ISSN 1028-8546

Volume XXVI Number 3
Section: En October, 2020

Azerbaijan Journal of Physics

Fizika

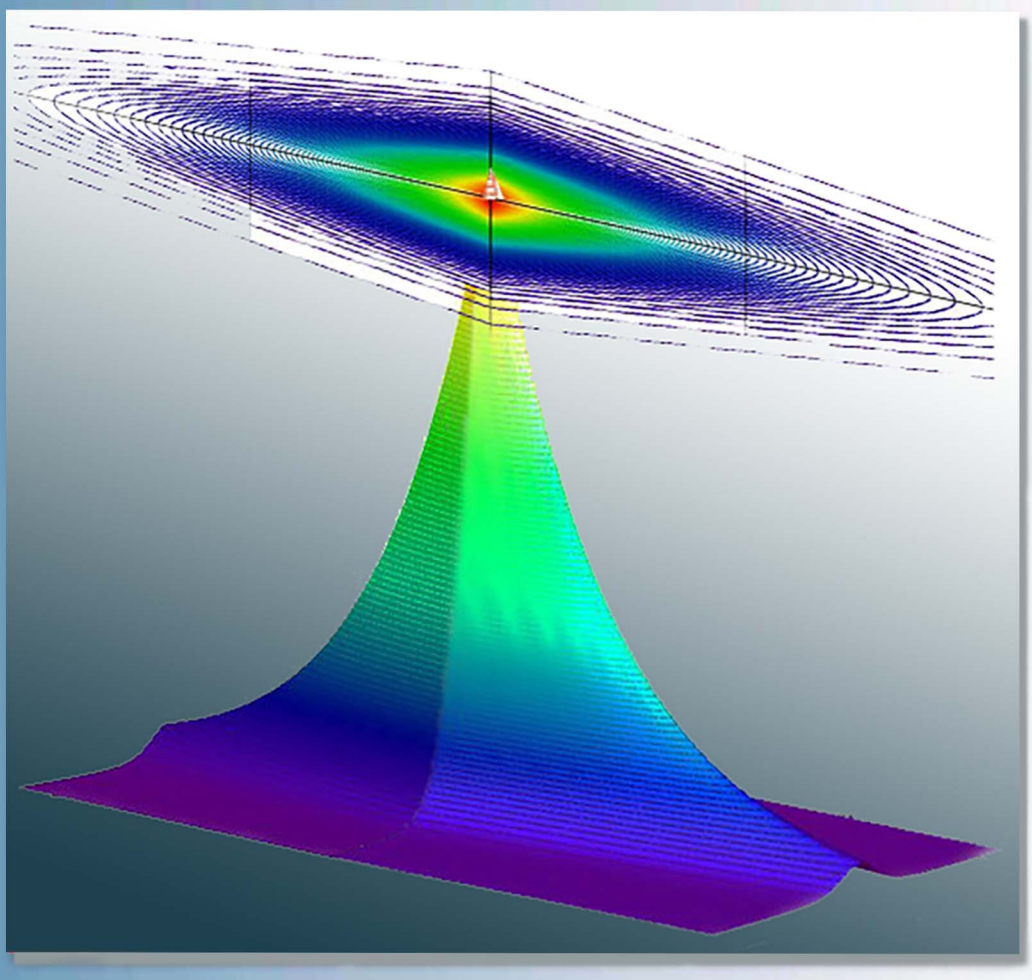

www.physics.gov.az
jophphysics.wixsite.com/ajpphysics

Institute of Physics
Azerbaijan National Academy of Sciences
Department of Physical, Mathematical and Technical Sciences

Published from 1995
Ministry of Press and Information
of Azerbaijan Republic,
Registration number 514, 20.02.1995

ISSN 1028-8546
vol. XXVI, Number 03, 2020
Series: En

Azerbaijan Journal of Physics

FIZIKA

Institute of Physics
Azerbaijan National Academy of Sciences
Department of Physical, Mathematical and Technical Sciences

PUBLISHING OFFICE

131, H. Javid ave., AZ-1143, Baku
ANAS, Institute of Physics

Tel.: (99412) 539-51-63, 539-32-23
Fax: (99412) 537-22-92
E-mail: jophphysics@gmail.com
Internet: www.physics.gov.az
https://jophphysics.wixsite.com/ajpphysics

Published at "**Omeqa-5**"
41, Aga Nematulla str., Baku

Sent for printing on: __.__. 202_
Printing approved on: __.__. 202_
Physical binding:_____
Number of copies:_____200
Order:_____

It is authorized for printing:

INFLUENCE OF SINGLE-WALLED CARBON NANOTUBES ON DIELECTRIC RELAXATION AND ELECTRIC CONDUCTIVITY OF SMECTIC A LIQUID CRYSTAL WITH POSITIVE DIELECTRIC ANISOTROPY

T.D. IBRAGIMOV, A.R. IMAMALIYEV, G.F. GANIZADE
Institute of Physics of Azerbaijan National Academy of Sciences,
H.Javid av.13I, Baku, AZ1143, Azerbaijan
E-mail : tdibragimov @mail.ru

The effect of single-walled carbon nanotubes (SWCNTs) on the dielectric and conductivity properties of smectic A liquid crystal 4- nitrophenyl -4'- decyloxybenzoic acid has been studied. It was shown that the additive of SWCNTs with concentration of 0.5% leads to a decrease in the order parameter of 5CB. In this case, the clearing point is raised, the longitudinal component of the dielectric permittivity decreases while the transverse component increases. The incipient percolation effect promotes to the dominance of hopping electron conductivity over ionic conductivity, leading to an increase in specific conductance.

Keywords: smectic A liquid crystal; single-walled carbon nanotubes, dielectric permittivity; electric conductivity
PACS: 64.70.mj; 64.70.pv; 77.84.Nh; 82.70.Dd.

1. INTRODUCTION

In recent years, an alternative direction in the chemistry and physics of liquid crystals (LC) has been the creation of hybrid liquid crystal systems in which liquid crystal mixes or comes into contact with some other structure without chemical interaction. In particular, all modern displays are based on hybrid liquid crystal systems in which field effects in liquid crystals are combined with the properties of thin-film structure. An example of a hybrid liquid crystal system is also a polymer dispersed by liquid crystal.

Single-walled carbon nanotubes (SWCNTs) are rod-shaped and have a diameter comparable to cross-section of elongated LC molecules. In addition, there is strong interaction of nanotubes with LC molecules, as a result of which they are aligned along the preferred direction (director) of LC molecules [1]. In that respect, liquid crystal with such nanoparticles can significantly change its physical properties. A very minute concentration of carbon nanotubes in liquid crystals can have an impact on their electrical and optical properties. Liquid crystals provide a distinctive medium for controlling the alignment of carbon whereas carbon nanotubes are important for the enhancement and fine-tuning of liquid crystalline properties [2].

One of the major applications of LCs is displays. Their operation is based on electro-optical effects in LCs, with which their dielectric and conductive properties are closely coupled. A set of works has been devoted to the study of the dielectric and electro-optic properties of LC doped with single-walled carbon nanotubes. It was shown in [3-4] that the inclusion of tiny amount (0.01-0.02 wt. %) of SWCNTs in the nematic matrix with positive dielectric anizotropy increases the nematic-isotropic transition temperature and dielectric anisotropy while threshold voltage decreases. Moreover, the composites filled in the cells have been probed under applied bias electric field and it enhanced the nematic ordering of the liquid crystal molecules in the composites which results overall improvement of their dielectric and electro-optic parameters [4]. A significant enhancement in the dielectric anisotropy and conductivity of SWCNTs doped p-ethoxybenzylidene p-butylaniline nematic LC at concentration of 0.01 and 0.02 wt.% was observed in work [5]. Influence of SWCNTs on the re-entrant phenomenon in LCs has been studied in [6]. Here a small concentration (0.5 wt.%) of SWCNTs doped to a nematic material not only induces the layered smectic A mesophase but also leads to the nematic-smectic-nematic re-entrant sequence. The presence of SWCNTs changes the physical properties like splay elastic constant, rotational viscosity and electrical conductivity. SWCNTs were dispersed in nematic liquid crystal 4-pentyl-4′-cyanobiphenyl at the concentration of 0.02 and 0.05 wt% in work [7, 8]. Differential scanning calorimetry and temperature-dependent dielectric studies suggest decrease in clearing temperature of the composite materials as compared to the pure material. Ionic conductivity increases by two orders of magnitude due to the dispersion of such a low concentration (0.05 wt%) of SWCNTs. Dielectric studies also show that the presence of the SWCNTs decreases the effective longitudinal as well as transverse components of the dielectric permittivity. Presence of SWCNTs increases the relaxation frequency corresponding to flip-flop motion of molecules around their short axes.

The aim of this work is to study the effect of SWCNTs at concentration corresponding to percolation phenomenon on the dielectric and conductivity properties of smectic A liquid crystal 4-nitrophenyl -4'- decyloxybenzoic acid .

2. MATERIALS AND METHODS

We used smectic A liquid crystal 4- nitrophenyl -4'- decyloxybenzoic acid as a matrix. A dielectric anisotropy of this LC is positive. The temperature range of smectic phase is located between 55°C and 77°C.

131, H.Javid ave, AZ-1143, Baku
ANAS, Institute of Physics
E-mail: jophphysics@gmail.com

The single-walled carbon nanotubes (US, Research Nanomaterials, In.) were added into the liquid crystal with concentration of 0.5 wt. %. Then obtained mixture was shaken in a vortex mixer for 1 hour at temperature 50°C, followed by sonication with dispergator Ultrasonic Cleaner NATO CD-4800 (China) for 4 hours.

The cell had a sandwich structure and consisted of two plane-parallel glass plates whose inner surfaces were coated with thin transparent and conductive indium-tin-oxide (ITO) layer. Planar orientation of molecules was attained by coating the inner substrate surfaces with rubbed polyimide layers. For obtaining of homeotropic orientation of LC molecules, we used the surfactant (polysiloxane). The cell thickness was fixed with calibrated 20 μm polymer spacers for measurements. Both the colloid and the pure LC were injected into the empty cell by capillary action at the isotropic state. To increase the dispersion, the cells with the colloid were placed at electric field of 40 V to achieve turbulence and were kept for 2 days. In this case, no aggregation of particles was observed. The stuffed cell was kept in the special heater with temperature regulator GL-100 (China). The copper-constantan thermocouple was used for temperature control. An accuracy of temperature determination was 0.1°C.

Temperature of the smectic-isotropic transition was defined under the Carl Zeiss polarization microscope (model 720, Germany).

Dielectric and conductivity measurements were carried out by the Precision LCR Meter 1920 (IET Labs. Inc., USA) over the frequency range of 20 Hz – 1 MHz and at temperatures between 23°C – 43°C. In such a case, applied voltage was 0.5 V for both LC molecular orientations.

3. RESULTS AND DISCUSSION

Observations under the polarizing microscope showed that the clearing point decreases from 76.8°C to 75.1°C at the additive of single-walled carbon nanotubes into the liquid crystal. This is an indirect fact of a decrease in the order parameter of the liquid crystal.

The frequency dependences of the real and imaginary parts of the dielectric permittivity of both the pure LC and the corresponding colloid at the homeotropic configuration and temperature of 58°C are shown in Fig. 1.

As can be seen, the value of ε' for the colloid is less than for the pure liquid crystal at all frequencies. These values change slightly up to 10^5 Hz then they decrease sharply. The value of ε' is 17.71 for the pure LC at the frequency of 2 kHz while it corresponds to 15.92 for the colloid. Starting from 9 kHz, the value of the dielectric permittivity of the colloid slightly increases and is 16.45 at 15 kHz. The presence of SWCNTs increases the value of ε " to 30 kHz, then it is lower down to 1 MHz. In this case, the maximum of dielectric absorption is shifted to the high frequency region from 400 kHz to 600 kHz.

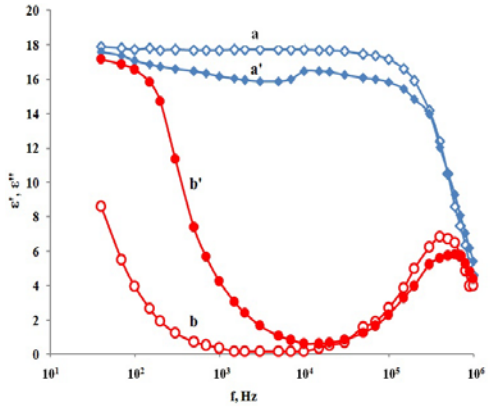

Fig. 1. Frequency dependences of the real ε ' and imaginary ε' 'components of the dielectric permittivity at the homeotropic configuration (temperature 58˚C): (a) ε' of the pure LC, (a') ε' of the colloid, (b) ε " of the pure LC, (b') ε" of the colloid.

It is known that the relaxation time of LC molecules, which is characterized by the flip-flop motion of molecules from one direction to the opposite direction, is determined as follows:

$$\tau = \frac{1}{2\pi f}, \qquad (1)$$

where f is the frequency of the applied electric field. The addition of nanotubes reduces the relaxation time from $4.0 \cdot 10^{-7}$ s to $2.7 \cdot 10^{-7}$ s at 58°C. Obviously, this is due to a decrease in the connection between the LC molecules.

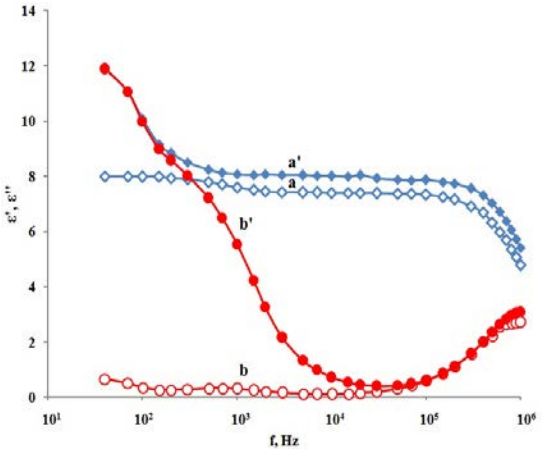

Fig. 2. Frequency dependences of the real ε' and imaginary ε" components of the dielectric permittivity in the planar configuration (temperature 58˚C): (a) ε' of the pure LC, (a ') ε' of the colloid, (b) ε " of the pure LC, (b ') ε" of the colloid.

The frequency dependences of the real and imaginary components of the dielectric permittivity of the pure LC and the colloid at planar configuration and temperature of 58°C are shown in Fig. 2. As can be seen, the value of ε' for the colloid is greater than for the pure LC at all frequencies. The real part of the dielectric permittivity remains almost unchanged for the colloid and the pure LC at medium frequencies. In this case, its value is 7.45 for pure LC while it

corresponds to 8.06 for the colloid at 2 kHz. The value of ε' decreases sharply after 10^5 Hz.

It should be noted that the dielectric anisotropy of the pure LC is 10.26 at medium frequencies while this value is 7.86 for the colloid. In other words, the addition of SWCNTs decreases the dielectric anisotropy.

We will analyze the experimental facts using the Mayer-Meier theory for nematic liquid crystals, which, in a rough approximation, can be used for smectic liquid crystals. According to this theory, expressions for both components of the permittivity are determined as follows [9]:

$$\varepsilon'_{II} = 1 + \frac{NHF}{\varepsilon_0}\left\{\gamma_{av} + \frac{2}{3}S\Delta\gamma + F\frac{p_e^{\,2}}{3k_BT}\left[1 - \frac{1}{2}\left(1 - 3\cos^2\beta\right)S\right]\right\} \quad (2)$$

$$\varepsilon'_{\perp} = 1 + \frac{NHF}{\varepsilon_0}\left\{\gamma_{av} - \frac{1}{3}S\Delta\gamma + F\frac{p_e^{\,2}}{3k_BT}\left[1 + \left(1 - 3\cos^2\beta\right)S\right]\right\} \quad (3)$$

From where we get:

$$\Delta\varepsilon' = \frac{NHF}{\varepsilon_0}\left[\Delta\gamma - F\frac{p_e^{\,2}}{2k_BT}\left(1 - 3\cos^2\beta\right)\right]S \quad (4)$$

where F is reaction field factor, H is the cavity form factor, $\gamma_{av} = (\gamma_{II} + 2\gamma_{\perp})/3$ is the average value of polarizability of LC molecules, $\Delta\gamma = \gamma_{II} - \gamma_{\perp}$ is the anisotropy of polarizability, N is the number of LC molecules per unit volume, S is the order parameter, β is the angle between the point molecular dipole p_e and the axis of maximum molecular polarizability, ε_0 is dielectric permittivity of vacuum, k_B is Boltzmann constant, T is Kelvin temperature.

Since the concentration of the colloid is very small, the number of embedded particles per unit volume is also small. That is, the number of LC molecules per unit volume N decreases insignificantly. This liquid crystal has a positive dielectric anisotropy. Hence, its dipole moment is directed along the long axis of the molecule as well as the direction of maximal polarizability. Therefore, the angle β = 0 and cos β = 1. In this case, the Maier-Meier expressions are converted to the form:

$$\varepsilon'_{II} = 1 + \frac{NHF}{\varepsilon_0}\left\{\gamma_{av} + \frac{2}{3}S\Delta\gamma + F\frac{p_e^{\,2}}{3k_BT}\left[1 + S\right]\right\} \quad (5)$$

$$\varepsilon'_{\perp} = 1 + \frac{NHF}{\varepsilon_0}\left\{\gamma_{av} - \frac{1}{3}S\Delta\gamma - F\frac{p_e^{\,2}}{3k_BT}\left[2S - 1\right]\right\} \quad (6)$$

Using (5-6) may be obtaned:

$$\Delta\varepsilon' = \frac{NHF}{\varepsilon_0}\left[\Delta\gamma + F\frac{p_e^{\,2}}{k_BT}\right]S \quad (7)$$

Let us denote by $\Delta S = S - S_0$, where S is the order parameter of the liquid crystal doped with nanotubes, S_0 is the order parameter of the pure LC; $\Delta\varepsilon'_{II}$ is the difference between the longitudinal component of the real part of the dielectric permittivity after doping and before doping of the liquid crystal; $\Delta\varepsilon'_{\perp}$ is the difference between the transverse component of the real part of the dielectric permittivity after and before doping of the liquid crystal; $\Delta(\Delta\varepsilon')$ is the difference between the dielectric anisotropy after and before doping the liquid crystal. Then you can write:

$$\Delta\varepsilon'_{II} = \frac{NHF}{3\varepsilon_0}\left[2\Delta\gamma + \frac{p_e^{\,2}}{k_BT}\right]\Delta S \quad (8)$$

$$\Delta\varepsilon'_{\perp} = -\frac{NHF}{3\varepsilon_0}\left[\Delta\gamma + F\frac{2p_e^{\,2}}{k_BT}\right]\Delta S \quad (9)$$

Their difference gives the change in dielectric anisotropy:

$$\Delta(\Delta\varepsilon') = \frac{NHF}{\varepsilon_0}\frac{p_e^{\,2}}{k_BT}\Delta S \quad (10)$$

It is obvious that the expressions in parentheses of relations (8) and (9) have positive values. The experiment shows a decrease in the longitudinal component of the dielectric permittivity ($\Delta\varepsilon'_{II} < 0$) and, accordingly, the condition $\Delta S < 0$ must be satisfied, that is, the order parameter decreases with the additive of nanotubes. The experiment also shows an increase in the transverse component of the permittivity with the addition of nanotubes, that is, $\Delta\varepsilon'_{\perp} > 0$.Therefore, the condition $\Delta S < 0$ is satisfied, indicating on decrease in the order parameter. Similarly, a decrease in the dielectric anisotropy also indicates a decrease in the order parameter of the colloid relative to the corresponding parameter of the pure liquid crystal. The decrease in the order parameter can be explained by the fact that an appreciable part of the nanotubes are localized in the

gap between the layers of the smectic liquid crystal, since their diameter is about 1 nm while the width of the gap is 2 nm. In this case, the ordering of LC molecules in the layers is disrupted, leading to a decrease in the order parameter and the clearing temperature.

The frequency dependences of the specific conductance of the pure LC and the colloid are shown in Fig. 3. As can be seen from this figure, the longitudinal component of the conductivity of the pure LC is greater than the transverse component. Obviously, this is due to the easier movement of ions along the director of the liquid crystal. Another thing is in the colloid, in which the percalation effect occurs. In the case, the predominance of the hopping electronic conductivity over the ionic one. Electrons move along the long axis of the nanotubes. This has the strong effect on the change in conductivity when nanotubes are embedded in the liquid crystal. The transverse component of the conductivity increases much more strongly than the longitudinal component. In particular, the longitudinal component of the conductivity of the pure liquid crystal increases from $1.82 \cdot 10^{-8}$ S/m to $2.44 \cdot 10^{-7}$ S/m at 40 Hz and from $2.28 \cdot 10^{-8}$ S/m to $2.40 \cdot 10^{-7}$ S/m at 2 kHz. With further increase in frequency, the specific conductance rises sharply and after the frequency of 15 kHz they equalize and reach the value of $4.19 \cdot 10^{-4}$ S/m at 1 MHz. The transverse component of the specific conductance of the pure LC upon the inclussion of nanotubes increases from $1.45 \cdot 10^{-9}$ S/m to $3.80 \cdot 10^{-7}$ S/m at 40 Hz and from $1.69 \cdot 10^{-8}$ S/m to $4.20 \cdot 10^{-7}$ S/m at 2 kHz. Then the specific conductance rises sharply, they equalize after 50 kHz and reach the value of $2.08 \cdot 10^{-4}$ S/m at 1 MHz. Note that additional electrons arising due to the percalation effect are delayed at high frequencies. For this reason, the specific conductance of the colloid has the same value as that of pure LC.

It is obvious that the change in conductivity correlates with a change in the imaginary part of the dielectric permittivity and the frequency. Therefore, the conductivity increases with an increase in these parameters. Due to the difference in the frequency ranges of the dispersion ε'_{II} и $\varepsilon'_{\perp}$, the maxima ε''_{II} and $\varepsilon''_{\perp}$, are observed at different frequencies and, accordingly, σ_{II} and $\sigma_{\perp}$ begin to increase at the same frequencies. The additive of nanotubes shifts the dispersion of the dielectric permittivity to the high-frequency region. In this case, the same shift occurs with the dispersion of the conductivity.

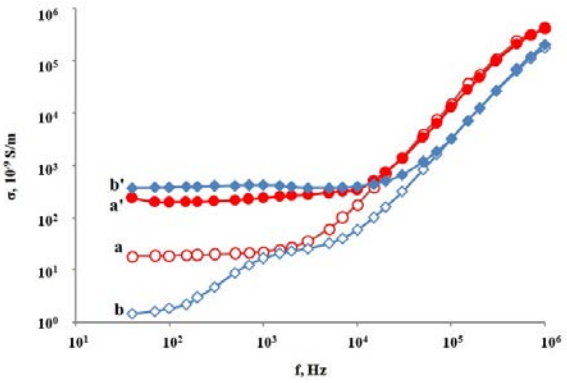

Fig. 3. Frequency dependence of the components of spesific conductance at 58°C: (a) σ_{II} of the pure LC, (a') σ_{II} of thr colloid, (b) $\sigma_{\perp}$ of the pure LC, (b') $\sigma_{\perp}$ of the colloid.

Ohmic conductivity in alternating current can be represented as:

$$\sigma = 2\pi f \varepsilon_0 \varepsilon'' \qquad (11)$$

4. CONCLUSSİON

It is shown that the additiive of single-walled carbon nanotubes into the smectic A liquid crystal with the concentration of 0.5 wt. % leads to a decrease in the order parameter and clearing temperature, which is connected with the inclussion of a part of the nanotubes into the gap between the layers. Due to the percalation effect, the electron hopping conductivity dominates over the ionic one, which leads to an increase in the specific conductance.

[1] *N.R. Jber, A.A. Rashad, M. S Shihab*. J. of Molecular Structure, 2013. 1043, 28–36.
[2] *S.P. Yadav, S. Singh*. Progress in Materials Science, 2016. 80, 38-76.
[3] *D. Singh, U.B. Singh, M.B. Pandey, R. Dabrowski, R. Dhar*. Optical Materials, 2018. 84, 16-21.
[4] *D. Singh, U.B. Singh, M.B. Pandey, R. Dhar*. Liquid Crystals, 2019. 46 (9), 1389-1395.
[5] *T. Vimal, S. Pandey, S.K. Gupta, D.P. Singh, R. Manohar*. 2015. Journal of Molecular Liquids, 204, 21-26.
[6] *G.V. Varshini, D.S. Rao, P.K. Mukherjee, S.K. Prasad*. J.Phys. 2018. Chem. B, 122 (47), 10774-10781.
[7] *R. Verma, M. Mishra, R. Dhar, R. Dabrowski*. Liquid Crystals, 2016. 44 (3), 544-556.
[8] *R. Verma, M. Mishra, R. Dharb, R. Dabrowskis*. Journal of Molecular Liquids, 2016. 221, 190-196.
[9] *L. Blinov*. Structure and Properties of Liquid Crystal, 2011. Springer: New York.

Received: 19.10.2020

THE EXCITATION OF UNSTABLE WAVES OF THERMOELECTROMAGNETIC CHARACTER IN CONDUCTIVE MEDIUMS OF ELECTRONIC TYPE OF CHARGE CARRIER

E.R. HASANOV, Sh.G. KHALILOVA, E.O. MANSUROVA, G.M. MAMMADOVA
Institute of Physics of ANAS, H. Javid ave., 131, Baku, Azerbaijan
E_mail: shahlaganbarova@gmail.com

From theoretic analysis of excited waves in the medium with one type of charge carrier it is obtained, that thermoelectromagnetic wave is the growing wave and medium becomes the energy radiation source. The frequency and increment of excited waves are expressed in terms of frequencies of electromagnetic and thermomagnetic waves.

Keywords: growing frequency, frequency, energy source, charge carriers, electric conduction tensor.
PACS: 72.70.m, 72.70.+m, 73.40.Gk, 73.40.Jn, 73.40.Mr, 73.43.Jn.

INTRODUCTION

The excitation of thermomagnetic waves in isotropic plasma is the theoretically analyzed in work [1]. In this work it is shown that thermomagnetic wave with frequency dependent on constant temperature gradient ($\nabla T = const$) appears at hydrodynamic motions of charge carriers in plasma without external magnetic field. Later, in works [2 – 3] confirmed that excited thermomagnetic wave in solid substance does not interact with sound waves (i.e. lattice small oscillations). Some excitation conditions of thermomagnetic waves in semiconductors investigated in work [4]. In this work, it is shown that the presence of recombination's and generations in semiconductors significantly changes the excitation conditions of thermomagnetic waves in impurity semiconductors with two types of charge carriers. However, some excitation conditions of thermomagnetic waves in anisotropic conductive mediums investigated in work [5]. The expressions for electric conduction tensor dependent on thermomagnetic wave frequency obtained in this work. In this theoretical work, we will investigate some excitation conditions of thermomagnetic waves in conductive medium of electron type of charge carriers. The term "thermomagnetic wave" is firstly introduced.

THE MAIN TASK EQUATIONS

At the presence of temperature gradient, $\nabla T = const$ the concentration gradient ∇n of charge carriers appears and their hydrodynamic motion with $v(\vec{r},t)$ velocity takes place. The variable magnetic field H' in medium appears under influence of external electric field. As a result, the current density in medium has the form:

$$j' = \sigma\vec{E}^* + \sigma'\left[\vec{E}^*\vec{H}^*\right] - \alpha\vec{\nabla}T - \alpha'\left[\vec{\nabla}TH'\right] \qquad (1)$$

Here E^* is electric field in the medium.

$$\vec{E}* = \vec{E} + \frac{\left[\vec{\upsilon}^* H'\right]}{c} + \frac{T}{e}\frac{\vec{\nabla}n}{n}; e > 0 \qquad (2)$$

E is external electric field, $\frac{\left[\vec{\upsilon}^* H'\right]}{c}$ is electric field appearing at hydrodynamic motions of charge carriers, $\frac{T}{e}\frac{\vec{\nabla}n}{n}$ is electric field appearing at the presence of charge carrier concentration. The diffusion members, which at $T << eE_0 l$ (l is mean free path of charge carriers) are less than σE are not considered in expressions (1-2). From (1-2) we obtain the total electric field in the medium with the help of Maxwell equation $rot\vec{H} = \frac{4\pi}{c}\vec{j}$ by following way. Substituting (2) in (1), we obtain the equation for electric field of following form:

$$\vec{X} = \vec{A} + \left[\vec{B},\vec{X}\right] \qquad (3)$$

From (3) we easily obtain:

$$\vec{X} = \vec{A} + \left[\vec{B}\vec{A}\right] + (\vec{A}\vec{B})\vec{B} \qquad (4)$$

or

$$\vec{E} = -\frac{\left[\vec{v}\vec{H}'\right]}{c} - \Lambda'\left[\nabla\vec{T}\vec{H}'\right] + \frac{c}{4\pi\sigma}rot\vec{H} - \frac{c\sigma'}{4\pi\sigma^2}\left[rot\vec{H}',\vec{H}'\right] + \frac{T}{e}\frac{\nabla\rho}{\rho} + \Lambda\nabla T \qquad (5)$$

Here $\Lambda = \frac{\alpha}{\sigma}$, $\Lambda' = \frac{\alpha'\sigma - \alpha\sigma'}{\sigma}$, σ is electric conduction, Λ is differential thermal e.m.f., Λ' is Nernst-Ettingshausen effect coefficient. In anisotropic conductive mediums, the total electric field has the following form:

$$\vec{E} = \varsigma\vec{j} + \varsigma'\left[\vec{j}\vec{H}\right] + \varsigma''\left(\vec{j}\vec{H}\right)H + \Lambda\nabla T + \Lambda'\left[\nabla TH\right] + \Lambda''\left(\left[\nabla TH\right]\right)H \qquad (6)$$

131, H. Javid ave, AZ-1143, Baku
ANAS, Institute of Physics
E-mail: jophphysics@gmail.com

or

$$\vec{E} = \vec{E}_1 + \vec{E}_2 + \vec{E}_3 + \vec{E}_4 + \vec{E}_5 + \vec{E}_6 \qquad (7)$$

In (7) $\vec{E}_1$ is electric field towards current direction, $\vec{E}_2$ is electric field perpendicular to current direction, $\vec{E}_3$ is electric field directed towards $\vec{H}$, $\vec{E}_4$ is electric field directed towards ∇T, $\vec{E}_5$ is electric field perpendicular to ∇T and $\vec{H}'$, $\vec{E}_6$ is electric field directed towards ∇T and $\vec{H}'$.

In anisotropic mediums, expression (6) has the form:

$$E_i = \varsigma_{im} j'_m + \varsigma'_{im}\left[jH\right]_m + \varsigma''_{im}\left[jH\right]H_m + \Lambda_{im}\nabla_m T + \Lambda'_{im}\left[\nabla TH\right]_m + \Lambda''_{im}\left[\nabla TH\right]H_m \qquad (8)$$

We consider the excitation of thermoelectromagnetic waves in anisotropic mediums without external magnetic field (i.e. $H_0 = 0$) and that is why the main equations of our task with taking under consideration the displacement current, have the following form:

$$\begin{aligned} E'_i &= \varsigma_{im} j'_m + \Lambda'_{im}\left[\nabla TH'\right]_m \\ rot\vec{H}' &= \frac{4\pi}{c}\vec{j}' + \frac{1}{c}\frac{\partial \vec{E}'}{\partial t} \\ rot\vec{E}' &= -\frac{1}{c}\frac{\partial \vec{H}'}{\partial t} \end{aligned} \qquad (9)$$

Suppose that all variable values in (9) change by fluctuation way (i.e. $E' << E_0, \vec{j}' << \vec{j}_0$) and have the character of monochromatic waves.

$$(E', H') \sim e^{i(\vec{k}\vec{r} - wt)} \qquad (10)$$

k is wave vector, w is oscillation frequency. Thus, we easily obtain from (9):

$$\begin{aligned} E'_i &= \varsigma_{im} j'_m + \Lambda'_{im}\left[\nabla TH\right]_m \\ j'_m &= \frac{ic^2}{4\pi w}\left[\vec{k}\left[\vec{k}\vec{E}'\right]\right]_m + \frac{iw}{4\pi}E'_m \end{aligned} \qquad (11)$$

THEORETICAL CALCULATIONS

For obtaining of dispersion equation from (11), we chose the following coordination system:

$$\begin{aligned} k_1 \neq 0, k_2 = 0, k_3 = 0 \\ \nabla_1 T \neq 0, \nabla_2 T \neq 0, \nabla_3 T = 0 \end{aligned} \qquad (12)$$

Taking under consideration (12) and (11) we easily obtain:

$$E'_i\left[\frac{ic^2}{4\pi w}\varsigma_{ie}k_e k_m + i\frac{w^2 - c^2k^2}{4\pi w}\varsigma_{im} + \frac{c\Lambda'_{ie}}{w}k_e\nabla_m T - \frac{c\Lambda'_{im}}{w}\vec{k}\vec{\nabla}T\right] = \delta_{im}E_{im} \qquad (13)$$

Substituting

$$E'_m = \delta_{im}E'_i \qquad (14)$$

We obtain from (13):

$$\left(\psi_{im} - \delta_{im}\right)E'_i = 0 \qquad (15)$$

where $\delta_{im} = 1$ at $i = m$, $\delta_{im} = 0$ at $i \neq m$.

Determinant from (15) should be equal to zero, i.e.

$$\left|\psi_{im} - \delta_{im}\right| = 0 \qquad (16)$$

From (16) we obtain:

$$\left(\psi_{11}-1\right)\left(\psi_{22}-1\right)\left(\psi_{33}-1\right) + \psi_{12}\psi_{31}\psi_{23} + \psi_{21}\psi_{32}\psi_{13} - \psi_{31}\psi_{13}\left(\psi_{22}-1\right) - \psi_{32}\psi_{23}\left(\psi_{11}-1\right) - \psi_{21}\psi_{12}\left(\psi_{33}-1\right) = 0 \qquad (17)$$

Here

$$\psi_{11} = \frac{iw}{4\pi}\varsigma_{11}, \psi_{12} = i\frac{w^2 - c^2k^2}{4\pi w}\varsigma_{12} + \frac{w_{11} - w_{12}}{w}, \psi_{13} = i\frac{w^2 - c^2k^2}{4\pi w}\varsigma_{13} - \frac{w_{13}}{w}$$

$$\psi_{21} = \frac{iw}{4\pi}\varsigma_{21}, \psi_{22} = i\frac{w^2 - c^2k^2}{4\pi w}\varsigma_{22} + \frac{w_{21} - w_{22}}{w}, \psi_{23} = i\frac{w^2 - c^2k^2}{4\pi w}\varsigma_{23} + \frac{w_{23}}{w}$$

$$\psi_{31} = \frac{iw}{4\pi}\varsigma_{31}, \psi_{32} = i\frac{w^2 - c^2k^2}{4\pi w}\varsigma_{32} + \frac{w_{31} - w_{32}}{w}, \psi_{33} = i\frac{w^2 - c^2k^2}{4\pi w}\varsigma_{33-}\frac{w_{33}}{w}$$

$$w_{11} = ck\Lambda'_{11}\nabla_1 T, w_{12} = ck\Lambda'_{12}\nabla_2 T, w_{13} = ck\Lambda'_{13}\nabla_1 T$$

$$w_{21} = ck\Lambda'_{21}\nabla_2 T, w_{22} = ck\Lambda'_{22}\nabla_1 T, w_{23} = ck\Lambda'_{23}\nabla_1 T$$

$$w_{31} = ck\Lambda'_{31}\nabla_1 T, w_{32} = ck\Lambda'_{32}\nabla_1 T, w_{33} = ck\Lambda'_{33}\nabla_1 T$$

The solution of dispersion equation (17) is impossible because of its high degree and that's why we use the numerical value of ψ_{ik} tensor which depends on medium properties:

$$1)\ \psi_{11}=\psi_{21}=\psi_{31},\ 2)\ \psi_{12}=\psi_{22}=\psi_{32},$$
$$3)\ \psi_{13}=\psi_{23}=\psi_{33} \quad (18)$$

Taking under consideration (18) in (17) we easily obtain:

$$\psi_{11}+\psi_{22}+\psi_{33}-1=0 \quad (19)$$

Substituting tensor values in (19) we obtain:

$$\omega^2+i\frac{4\pi}{\varsigma}\omega-c^2k^2(1-\frac{\varsigma_{11}}{\varsigma})+4\pi i\frac{w_{21}-w_{33}-w_{22}}{\varsigma}=0 \quad (20)$$

where ω is thermoelectromagnetic wave frequency. From (20) it is seen that if $w_{21}=w_{33}+w_{22}$ then the excited wave has the pure electromagnetic character. Thermoelectromagnetic wave excites under $w_{21}>w_{33}+w_{22}$ conditions or $w_{21}<w_{33}+w_{22}$ conditions.

Under conditions, $w_{21}>w_{33}+w_{22}$ we obtain from (20):

$$\omega_1=-ick+(ckw_{21})^{1/2}+i(ckw_{21})^{1/2}$$
$$\omega_2=-ick-(ckw_{21})^{1/2}-i(ckw_{21})^{1/2} \quad (21)$$

From (21) it is seen that wave with ω_2 frequency is damping one. The wave with ω_1 frequency can grow at:

$$w_{21}>ck \text{ ; i.e. at } \Lambda'_{21}\nabla_2 T>1 \quad (22)$$

Under conditions $w_{21}<w_{33}+w_{22}$ at $(\Lambda'_{22}+\Lambda'_{33})\nabla_1 T>1$ thermoelectromagnetic wave with frequency $\omega_0=\left[ck\left(w_{22}+w_{33}\right)\right]^{1/2}$ and increment $\gamma=\left[ck\left(w_{22}+w_{33}\right)\right]^{1/2}-ck$ is growing one. Under conditions frequency $w_{21}>w_{33}+w_{22}$ and increment of thermoelectromagnetic wave are: $\omega_0=\left(ckw_{21}\right)^{1/2}$, $\gamma=\left(ckw_{21}\right)^{1/2}-ck$. Thus, excited thermoelectromagnetic wave under the considered conditions always has frequency, which is bigger than increment.

DISCUSSION OF OBTAINED RESULTS

The thermoelectromagnetic waves in different directions respective of the electric field direction excite in anisotropic mediums with one type of charge carriers. The frequencies of these waves are different ones in dependence on electric conduction values. The conditions of wave growth of these waves are clear and correspond to experiment. The different thermoelectromagnetic waves with different frequencies are excited. These frequencies depend on temperature gradient values. The increment of growth of these waves is less than their frequency. This theory constructed without external magnetic field. Probably, at the presence of external magnetic field the appearance conditions of these waves essentially change. The frequency numerical values of these waves are approximately by order 10^{10} -10^{11} Hz. In this frequency interval, the phenomena take place with high frequency and can serve as energy sources.

[1] *L.E. Gurevich.* Thermomagnetic waves and excitation of the magnetic field in nonequlibrium plasmas JETP, 44, 548-555, 1963.

[2] *L.E. Gurevich, B.L. Helmont.* Hydrothermomagnetic waves in a weakly homogeneous plasma. JETP, 884-900, 1964.

[3] *E.R. Hasanov, Sh. G. Khalilova, Z.A. Tagiyeva, V.M. Hajiyeva, S.S. Ahadova.* Exciation of termomagnetic and recombination waves in impurity with two types of current carriers. 16th International Conference on "Technical and Physical Problems of Elektrical Engineering" 12-13 October 2020 Istanbul, Rumeli University, 1-6.

[4] *E.R. Hasanov, Sh.G. Khalilova, E.O. Mansurova, N.M. Tabatabaei.* Inretnatonal journal "Technical and Physical Problems of Engineering" V 12, № 1, 49-52, 2020.

[5] *E.R. Hasanov, Sh.G. Khalilova, A.I. Alekberov, A.B Maharramov, E.O. Mansurov.* Transactions of Azerbaijan National Academy of Sciences, Physics and Astronomy, № 2, 73-80, 2020.

Received: 13.10.2020

LOCAL SPIN-WAVE REGIONS IN A SUPERLATTICE CONSTRUCTED FERRO- AND ANTIFERROMAGNETIC SEMICONDUCTORS MATERIALS

V.A. TANRIVERDIYEV, V.S. TAGIYEV, G.G. KERIMOVA
Institute of Physics of the National Academy of Sciences of Azerbaijan, Baku AZ -1143, Baku, H. Javid ave.131, E-mail: vahid_tanriverdi @yahoo.com.

The s-d (or s-f) interaction model is used to study the local spin-wave excitations in a superlattice constructed by alternating layers of simple-cubic Heisenberg ferromagnetic and antiferromagnetic semiconductors materials. The spin-wave regions for local spin waves propagating in a general direction in the superlattice are derived by the Green function method. The results are i1lustrated numerically.

PACS: 75.70.Cn. 75.40.Gb
Keywords: spin wave, superlattice.

INTRODUCTION

Magnetic layered structures constructed by different materials have received increasing interest during the last decade. Studies on artificial magnetic superlattices, either experimental or theoretical have been a subject of growing interests, because these structures are realizable in laboratories, whose characteristics may be much different from those of its component materials [1-5]. The spin waves spectrum, which is the signature of the periodicity, has been intensively studied in multilayered magnetic materials. The materials with periodic magnetic structure can be refereed to as magnonic crystals. Many physical properties of layered magnetic systems may be explained by the spin wave energy gap [6,7].

There have been considerable theoretical studies of spin excitations in the long-wavelength limit and in the short-wavelength limit, where the exchange coupling is dominant [8-10]. Most of these studies have been devoted experimental research of the superlattice properties consisting of two different ferro- or antiferromagnetic materials. However, little attention been paid on theoretical study of superlattice constructed by different type magnetic materials. Spin-wave excitations of ferro- and antiferromagnetic superlattice were studied in Ref [11]. In this paper we will study spectrum of the local spin waves in the superlattice constructed by alternating layers of simple-cubic Heisenberg ferromagnetic and antiferromagnetic semiconductors materials using Green function technique.

MODEL AND FORMALISM

We consider a Heisenberg model for ferro-and antiferromagnetic semiconductors superlattice with a simple cubic lattice. A schematic diagram of the superlattice model in which the atomic layers of ferromagnetic semiconductors material alternate with atomic layers of antiferromagnetic semiconductors materials is illustrated in fig.1. Elementary unit cell of the superlattice consist of two layers, spins labeled with a and b belong antiferromagnetic semiconductors layer, spins c and d belong ferromagnetic semiconductors layer. Each atomic layers is assumed to be the [001] planes. Lattice constant of the superlattice in x-y plane is a.

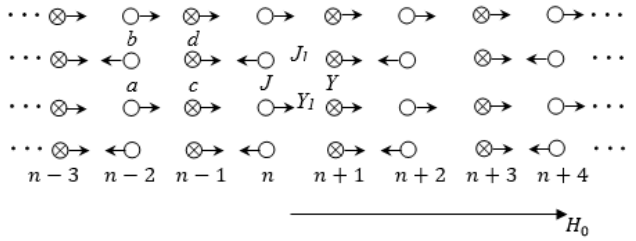

Fig.1. A superlattice model constructed by alternating layers of simple-cubic Heisenberg ferromagnetic and antiferromagnetic semiconductors materials. The lattice parameter a is assumed for both the materials.

Our total Hamiltonian H may be expressed as the sum of four terms:

$$H = H_{FM} + H_{FE} + H_{AFM} + H_{AFE}, \quad (1)$$

where H_{FM} is the Heisenberg Hamiltonian for the ferromagnetically ordered localized spins (of d or f type)

$$H_{FM} = -\frac{1}{2}\sum_{i,j} Y_{ij}\left(\vec{S}_i \vec{S}_j\right) - \sum_i g\mu_B\left(H_0 + H_{FM,i}^{(A)}\right)S_i^z \quad (2)$$

Hamiltonians H_{FE} and H_{AFE} representing an s-d (or s-f) ineraction for ferromagnetic and antiferromagnetic semiconductors materials, respectively

131, H.Javid ave, AZ-1143, Baku
ANAS, Institute of Physics
E-mail: jophphysics@gmail.com

$$H_{FE} = -\sum_i I_i \left(\vec{S}_i \vec{s}_i\right), \quad H_{AFE} = -\sum_i K_i \left(\vec{S}_i \vec{s}_i\right) \tag{3}$$

The term H_{AFM} in (1) describes antiferromagnetically ordered localized spins:

$$H_{AFM} = \sum_{i,j} J_{ij} \left(\vec{S}_i \vec{S}_j\right) - \sum_i g\mu_B\left(H_0 + {H_{AFM,i}}^{(A)}\right)S_{ia}^z - \sum_i g\mu_B\left(H_0 - {H_{AFM,i}}^{(A)}\right)S_{ib}^z \tag{4}$$

H_0 in (2) and (4) is the internal magnetic field, which is assumed to be paralle1 to the z axis and $H_{FM(AFM),i}^{(A)}$ anisotropy field with simple uniaxial anisotropy. $\vec{S}$ and $\vec{s}$ are localized and conduction electron spins operator, respectively. There are both ferro- and antiferromagnetically spin arrangements between spins of the two atomic layers at each interface as shown in fig.1. The exchange constant between constituents are Y_1 when ferromagnetically, and J_1 antiferromagnetically arrangements between spins of the two atomic layers at each interface. In order to obtain the solutions Green function equation, we define eight type Green functions in the random phase approximation:

$$G_{i,j}^{(a)}(\omega) = << S_{i,(a)}^+; S_{j,(a)}^- >>_\omega , \qquad G_{i,j}^{(b)}(\omega) = << S_{i,(b)}^+; S_{j,(a)}^- >>_\omega ,$$
$$G_{i,j}^{(c)}(\omega) = << S_{i,(c)}^+; S_{j,(a)}^- >>_\omega , \qquad G_{i,j}^{(d)}(\omega) = << S_{i,(d)}^+; S_{j,(a)}^- >>_\omega .$$
$$g_{i,j}^{(a)}(\omega) = << s_{i,(a)}^+; S_{j,(a)}^- >>_\omega , \qquad g_{i,j}^{(b)}(\omega) = << s_{i,(b)}^+; S_{j,(a)}^- >>_\omega ,$$
$$g_{i,j}^{(c)}(\omega) = << s_{i,(c)}^+; S_{j,(a)}^- >>_\omega , \qquad g_{i,j}^{(d)}(\omega) = << s_{i,(d)}^+; S_{j,(a)}^- >>_\omega .$$

Furthermore, to emphasize the layered structure we shall use the following two-dimensional. Fourier transformation [11,12]

$$G_{i,j}^{(\alpha)}(\omega) = \frac{1}{N}\sum_{k_{||}} G_{n,n'}^{(\alpha)}(\omega, k_{||})\, exp[\, ik_{||}(r_i - r_j)], \quad (\alpha = a, b, c, d), \tag{5}$$

where $k_{||}$ is two-dimensional wave vector parallel to the xy- plane , n and n' indices of the layers to which r_i and r_j belong , respectively. Employing the equation of motion for the Green functions [13,14] one obtains the following set of equations after Fourier transform (5)

$$\begin{cases} \lambda_a(\omega)G_{n,n'}^{(a)}(\omega,k_{||}) - \langle S_{\mathrm{n,a}}^z\rangle\left[J\gamma(k_{||})G_{n,n'}^{(b)}(\omega,k_{||}) - 0.5Y_1G_{n-1,n'}^{(c)}(\omega,k_{||}) - 0.5Y_1G_{n+1,n'}^{(c)}(\omega,k_{||})\right] = 2\langle S_{\mathrm{n,a}}^z\rangle\delta_{n,n'}, \\ \lambda_b(\omega)G_{n,n'}^{(b)}(\omega,k_{||}) - \langle S_{\mathrm{n,b}}^z\rangle\left[J\gamma(k_{||})G_{n,n'}^{(a)}(\omega,k_{||}) + J_1G_{n-1,n'}^{(d)}(\omega,k_{||}) + J_1G_{n+1,n'}^{(d)}(\omega,k_{||})\right] = 0, \\ \lambda_c(\omega)G_{n+1,n'}^{(c)}(\omega,k_{||}) + \langle S_{n+1,\mathrm{c}}^z\rangle\left[Y\gamma(k_{||})G_{n+1,n'}^{(d)}(\omega,k_{||}) + Y_1G_{n,n'}^{(a)}(\omega,k_{||}) + Y_1G_{n+2,n'}^{(a)}(\omega,k_{||})\right] = 2\langle S_{n+1,\mathrm{c}}^z\rangle\delta_{n+1,n'}, \\ \lambda_d(\omega)G_{n+1,n'}^{(d)}(\omega,k_{||}) + \langle S_{n+1,\mathrm{d}}^z\rangle\left[Y\gamma(k_{||})G_{n+1,n'}^{(c)}(\omega,k_{||}) - 2J_1G_{n,n'}^{(b)}(\omega,k_{||}) - 2J_1G_{n+2,n'}^{(b)}(\omega,k_{||})\right] = 0. \end{cases} \tag{6}$$

where $\lambda^a(\omega) = \omega - K\langle s^z\rangle - \frac{K^2\langle S_{AFM}^z\rangle\langle s^z\rangle}{\omega - g_e\mu_BH_0 - K\langle S_{AFM}^z\rangle} - g\mu H_{AFM}^{(A)} - 4J\langle S_{AFM}^z\rangle - Y_1\langle S_{FM}^z\rangle$,

$$\lambda^b(\omega) = \omega + K\langle s^z\rangle - \frac{K^2\langle S_{AFM}^z\rangle\langle s^z\rangle}{\omega - g_e\mu_BH_0 + K\langle S_{AFM}^z\rangle} + g\mu H_{AFM}^{(A)} + 4J\langle S_{AFM}^z\rangle + 2J_1\langle S_{FM}^z\rangle ,$$

$$\lambda^c(\omega) = \omega - I\langle s^z\rangle - \frac{I^2\langle S_{FM}^z\rangle\langle s^z\rangle}{\omega - g_e\mu_BH_0 - I\langle S_{FM}^z\rangle} - g\mu H_{FM}^{(A)} - 2Y\langle S_{FM}^z\rangle - Y_1\langle S_{AFM}^z\rangle ,$$

$$\lambda^d(\omega) = \omega - I\langle s^z\rangle - \frac{I^2\langle S_{FM}^z\rangle\langle s^z\rangle}{\omega - g_e\mu_BH_0 - I\langle S_{FM}^z\rangle} - g\mu H_{FM}^{(A)} - 2Y\langle S_{FM}^z\rangle - 2J_1\langle S_{AFM}^z\rangle ,$$

$$\gamma(k_{||}) = 2(\cos k_x a + \cos k_y a) ,$$

$\langle S_{FM}^z\rangle$ and $\langle S_{AFM}^z\rangle$ are average meaning of z-spins components in ferro - and antiferromagnetic sublattices, respectively.

The system is also periodic in the z direction, which lattice constant is d=2a. According to Bloch's theorem, we introduce the following plane waves [15, 16]:

$$G^{(\alpha)}_{n+2,n'}(\omega,k_{||}) = exp[ik_z d]\;\; G^{(\alpha)}_{n,n'}(\omega,k_{||})\;,$$

$$G^{(\alpha)}_{n-1,n'}(\omega,k_{||}) = exp[-ik_z d]\;\; G^{(\alpha)}_{n+1,n'}(\omega,k_{||}),\quad \alpha = a,b,c,d. \tag{7}$$

Using (7) the system of equations (6) may be written the following matrix form:

$$\begin{pmatrix} \lambda_a(\omega) & -J\langle S_{AFM}\rangle\gamma(k_{||}) & 0.5Y_1\langle S_{AFM}\rangle T^* & 0 \\ J\langle S_{AFM}\rangle\gamma(k_{||}) & \lambda_b(\omega) & 0 & J_1\langle S_{AFM}\rangle T^* \\ Y_1\langle S_{FM}\rangle T & 0 & \lambda_c(\omega) & Y\langle S_{FM}\rangle\gamma(k_{||}) \\ 0 & -2J_1\langle S_{AFM}\rangle T & Y\langle S_{FM}\rangle\gamma(k_{||}) & \lambda_d(\omega) \end{pmatrix} \cdot \begin{pmatrix} G^{(a)}_{n,n'}(\omega,k_{|\ |}) \\ G^{(b)}_{n,n'}(\omega,k_{|\ |}) \\ G^{(c)}_{n+1,n'}(\omega,k_{|\ |}) \\ G^{(d)}_{n+1,n'}(\omega,k_{|\ |}) \end{pmatrix} =$$

$$= \begin{pmatrix} 2\langle S^z_{\mathrm{AFM}}\rangle\delta_{n,n'} \\ 0 \\ 2\langle S^z_{\mathrm{FM}}\rangle\delta_{n+1,n'} \\ 0 \end{pmatrix} \tag{8}$$

where $T = 1 + exp(ik_z d)$ and T^* is the complex conjugate of T. The Green function are obtained by solving the equations (8). The poles of the Green functions occur at energies, which are the roots of the following local spin wave dispersion equation for the superlattice constructed ferro- and antiferromagnetic semiconductors materials:

$$\langle S_{AFM}\rangle^2\langle S_{FM}\rangle\big[JJ_1YY_1\gamma^2(k_{||})TT^*(\langle S_{AFM}\rangle + \langle S_{FM}\rangle) - J_1^2Y_1^2\langle S_{AFM}\rangle(TT^*)^2 -$$
$$J^2Y^2\langle S_{FM}\rangle\gamma^2(k_{||})\big] + \langle S_{AFM}\rangle\lambda_d(\omega)\big[J^2\langle S_{AFM}\rangle\gamma^2(k_{||})\lambda_c(\omega) - 0.5Y_1^2\langle S_{FM}\rangle TT^*\lambda_b(\omega)\big] +$$
$$\lambda_a(\omega)\big[2J_1^2\langle S_{AFM}\rangle^2TT^*\lambda_c(\omega) + \lambda_b(\omega)\big(\lambda_c(\omega)\lambda_d(\omega) - Y^2\langle S_{FM}\rangle^2\gamma^2(k_{||})\big)\big] = 0 \tag{9}$$

CONCLUSION

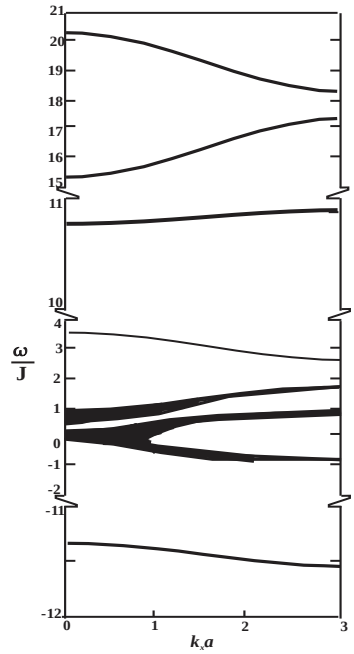

Fig. 2. The bulk spin–wave regions in the superlattice as a function of transverse components of wavevectors. The values of parameters are following: $J/Y = 0.5$, $J_1/Y = 0.5$, $Y_1/Y = 1.5$, $I/Y = 15$, $K/Y = 10$, $\langle S^z_{AFM}\rangle = \langle S^z_{FM}\rangle = \langle s^z\rangle = 0.5$, $g\mu_B H^{(A)}_{FM}/Y = 0.1$, $g\mu_B H^{(A)}_{AFM}/Y = 0.2$.

For the superlattice under consideration, the bulk spin-wave energy regions as a function of wave vector $k_x a$ for a particular choice of parameters is demonstrated in figure 2, that corresponds to $k_y a = 0$ and $-1 \le cosk_z d \le 1$ range.

The calculations show that roots of dispersion equation (9) have six positive and two negative frequencies. In addition, half of the spin-wave regions correspond to the small value of the frequency module, and half of the higher ones. The spin wave frequencies increase with increasing exchange coupling between localized spins and (s-d) or (s-f) exchange interaction of the conduction electrons spins.

The analysis of the results shows that the width of the bulk-spin wave regions in the superlattice formed ferro- and antiferromagnetic materials is depended on transverse components of wave vectors and exchange interaction.

[1] *S.J. Noh, G.H. Ahn, J.H. Seo, Zheng Gai, Ho Nyung Lee, Woo Seok Choi, S. J. Moon.* Physical Review B 2019, vol. 100 №.6.
[2] *E. Faizabadi, M. Esmaeilzadeh, F. Sattari.* The European Physical Journal B, 2012, vol. 85, 198.
[3] *Shanshan Liu, Ke Yang, Wenqing Liu, Enze Zhang, Zihan Li, Xiaoqian Zhang* and oth. National Science Review, 2019, nwz*205*.
[4] *Rui Hua Zhu, Hong Yan Peng, Mei Heng Zhang, Yu Qiang Chen.* Physica B: Condensed Matter vol. 404, 2009, issues 14–15, p. 2086-2090.
[5] *T. Jungwirth, W. A. Atkinson, B. H. Lee, and A. H. MacDonald.* Phys. Rev. B 59, 1999, 9818.
[6] *Sergio M. Rezende, Antonio Azevedo, and Roberto L. Rodríguez Suárez.* Journal of Applied Physics 126, 2019, 151101.
[7] *Qiu Rong Ke, Song Pan Pan, Zhang Zhi Dong and Guo Lian Quan.* Chinese Physics B, 2008, vol. 17, № 10.
[8] *V.A. Sanina, E.I. Golovenchits and V.G. Zalesskii.* Journal of Physics: Condensed Matter, 2012, vol. 24, № 34.
[9] *J.L. Lado and Oded Zilberberg.* Phys. Rev. Research 1, 2019, 033009.
[10] *V.A. Tanriverdiyev, V.S. Tagiyev, S.M. Seyid-Rzayeva.* Phys. Stat. Sol. (b). 2003. 240,183.
[11] *V.A. Tanriverdiyev, V.S. Tagiyev, S.M. Seyid-Rzayeva.* Fizika, 2006, vol. XII, № 4.
[12] *H.T. Diep.* Phys. Lett. A, 138, 69 (1989).
[13] *J.M. Wesselinova, E. Kroumova, N. Teofilov, and W. Nolting.* Phys. Rev. B 57, (1998). 11.
[14] *Sudha Gopalan and M. G. Cottam.* Phys. Rev. B 42, 1990, 10311.
[15] *Feng Chen, H.K. Sy.* J. Phys. Condens. Matter 7, 1995.
[16] *Yi Fang Zhou.* Phys. Lett. A, 134, 1989, 257.

Received:12.10.2020

STRUCTURE FUNCTIONS AND TWO-SPIN ASYMMETRIES IN SEMI-INCLUSIVE REACTIONS $\nu_\mu(\bar{\nu}_\mu)N \to \nu_\mu(\bar{\nu}_\mu)h^\pm X$

M.Sh. GOJAYEV
Baku State University, Azerbaijan,
AZ 1148, Baku, acad. Z. Khalilov, 23, m_qocayev@mail.ru

The structure functions and longitudinal spin asymmetries in semi-inclusive reactions $\nu_\mu(\bar{\nu}_\mu)N \to \nu_\mu(\bar{\nu}_\mu)h^\pm X$ are investigated within the framework of the Standard Model. Expressions for the non-polarization and polarization structure functions of hadrons are obtained. Within the framework of the quark-parton model, all structure functions are determined and spin asymmetries are studied in detail.

Keywords: deep inelastic scattering, structure functions, quark-parton model, two-spin asymmetry.
PACS: 12.15.-y; 13.60.-r; 13.60.+e, 14.20.Dh

1. INTRODUCTION

The Standard Model (SM), based on a local gauge theory with a symmetry group $SU_C(3)\times SU_L(2)\times U_Y(1)$, describes well the physics of elementary particles [1, 2]. There is not a single experiment in particle physics, the results of which do not agree with the predictions of the Standard Model. One of the most accurate checks of the SM was performed at the LEP and SLC electron-positron colliders. Along with electron-positron annihilation, the processes of deep inelastic scattering of leptons by nucleons play an important role in the verification of the standard model and are currently being intensively studied theoretically and experimentally [3-11]. Experiments COMPASS, HERMES, EMC, EIC, ZEUS, carried out with polarized leptons and targets, open up new possibilities for studying the internal structure of nucleons. In [10, 11], within the framework of the quark-parton model, polarization asymmetries in the processes of deep inelastic scattering of leptons by nucleons were studied. However, in these works, the non-polarization and polarization structure functions of hadrons were not considered. In the present work, we study the production of a charged $\pi^\pm$- or $K^\pm$-hadron in deep-inelastic scattering of neutrinos (antineutrinos) by polarized nucleons:

$$\nu_\mu + N(h_N) \to \nu_\mu + h^\pm + X, \qquad (1)$$

$$\bar{\nu}_\mu + N(h_N) \to \bar{\nu}_\mu + h^\pm + X, \qquad (2)$$

where h_N – is the longitudinal polarization of the target nucleon, the $h^\pm = \pi^\pm, K^\pm$, $X-$ system of undetected hadrons. The non-polarization and polarization structure functions of hadrons are introduced and analytical expressions are obtained for the differential cross sections of processes (1)-(2) and spin asymmetries.

2. KINEMATIC VARIABLES OF REACTION $\nu_\mu(\bar{\nu}_\mu)N \to \nu_\mu(\bar{\nu}_\mu)h^\pm X$

The process of deep inelastic scattering of neutrinos (antineutrinos) by nucleons with the formation of a hadron h is described by the Feynman diagram shown in Fig. 1. The shaded area shows that the target nucleon has an internal structure, which is taken into account by introducing the structure functions.

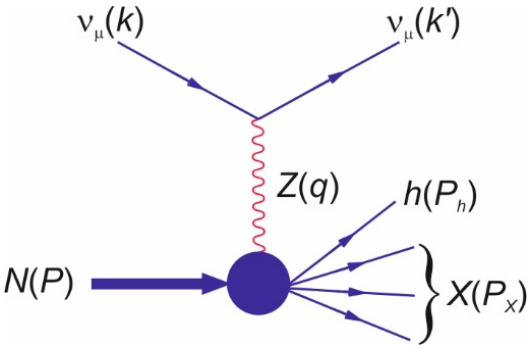

*Fig. 1.*Feynman diagram of a semi-inclusive reaction $\nu_\mu N \to \nu_\mu hX$

The semi-inclusive process $\nu_\mu + N \to \nu_\mu + h + X$ is described by the following invariant variables:

1) square of momentum transfer to hadrons

$$Q^2 = -q^2 = -(k-k')^2 \approx 4EE'\sin^2\frac{\theta}{2}, \qquad (3)$$

where $\theta-$ is the scattering angle of neutrinos, E and $E'-$ the energies of the initial and scattered neutrinos;

2) conventional kinematic variables of deep inelastic scattering

$$x = \frac{Q^2}{2(P\cdot q)},\ y = \frac{(q\cdot P)}{(k\cdot P)}; \qquad (4)$$

3) scaling variable that determines the fraction of the energy carried away by the hadron h:

$$z = \frac{(P\cdot P_h)}{(P\cdot q)}; \qquad (5)$$

4) the square of the total energy of the neutrino and target nucleon in the center of mass system:

131, H.Javid ave, AZ-1143, Baku
ANAS, Institute of Physics
E-mail: jophphysics@gmail.com

$$S = (k+P)^2 = \frac{Q^2}{xy} + M^2, \qquad (6)$$

where M – is the nucleon mass.

In the lowest order of perturbation theory, the differential effective cross section for deep inelastic neutrino scattering (it is always left-handed) by polarized nucleons can be written in the form

$$\frac{d^3\sigma(h_N)}{dxdydz} = \frac{2\pi y\alpha^2}{Q^4}\eta_Z L_{\mu\nu}H_{\mu\nu}.$$

Here

$$\eta_Z = \left(\frac{G_F M_Z^2}{2\sqrt{2}\pi\alpha}\right)^2\left(\frac{Q^2}{Q^2+M_Z^2}\right)^2,$$

G_F – Fermi constant of weak interactions, M_Z – is the mass of a charged Z-boson, $L_{\mu\nu}$ and $H_{\mu\nu}$ are the neutrino and hadron tensors.

The neutrino tensor contains symmetric and antisymmetric parts:

$$L_{\mu\nu} = 8[k_\mu k'_\nu + k'_\mu k_\nu - (k\cdot k')g_{\mu\nu} - i\varepsilon_{\mu\nu\rho\sigma}k_\rho k'_\sigma]. \qquad (9)$$

3. STRUCTURE FUNCTIONS OF A NUCLEON

The hadronic tensor $H_{\mu\nu}$ contains three non-polarization (F_1, F_2 and F_3) and five polarization (g_1, g_2, g_3, g_4 and g_5) structure functions, depending on invariant variables x, z and Q^2.

$$H_{\mu\nu} = \left(-g_{\mu\nu} + \frac{q_\mu q_\nu}{q^2}\right)F_1(x,z,Q^2) +$$
$$+ \frac{\tilde{P}_\mu\tilde{P}_\nu}{(P\cdot q)}F_2(x,z,Q^2) - i\varepsilon_{\mu\nu\alpha\beta}\frac{q_\alpha P_\beta}{2(P\cdot q)}F_3(x,z,Q^2) +$$
$$+ i\varepsilon_{\mu\nu\alpha\beta}\frac{q_\alpha}{(P\cdot q)}\left[S_\beta g_1(x,z,Q^2) + \left(S_\beta - \frac{(S\cdot q)}{(P\cdot q)}P_\beta\right)g_2(x,z,Q^2)\right] +$$
$$+ \frac{1}{(P\cdot q)}\left[\frac{1}{2}(\tilde{P}_\mu\tilde{S}_\nu + \tilde{S}_\mu\tilde{P}_\nu) - \frac{(S\cdot q)}{(P\cdot q)}\tilde{P}_\mu\tilde{P}_\nu\right]g_3(x,z,Q^2) +$$
$$+ \frac{(S\cdot q)}{(P\cdot q)}\left[\frac{\tilde{P}_\mu\tilde{P}_\nu}{(P\cdot q)}g_4(x,z,Q^2) + \left(-g_{\mu\nu} + \frac{q_\mu q_\nu}{q^2}\right)g_5(x,z,Q^2)\right]. \qquad (10)$$

Here S_μ – is the 4-vector of nucleon polarization, a $\tilde{P}_\mu$ and $\tilde{S}_\mu$ are defined as:

$$\tilde{P}_\mu = P_\mu - \frac{(P\cdot q)}{q^2}q_\mu, \quad \tilde{S}_\mu = S_\mu - \frac{(S\cdot q)}{q^2}q_\mu.$$

If the target nucleon is not polarized, then the differential cross section for deep inelastic neutrino (antineutrino) scattering by a nucleon contains non-polarization structure functions F_1, F_2 and F_3:

$$\frac{d^3\sigma}{dxdydz} = \frac{4\pi\alpha^2}{xyQ^2}\eta_Z\left[xy^2F_1 + \left(1-y-x^2y^2\frac{M^2}{Q^2}\right)F_2 \pm xy\left(1-\frac{y}{2}\right)F_3\right], \qquad (11)$$

the «+» sign corresponds to neutrino scattering, and the «–» sign corresponds to antineutrino.

In the deeply inelastic region $Q^2 >> M^2$, the differential cross section (11) usually takes the form

$$\frac{d^3\sigma}{dxdydz} = \frac{2\pi\alpha^2}{xyQ^2}\eta_Z\{[1+(1-y)^2]\cdot 2xF_1 + [1-(1-y)^2]\cdot xF_3 \pm (1-y)\cdot 2F_L\}, \qquad (12)$$

where the longitudinal structure function is:

$$F_L = F_2 - 2xF_1. \qquad (13)$$

If the nucleon is polarized, then the difference between the differential cross sections of reaction (1) for two values of the nucleon helicity is:

$$\frac{d^3\Delta\sigma}{dxdydz} = \frac{8\pi\alpha^2}{xyQ^2}\eta_Z\left\{\left[2-y-2x^2y^2\frac{M^2}{Q^2}\right]xyg_1 + 4x^3y^2\frac{M^2}{Q^2}g_2 + 2x^2y\frac{M^2}{Q^2}\times\right.$$

$$\times\left(1-y-x^2y^2\frac{M^2}{Q^2}\right)g_3+\left(1+2x^2y\frac{M^2}{Q^2}\right)\left[\left(1-y-x^2y^2\frac{M^2}{Q^2}\right)g_4+xy^2g_5\right]\Bigg\}. \qquad (14)$$

At $Q^2 >> M^2$, the contribution to the cross section of the polarization structure functions g_2 and g_3 vanishes:

$$\frac{d^3\Delta\sigma}{dxdydz}=\frac{8\pi\alpha^2}{xyQ^2}\eta_Z\{[1+(1-y)^2]\cdot xg_5+[1-(1-y)^2]\cdot xg_1+(1-y)g_L\}, \qquad (15)$$

where

$$g_L=g_4-2xg_5. \qquad (16)$$

Let us find the structure functions of hadrons in the quark-parton model. According to this model:

1) the nucleon consists of valence quarks and a quark-antiquark sea. In the region of deep-inelastic scattering, there is no interaction between partons, they behave like free particles;

2) in the Breit system, the momenta of partons are directed in the direction of the momentum of the nucleon and each parton carries a certain fraction of the momentum of the nucleon;

3) a neutral intermediate Z-boson interacts with a parton that has a fraction of the momentum of a nucleon x and transfers momentum q to it, and all other partons simply observe the process.

Parton subprocesses of deep inelastic reactions (1) and (2) are neutrino (antineutrino) quark and antiquark scattering:

$$\nu_\mu(\overline{\nu}_\mu)+q\to\nu_\mu(\overline{\nu}_\mu)+q,\quad \nu_\mu(\overline{\nu}_\mu)+\overline{q}\to\nu_\mu(\overline{\nu}_\mu)+\overline{q}\,.$$

The Feynman diagram of neutrino-quark scattering is shown in Fig. 2.

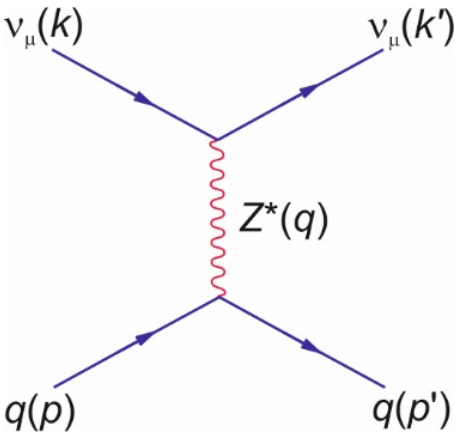

Fig. 2. Feynman diagram reaction $\nu_\mu q\to\nu_\mu q$.

Calculation of this diagram leads to the following structure functions:

$$F_1=\sum_q[g_L^2(q)+g_R^2(q)][f_q^N(x)D_q^h(z)+f_{\overline{q}}^N(x)D_{\overline{q}}^h(z)],$$

$$F_2=2x\sum_q[g_L^2(q)+g_R^2(q)][f_q^N(x)D_q^h(z)+f_{\overline{q}}^N(x)D_{\overline{q}}^h(z)],$$

$$F_3=\sum_q[g_L^2(q)-g_R^2(q)][f_q^N(x)D_q^h(z)-f_{\overline{q}}^N(x)D_{\overline{q}}^h(z)],$$

$$g_1=\sum_q[g_L^2(q)+g_R^2(q)][\Delta f_q^N(x)D_q^h(z)+\Delta f_{\overline{q}}^N(x)D_{\overline{q}}^h(z)], \qquad (17)$$

$$g_4=2x\sum_q[g_L^2(q)-g_R^2(q)][-\Delta f_q^N(x)D_q^h(z)+\Delta f_{\overline{q}}^N(x)D_{\overline{q}}^h(z)],$$

$$g_5=\sum_q[g_L^2(q)-g_R^2(q)][-\Delta f_q^N(x)D_q^h(z)+\Delta f_{\overline{q}}^N(x)D_{\overline{q}}^h(z)],$$

where $g_L(q)=\pm\frac{1}{2}-Q_q\sin^2\theta_W$ and $g_R(q)=-Q_q\sin^2\theta_W$ – are the left and right coupling constants of a quark with a Z-boson (the «±» sign corresponds to an up and down quark, respectively), $f_q^N(x)$ ($f_{\overline{q}}^N(x)$) – the distribution function of a quark q (antiquark $\overline{q}$) in a nucleon N, $D_q^h(z)$ ($D_{\overline{q}}^h(z)$) – is a function of fragmentation of a quark q (antiquark $\overline{q}$) into a hadron h, $\Delta f_q^N(x)=f_q^+(x)-f_q^-(x)$, ($\Delta f_{\overline{q}}^N(x)=f_{\overline{q}}^+(x)-f_{\overline{q}}^-(x)$), $f_q^+(x)$ ($f_{\overline{q}}^+(x)$)

and $f_q^-(x)$ ($f_{\bar{q}}^-(x)$) – determines the distribution of a quark q (antiquark $\bar{q}$) with positive and negative helicity in a nucleon with positive helicity.

In the quark-parton model, there are connections between the structure functions:

$$F_L = F_2 - 2xF_1 = 0, \quad g_L = g_4 - 2xg_5 = 0.$$

Thus, as in the case of non-polarization structure functions F_1 and F_3, there are only two polarization structure functions g_1 and g_5. Of these, F_1 and g_1 they preserve P-parity, a F_3 and g_5 – violate.

In the quark-parton model, the structure functions are only functions of the invariants x and z, and they do not depend on the square of the momentum transfer Q^2. This property is due to the fact that in the Breit system the transverse momenta of partons are very small. In quantum chromodynamics, the emission of hard gluons by quarks leads to a logarithmic violation of scaling. As the Q^2 increases, the number of emitted gluons increases, which leads to an increase in $q\bar{q}$-quark pairs and the gluon distribution density.

In deep inelastic scattering of neutrinos (antineutrinos) by a polarized nucleon target, the main observables are the two-spin asymmetries

$$A_N^{h\pm} = \frac{\sigma_{\uparrow\uparrow}^{h^\pm} - \sigma_{\uparrow\downarrow}^{h^\pm}}{\sigma_{\uparrow\uparrow}^{h^\pm} + \sigma_{\uparrow\downarrow}^{h^\pm}}, \tag{18}$$

$$A_N^{h^+-h^-} = \frac{(\sigma_{\uparrow\uparrow}^{h^+} - \sigma_{\uparrow\uparrow}^{h^-}) - (\sigma_{\uparrow\downarrow}^{h^+} - \sigma_{\uparrow\downarrow}^{h^-})}{(\sigma_{\uparrow\uparrow}^{h^+} - \sigma_{\uparrow\uparrow}^{h^-}) + (\sigma_{\uparrow\downarrow}^{h^+} - \sigma_{\uparrow\downarrow}^{h^-})}, \tag{19}$$

where $\sigma_{\uparrow\uparrow}^h$ and $\sigma_{\uparrow\downarrow}^h$ are the differential cross sections for the production of a semi-inclusive hadron h in the parallel (antiparallel) direction of the spins of the neutrino or antineutrino and the target nucleon.

The two-spin asymmetries $A_N^{h^+}$ and $A_N^{h^-}$ depend both on the distribution functions of quarks in a nucleon and on the functions of fragmentation of quarks into a hadron h.

For example, if we neglect the contribution of sea quarks, then for the asymmetry in the scattering of neutrinos on an isoscalar target, we can obtain the formula:

4. SPIN ASYMMETRIES

$$A_d^{\pi^+} = \frac{\Delta u_\upsilon(x) + \Delta d_\upsilon(x)}{u_\upsilon(x) + d_\upsilon(x)} \frac{D_u^{\pi^+}(z)[g_L^2(u) - (1-y)^2 g_R^2(u)] + D_d^{\pi^+}(z)[g_L^2(d) - (1-y)^2 g_R^2(d)]}{D_u^{\pi^+}(z)[g_L^2(u) + (1-y)^2 g_R^2(u)] + D_d^{\pi^+}(z)[g_L^2(d) + (1-y)^2 g_R^2(d)]}. \tag{20}$$

Here $u_\upsilon(x)$ and $d_\upsilon(x)$ – are the distribution functions of valence u- and d-quarks in a proton. Under the condition $y \to 1$, spin asymmetry (20) depends only on the distribution functions of valence u- and d-quarks in the proton:

$$A_d^{\pi^+}(y \to 1) = \frac{\Delta u_\upsilon(x) + \Delta d_\upsilon(x)}{u_\upsilon(x) + d_\upsilon(x)}. \tag{21}$$

Another two-spin asymmetry $A_N^{h^+-h^-}$ does not depend on the functions of quark fragmentation into a hadron h; they are the distribution functions of quarks in a nucleon (the contribution of sea quarks is not taken into account):

$$A_p^{\pi^+-\pi^-} = -\frac{\Delta u_\upsilon(x)[g_L^2(u) - (1-y)^2 g_R^2(u)] - \Delta d_\upsilon(x)[g_L^2(d) - (1-y)^2 g_R^2(d)]}{u_\upsilon(x)[g_L^2(u) + (1-y)^2 g_R^2(u)] + d_\upsilon(x)[g_L^2(d) + (1-y)^2 g_R^2(d)]}, \tag{22}$$

$$A_p^{K^+-K^-} = -\frac{\Delta u_\upsilon(x)[g_L^2(u) - (1-y)^2 g_R^2(u)]}{u_\upsilon(x)[g_L^2(u) + (1-y)^2 g_R^2(u)]}. \tag{23}$$

Under the condition $y \to 1$, the asymmetry $A_p^{K^+-K^-}$ depends only on the distribution functions of the valence u-quark in the proton

$$A_p^{K^+-K^-} = -\frac{\Delta u_\upsilon(x)}{u_\upsilon(x)}. \tag{24}$$

We have obtained expressions for the two-spin asymmetries $A_p^{\pi^+-\pi^-}$ и $A_p^{K^+-K^-}$ in processes $\nu_\mu + p \to \nu_\mu + \pi^\pm + X$ and $\nu_\mu + p \to \nu_\mu + K^\pm + X$ taking into account the contribution of sea quarks (integrated over the variable y):

$$A_p^{\pi^+-\pi^-}(\nu_\mu p) = \{\Delta u_\upsilon(x)[3g_L^2(u) - g_R^2(u)] - \Delta d_\upsilon(x)[3g_L^2(d) - g_R^2(d)] + 4\Delta u_s(x)[g_L^2(u) - g_R^2(u)] -$$

$$-4\Delta d_s(x)[g_L^2(d)-g_R^2(d)]\}\quad\{u_\upsilon(x)[3g_L^2(u)+g_R^2(u)]-d_\upsilon(x)[3g_L^2(d)+g_R^2(d)]+$$
$$+2u_s(x)[g_L^2(u)-g_R^2(u)]-2d_s(x)[g_L^2(d)-g_R^2(d)]\}^{-1}; \qquad (25)$$

$$A_p^{K^+-K^-}=\{\Delta u_\upsilon(x)[3g_L^2(u)-g_R^2(u)]+4\Delta u_s(x)[g_L^2(u)-g_R^2(u)]-4\Delta s(x)[g_L^2(u)-g_R^2(u)]\}\times$$
$$\times\{u_\upsilon(x)[3g_L^2(u)+g_R^2(u)]+2u_s(x)[g_L^2(u)-g_R^2(u)]-2s(x)[g_L^2(d)-g_R^2(d)]\}^{-1}, \qquad (26)$$

here $u_\upsilon(x)$, $d_\upsilon(x)$ and $s_s(x)$ – distribution function of valence u-, d- and sea s-quarks in a proton.

Formulas for asymmetries $A_p^{\pi^+-\pi^-}$ and $A_p^{K^+-K^-}$ in the processes of deep inelastic scattering of antineutrinos $\overline{\nu}_\mu + p \to \overline{\nu}_\mu + \pi^\pm + X$ and $\overline{\nu}_\mu + p \to \overline{\nu}_\mu + K^\pm + X$ are obtained from (25) and (26) by simple changes $g_L \leftrightarrow g_R$.

5. ANALYSIS OF THE OBTAINED RESULTS

We pass to the estimation of the spin asymmetries $A_N^{h^\pm}$ and $A_N^{h^+-h^-}$. For this purpose, we used the distribution functions of quarks in a proton given in [4, 12, 13]

In fig. 3 shows the dependence of the asymmetry $A_d^{\pi^+}(y\to 1)$ (formula (21)) on the variable x. As follows from the figure, this asymmetry is positive and monotonically increases with increasing variable x. With $x=0.1$ the asymmetry is 10%, and with $x=0.9$ the value it reaches 90%.

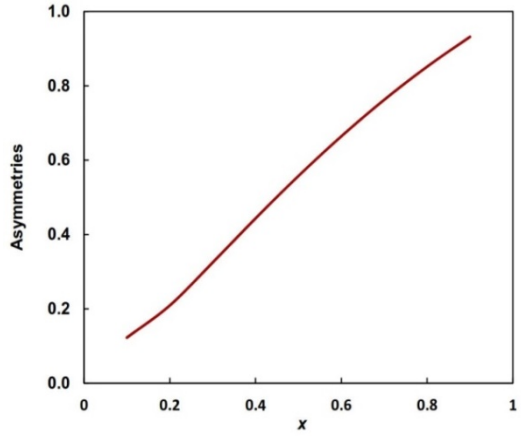

Fig. 3. Dependence of asymmetry $A_d^{\pi+}$ on variable x.

Fig. 4 illustrates the dependence of the two-spin asymmetry $A_p^{K^+-K^-}$ in processes $\nu_\mu + p \to \nu_\mu + K^\pm + X$ on the variable x at various fixed values y: $y=0.1$ (curve 1), $y=0{,}4$ (curve 2), and $y=0{,}4$ (curve 3). As you can see, with an increase in the variable x, the asymmetry first sharply decreases and, reaching a minimum near it $x\approx 0{,}2$, begins to grow. The graphs plotted at the Weinberg parameter $\sin^2\theta_W = 0.232$ value. The figure also shows that an increase in the variable y leads to an increase in the two-spin asymmetry $A_p^{K^+-K^-}$.

In fig. 5 shows the dependence of asymmetry $A_p^{K^+-K^-}$ in processes $\nu_\mu + p \to \nu_\mu + K^\pm + X$ and $\overline{\nu}_\mu + p \to \overline{\nu}_\mu + K^\pm + X$ on a variable x. In the process $\nu_\mu + p \to \nu_\mu + K^\pm + X$, the asymmetry is positive and increases with the growth of the variable x. In the process $\overline{\nu}_\mu + p \to \overline{\nu}_\mu + K^\pm + X$, the asymmetr is negative and an increase x leads to a decrease in asymmetry.

CONCLUSION

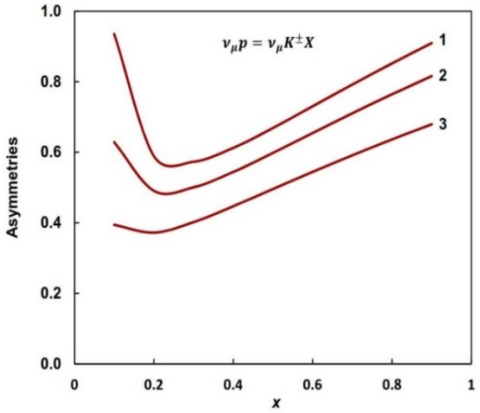

Fig. 4. Dependence of asymmetry $A_p^{K^+-K^-}(\nu_\mu p)$ at x.

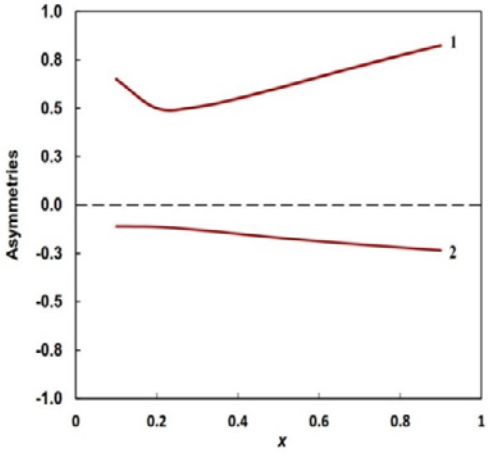

Fig. 5. Dependence of asymmetry $A_p^{K^+-K^-}$ on variable x in reactions $\nu_\mu p \to \nu_\mu K^\pm X$ (curve 1) and $\overline{\nu}_\mu p \to \overline{\nu}_\mu K^\pm X$ (curve 2).

By introducing non-polarization and polayrization structure functions, differential cross sections of deep inelastic processes $\nu_\mu + N \to \nu_\mu + h^\pm + X$ and $\overline{\nu}_\mu + N \to \overline{\nu}_\mu + h^\pm + X$ obtained. Two-spin asymmetries $A_N^{h^+}$, $A_N^{h^-}$ and $A_N^{h^+-h^-}$ are determined. In the quark-parton model, structure functions found, and the dependence of two-spin asymmetries on the invariant variable x is investigated. The results illustrated with graphs.

[1] *J. Beringer et al.* (Particle Data Group Collaboration). 2012, Phys. Rev., D 86, 010001.
[2] *S.K. Abdullaev.* Standard model, properties of leptons and quarks (in Azerb.). Baku, Zeka Print, 2017, 276 p.
[3] *P.J. Mulders.* Polarized structure functions. Progress in Particle and Nuclear Physics, 2005, №55, p.243-269.
[4] *D. De Florian, G.A. Navarro, R. Sassot.* Sea quarks and gluon polarization in the nucleon at NLO accuracy. Phys. Rev., 2005, v. D 71, 094018, p. 1-12
[5] *Y. Koike, J. Nagashima.* Double spin asymmetries for large-p_T hadron production in semi-inclusive DIS. arxiv: hep-ph/0302061, 2003, v.2, p.1-25.
[6] *I.A. Savin.* COMPASS results on the nucleon spin structure. Nuclear Physics B (Proceedings Supplements), 2011, 219-220, 94-101pp.
[7] *K. Nikolayev.* The polarized valence quark distribution from COMPASS. Spin-Praha-2007.
[8] HERMES Collaboration. Quark helicity distributions in the nucleon for up, down, and strange quarks from semi-inclusive deep-inelastic scattering. Phys. Rev., 2005, D71, p. 012003.
[9] COMPASS Collaboration *(Alexakhin, V.Yu. et al.)* The Deuteron Spin-dependent Structure Function g_1(d) and its First Moment Phys. Lett., 2007, B 647, p. 8-17.
[10] *S.K. Abdullayev.* Double-spin asymmetries in semi-inclusive DIS // Azerbaijan Journal of Physics, Fizika, Baku, 2013, V. XIX, №3, p.19-24.
[11] *S.K. Abdullayev, A.I. Mukhtarov, M.Sh. Gojayev.* Double-spin asymmetries in semi-inclusive DIS Azerbaijan Journal of Physics, Fizika, Baku, 2009, V. XV, №1, p.61-67.
[12] *D. De Florian, G.A. Navarro, R. Sassot.* Sea quarks and gluon polarization in the nucleon at NLO accuracy Phys. Rev., 2005, D71, p.094018-1-12.
[13] *D. De Florian, R. Sassot, M. Stratmann.* Global analysis of fragmentation functions for pions and kaons and their uncertainties Phys. Rev. 2007, v. D 75, p. 114010.

Received:19.10.2020

THE PRODUCTION OF A CHARGINO PAIR IN POLARIZED LEPTON-ANTILEPTON COLLISIONS (I)

S.K. ABDULLAYEV, M.Sh. GOJAYEV, A.K. GULAYEVA
Baku State University, Azerbaijan, AZ 1148, Baku,
acad. Z. Khalilov, 23, m_qocayev@mail.ru

In the framework of the Minimal Supersymmetric Standard Model, the processes of annihilation of an arbitrarily polarized lepton-antilepton pair into a pair of charginos are considered: $\ell^- + \ell^+ \to \tilde{\chi}_i^- + \tilde{\chi}_j^+$. A general expression is obtained for the cross section of the process in the case of arbitrarily polarized initial particles. The angular and polarization characteristics of the process have been studied in detail. In particular, it is shown that the asymmetry arising in the interaction of longitudinally polarized electrons with unpolarized positrons is equal in magnitude and opposite in sign of the asymmetry arising in the interaction of polarized positrons with unpolarized electrons.

Keywords: Minimal Supersymmetric Standard Model, Standard Model, lepton-antilepton pair, chargino, longitudinal polarization, transverse polarization.
PACS: 12.10.−g, 12.15.-y, 12.60.−i, 14.80.Ly, 14.70.Bh, 14.70.Hp.

1. INTRODUCTION

The discovery of the Higgs boson H_{SM} at the Large Hadron Collieder (LHC) by the ATLAS and CMS collaborations [1, 2] (see also reviews [3-5]) began a new chapter in the history of elementary particle physics. The mechanism of the generation of masses of fundamental particles - the mechanism of spontaneous breaking of the Braut – Englert – Higgs symmetry [6, 7] was experimentally confirmed. Thus, the Standard Model (CM) of fundamental interactions received its logical conclusion and acquired the status of a standard theory.

According to the SM, there are six quarks and six leptons in nature, making up three generations and three types of interactions: strong, electromagnetic and weak, which are transported by gluons, photons and $W^{\pm}$, Z -bosons. Now a fourth, the Yukawa interaction, carried by the Higgs boson, has been added to them. Based on the CM, one can accurately calculate Feynman diagrams of various processes and compare them with the corresponding experimental data. The agreement between CM and experience is strikingly good.

Despite the successes of SM, this theory has its own difficulties. Many of them are related to the fact that this theory describes a lot, but does not explain where it came from, does not allow it to be derived from deeper principles. One of the mysteries of the SM is the very large spread of masses of fundamental fermions - quarks and leptons. The mass of the electron is the smallest ($m_e = 5 \cdot 10^{-4}$ GeV), and the mass of the top quark is the largest ($m_t = 173.2$ GeV). Their masses differ hundreds of thousands of times. The masses of all SM particles are scattered over a very wide range (see Fig. 1).

This situation looks abnormal. Physicists are trying to figure out if there is some mechanism that naturally leads to such a spread of masses. Within the framework of the SM, such a hierarchy of masses does not receive a satisfactory explanation; however, in some non-standard models a similar hierarchy of masses may arise.

In quantum field theory, it turns out that the vacuum is not an absolute emptiness, but a ceaselessly seething sea of virtual particles. These virtual particles of various kinds appear for a short moment and then disappear. However, if there is some real particle in a vacuum, then virtual particles envelop it and change its properties. All the particles of our world are particles dressed in a virtual fur coat. Masses, charges and all other characteristics of the observed particles these are the characteristics of the particles dressed in a fur coat.

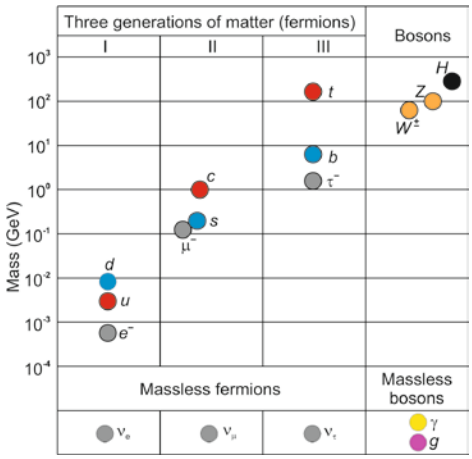

Fig. 1. Particle masses of the Standard Model.

This phenomenon is taken into account by a mathematical procedure called renormalization. For all SM particles, renormalization works well, but in the case of the Higgs boson, a problem arises: the effect of virtual particles on the Higgs boson mass is too large, the boson mass increases by a factor of trillions, and such a particle can no longer play the role of the Higgs boson. Inside the SM, there is no restraining factor that stops the growth of the Higgs boson mass due to virtual particles. This difficulty is called the hierarchy problem. Here such a way out of the difficult situation is possible. If there are some

131, H.Javid ave, AZ-1143, Baku
ANAS, Institute of Physics
E-mail: jophphysics@gmail.com

other particles in nature that are absent in the SM, then in virtual form they can compensate for the effect on the Higgs boson mass. The most important thing here is that in models of physics outside the SM, for example, in the Minimal Supersymmetric Standard Model (MSSM), such compensation itself arises from the construction of the theory.

The absence of dark matter particles in the SM is also one of the difficulties of this theory. In astrophysics, it is believed that in the Universe, in addition to ordinary matter in the form of planets, stars, black holes, gas and dust clouds, neutrinos, etc., there are also particles of a completely different nature. These particles practically do not interact with ordinary matter and radiation. There is not a single particle in the SM that is suitable for this role. However, in the MSSM there are new particles called neutralino, sneutrino, gluino, gravitino, which can be candidates for dark matter.

All the above facts and a number of other reasons indicate the need to go beyond the SM. At the same time, special attention is paid to the MSSM. In this model, two doublets of the scalar field are introduced and after spontaneous symmetry breaking, five Higgs bosons appear: CP-even H - and h - bosons, CP-odd A-boson and charged $H^{\pm}$-bosons. The Higgs sector is characterized by the parameters $M_H, M_h, M_A, M_{H^{\pm}}, \alpha$ and β (α and β are the mixing angles of the scalar fields). Of these, the parameters M_A and $tg\beta = \frac{\upsilon_2}{\upsilon_1}$ are assumed to be free (υ_1 and υ_2 are the vacuum values of the neutral scalar fields). The rest of the parameters are expressed through M_A and β:

$$M^2_{H(h)} = \frac{1}{2}[M^2_A + M^2_Z \pm \sqrt{(M^2_A + M^2_Z)^2 - 4M^2_A M^2_Z \cos^2 2\beta}],$$

$$M^2_{H^{\pm}} = M^2_A + M^2_W,$$

$$\mathrm{tg}2\alpha = \mathrm{tg}2\beta \cdot \frac{M^2_A + M^2_Z}{M^2_A - M^2_Z} \quad \left(-\frac{\pi}{2} \le \alpha \le 0\right).$$

Here M_Z and M_W are the masses of gauge Z - and $W^{\pm}$-bosons.

The supersymmetric (SUSY) partners of gauge $W^{\pm}$-bosons and Higgs $H^{\pm}$-bosons are calibrino $\tilde{W}^{\pm}$ and Higgsino $\tilde{H}^{\pm}$. These spinor fields mix and create new mass states called charginos $\tilde{\chi}^{\pm}_{1,2}$. Chargino's mass matrix depends on the mass parameters of wine and Higgsino, as well as on the parameter M_2 and μ [8, 9, 11]:

$$M_C = \begin{pmatrix} M_2 & \sqrt{2}M_W \sin\beta \\ \sqrt{2}M_W \cos\beta & \mu \end{pmatrix}.$$

This matrix is diagonalized by two real two-row matrices U and V:

$$UM_C V^{-1} \Rightarrow U = R\_, \; V = \begin{cases} R_+, \; if \;\; \det M_C > 0 \\ \sigma_3 R_+, \; if \;\; \det M_C < 0 \end{cases},$$

where $\sigma_3 -$ is the Pauli matrix making the chargino mass positive R_+ and $R_- -$ the rotation matrix with angles θ_+ and θ_-:

$$\mathrm{tg}2\theta_+ = \frac{2\sqrt{2}M_W(M_2 \sin\beta + \mu\cos\beta)}{M^2_2 - \mu^2 + 2M^2_W \cos\beta},$$

$$\mathrm{tg}2\theta_- = \frac{2\sqrt{2}M_W(M_2 \cos\beta + \mu\sin\beta)}{M^2_2 - \mu^2 - 2M^2_W \cos\beta}.$$

This leads to two mass states of charginos:

$$m^2_{\tilde{\chi}^{\pm}_{1,2}} = \frac{1}{2}\{M^2_2 + \mu^2 + 2M^2_W \mp [(M^2_2 - \mu^2)^2 + 4M^2_W(M^2_W \cos^2 2\beta + M^2_2 + \mu^2 + 2M_2\mu \sin 2\beta)]^{1/2}\}.$$

When $|\mu| \to \infty$ we have:

$m_{\tilde{\chi}^{\pm}_1} \approx M_2, \quad m_{\tilde{\chi}^{\pm}_2} \approx |\mu|,$

this means that a light chargino corresponds to a wino state, and a heavy chargino corresponds to a Higgsino state. In the case $M_2 >> |\mu|$, $M_W -$ of light and heavy charginos, they exchange roles:

$$m_{\tilde{\chi}^{\pm}_i} \approx |\mu|, \quad m_{\tilde{\chi}^{\pm}_2} \approx M_2.$$

The neutral analogs of the charginos are called neutralino, there are four of them: $\tilde{\chi}^0_j \; (j = 1,2,3,4)$. They arise from the mixing of bino $\tilde{B}^0$, wino $\tilde{W}^0_3$ and Higgsino $\tilde{H}^0_1$ and $\tilde{H}^0_2$.

Charginos and neutralinos can be born in the LHC in the decays of squarks and gluinos: $\tilde{g} \to q + \tilde{q}$ and $\tilde{q} \to q + \tilde{\chi}_i$. The joint production of a pair of neutralinos in quark-antiquark collisions in hadron colliders $q + \bar{q} \to \tilde{\chi}^0_i + \tilde{\chi}^0_j$ was considered in [12]. The process of production of a pair of different neutralinos in the collision of polarized electrons and positrons has been studied in a number of works [13-18].

In this paper, we consider the production of a pair of charginos in arbitrarily polarized lepton-antilepton (electron-positron or muon-antimuon) collisions ($\ell^-\ell^+ \to e^-e^+, \mu^-\mu^+$):

$$\ell^- + \ell^+ \to \tilde{\chi}_i^- + \tilde{\chi}_j^+, \qquad (1)$$

Cases of annihilation of a longitudinally and transversely polarized lepton-antilepton pair are considered separately. The degrees of longitudinal and transverse polarization of the chargino were also determined during the annihilation of a longitudinally polarized lepton and an unpolarized antilepton.

2. THE AMPLITUDE AND CROSS SECTION OF THE PROCESS $\ell^-\ell^+ \to \tilde{\chi}_i^-\tilde{\chi}_j^+$

Within the framework of the MSSM, the process of annihilation of a lepton-antilepton pair into a chargino pair is described by the Feynman diagrams shown in Fig. 2: a) s-channel diagrams with the exchange of a photon and a Z-boson; b) s-channel diagrams with the exchange of Higgs bosons H , h or A; c) t-channel diagram with scalar neutrino $\tilde{\nu}_L$ exchange.

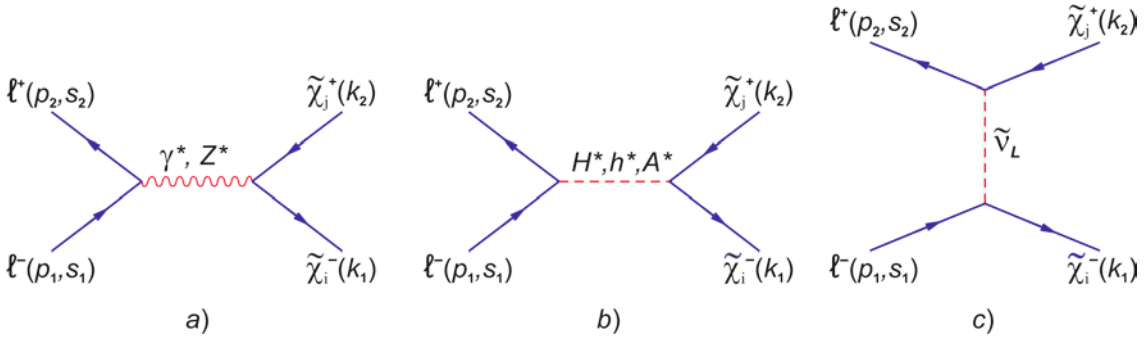

Fig. 2. Feynman diagrams for reaction $\ell^-\ell^+ \to \tilde{\chi}_i^-\tilde{\chi}_j^+$.

Consider the diagram a) with the exchange of a photon and a Z-boson. The amplitude corresponding to these diagrams can be represented as:

$$M_{i\to f} = M^{(\gamma)} + M^{(Z)},$$

$$M^{(\gamma)} = i\frac{e^2}{s}[\bar{\upsilon}_e(p_2,s_2)\gamma_\mu u_e(p_1,s_1)][\bar{u}_{\chi_i}(k_1)\gamma_\mu \upsilon_{\chi_j}(k_2)], \qquad (2)$$

$$M^{(Z)} = \frac{ig_Z^2}{(s-M_Z^2+iM_Z\Gamma_Z)}\{\bar{\upsilon}_e(p_2,s_2)\gamma_\mu[g_L(1+\gamma_5)+g_R(1-\gamma_5)]u_e(p_1,s_1)\}\times$$
$$\times[\bar{u}_{\chi_i}(k_1)\gamma_\mu(g^L_{\chi_i^-\chi_j^+Z}P_L + g^R_{\chi_i^-\chi_j^+Z}P_R)\upsilon_{\chi_j}(k_2)], \qquad (3)$$

where $s=(p_1+p_2)^2=(k_1+k_2)^2$ – is the square of the total energy of the lepton-antilepton pair in the center of mass system; $p_1(s_1)$ and $p_2(s_2)$ – 4-vectors of the momentum (polarization) of the lepton and antilepton; g_Z – weak coupling constant

$$g_Z^2 = \frac{e^2}{4x_W(1-x_W)}; \qquad (4)$$

$x_W = \sin^2\theta_W$ – Weinberg parameter; g_L and g_R – are the left and right constants of interaction of a lepton with a Z-boson

$$g_L = -\frac{1}{2} + x_W, \qquad g_R = x_W; \qquad (5)$$

$P_{L(R)} = (1\pm\gamma_5)/2$ – chirality matrices; $g^L_{\tilde{\chi}_i^-\tilde{\chi}_j^+Z} = G_L$ and $g^R_{\tilde{\chi}_i^-\tilde{\chi}_j^+Z} = G_R$ – are the left and right constants of interaction of the chargino with the vector -boson (they are given [8]):

$$G_L = \frac{1}{\cos\theta_W}\left[\delta_{ij}\sin^2\theta_W - \frac{1}{2}V_{i2}V_{j1} + V_{i1}V_{j1}\right],$$
$$G_R = \frac{1}{\cos\theta_W}\left[\delta_{ij}\sin^2\theta_W - \frac{1}{2}U_{i2}U_{j1} - U_{i1}U_{j1}\right]. \qquad (6)$$

The square of the process amplitude is:

$$\left|M_{i\to f}\right|^2 = \left|M^{(\gamma)}\right|^2 + \left|M^{(Z)}\right|^2 + M^{+(\gamma)}M^{(Z)} + M^{+(Z)}M^{(\gamma)}, \qquad (7)$$

here $\left|M^{(\gamma)}\right|^2$ and $\left|M^{(Z)}\right|^2$ – are the contributions of the diagrams with the exchange of a photon and Z-boson,

$(M^{+(\gamma)}M^{(Z)} + M^{+(Z)}M^{(\gamma)})$ – is the interference of these diagrams. The expressions for these quantities are given in the Appendix.

The differential effective cross section of the reaction is expressed by the formula

$$d\sigma = \frac{1}{2s}\left|M_{i\to f}\right|^2 (2\pi)^4 \delta(p_1 + p_2 - k_1 - k_2)\frac{d\mathrm{k}_1}{(2\pi)^3 \cdot 2\varepsilon_1}\frac{d\mathrm{k}_2}{(2\pi)^3 \cdot 2\varepsilon_2}, \qquad (8)$$

where $\varepsilon_1(\vec{k}_1)$ and $\varepsilon_2(\vec{k}_2)$ – are the energies (impulses) of the chargino $\tilde{\chi}_i^-$ and $\tilde{\chi}_j^+$. After integrating over the chargino $\tilde{\chi}_j^+$ impulses and over the chargino $\tilde{\chi}_i^-$ energy, we obtain the following expression for the differential cross section of the considered reaction in the center of mass system

$$\frac{d\sigma}{d\Omega} = \frac{\left|M_{i\to f}\right|^2}{64\pi^2 s}\cdot\sqrt{\lambda(r_{\chi_i}, r_{\chi_j})}, \qquad (9)$$

Here $d\Omega = \sin\theta d\theta d\varphi -$ is the solid angle of departure of the chargino $\tilde{\chi}_i^-$; $\theta -$ the polar angle between the directions of the lepton and chargino $\tilde{\chi}_i^-$ pulses, $\varphi -$ the azimuthal angle of departure of the chargino; $\lambda(r_{\chi_i}, r_{\chi_j})$ – is the known kinematic function of the two-particle phase volume

$$\lambda(r_{\chi_i}, r_{\chi_j}) = (1 - r_{\chi_i} - r_{\chi_j})^2 - 4r_{\chi_i} r_{\chi_j}, \qquad (10)$$

where the notation are introduced:

$$r_{\chi_i} = \left(\frac{m_{\chi_i}}{\sqrt{s}}\right)^2, \qquad r_{\chi_j} = \left(\frac{m_{\chi_j}}{\sqrt{s}}\right)^2.$$

Using the expressions $\left|M^{(\gamma)}\right|^2$, $\left|M^{(Z)}\right|^2$ and $(M^{+(\gamma)}M^{(Z)} + M^{+(Z)}M^{(\gamma)})$ given in the Appendix, we obtain the following expressions for the differential cross sections of the process $\ell^- + \ell^+ \to \tilde{\chi}_i^- + \tilde{\chi}_j^+$:

$$\frac{d\sigma^{(\gamma)}}{d\Omega} = \frac{\alpha_{\mathrm{QED}}^2}{16s}\sqrt{\lambda(r_{\chi_i}, r_{\chi_j})}\{(1-\lambda_1\lambda_2)[(1 + r_{\chi_i} - r_{\chi_j})(1 - r_{\chi_i} + r_{\chi_j}) + \lambda(r_{\chi_i}, r_{\chi_j})\cos^2\theta + 8\sqrt{r_{\chi_i} r_{\chi_j}}] +$$
$$+ \lambda(r_{\chi_i}, r_{\chi_j})\sin^2\theta\cos(2\varphi - \phi)\cdot\eta_1\eta_2\}, \qquad (11)$$

$$\frac{d\sigma^{(Z)}}{d\Omega} = \frac{\alpha_{\mathrm{QED}}^2 \cdot s}{32[(s - M_Z^2)^2 + \Gamma_Z^2 M_Z^2]}\frac{\sqrt{\lambda(r_{\tilde{\chi}_j}, r_V)}}{x_W^2(1 - x_W)^2}\times$$
$$\times\{(G_L^2 + G_R^2)[g_L^2(1-\lambda_1)(1+\lambda_2) + g_R^2(1+\lambda_1)(1-\lambda_2)][(1 + r_{\chi_i} - r_{\chi_j})(1 - r_{\chi_i} + r_{\chi_j}) + \lambda(r_{\chi_i}, r_{\chi_j})\cos^2\theta] +$$
$$+ g_L g_R \lambda(r_{\chi_i}, r_{\chi_j})\sin^2\theta\cos(2\varphi - \phi)\cdot\eta_1\eta_2\} + 2(G_L^2 - G_R^2)[g_L^2(1-\lambda_1)(1+\lambda_2) - g_R^2(1+\lambda_1)(1-\lambda_2)]\times$$
$$\times\sqrt{\lambda(r_{\chi_i}, r_{\chi_j})}\cos\theta + 8G_L G_R\sqrt{r_{\chi_i} r_{\chi_j}}[g_L^2(1-\lambda_1)(1+\lambda_2) + g_R^2(1+\lambda_1)(1-\lambda_2)]\}. \qquad (12)$$

$$\frac{d\sigma^{(I)}}{d\Omega} = \frac{\alpha_{\mathrm{QED}}^2}{16x_W(1 - x_W)}\frac{s - M_Z^2}{(s - M_Z^2)^2 + \Gamma_Z^2 M_Z^2}\sqrt{\lambda(r_{\chi_i}, r_{\chi_j})}\times$$
$$\times\{(G_L + G_R)[g_L(1-\lambda_1)(1+\lambda_2) + g_R(1+\lambda_1)(1-\lambda_2)][(1 + r_{\chi_i} - r_{\chi_j})(1 - r_{\chi_i} + r_{\chi_j}) +$$
$$+ \lambda(r_{\chi_i}, r_{\chi_j})\cos^2\theta + 8\sqrt{r_{\chi_i} r_{\chi_j}}] + \lambda(r_{\chi_i}, r_{\chi_j})\sin^2\theta\cos(2\varphi - \phi)\cdot\eta_1\eta_2\} +$$
$$+ 2(G_L - G_R)[g_L(1-\lambda_1)(1+\lambda_2) - g_R(1+\lambda_1)(1-\lambda_2)]\sqrt{\lambda(r_{\chi_i}, r_{\chi_j})}\cos\theta. \qquad (13)$$

Here λ_1 and λ_2 – are the helicities of the lepton and antilepton, $\vec{\eta}_1$ and $\vec{\eta}_2$ – are the transverse components of their spin vectors, $\phi -$ the angle between the transverse spin vectors of the lepton $\vec{\eta}_1$ and antilepton $\vec{\eta}_2$, and $\Gamma_Z -$ the total width of the Z-boson decay. At high energies of lepton-antilepton beams ($s >> M_Z^2$), the contribution of the diagram with Z-boson exchange prevails over the contribution of the electromagnetic mechanism. In this regard, let us analyze the cross section of the Z-boson mechanism (12) in various cases of particle polarizations.

3. THE CASE OF LONGITUDINAL POLARIZATION OF PARTICLES

Differential cross section (12) in the case of longitudinally polarized lepton-antilepton beams has the following form:

$$\frac{d\sigma(\lambda_1,\lambda_2)}{d\Omega} = \frac{\alpha_{\mathrm{QED}}^2 \cdot s}{32[(s - M_Z^2)^2 + \Gamma_Z^2 M_Z^2]}\frac{\sqrt{\lambda(r_{\chi_i}, r_{\chi_j})}}{x_W^2(1 - x_W)^2}\times$$

$$\times\{[g_L^2(1-\lambda_1)(1+\lambda_2)+g_R^2(1+\lambda_1)(1-\lambda_2)][(G_L^2+G_R^2)[(1+r_{\chi_i}-r_{\chi_j})(1-r_{\chi_i}+r_{\chi_j})+\lambda(r_{\chi_i},r_{\chi_j})\cos^2\theta]+$$
$$+8G_LG_R\sqrt{r_{\chi_i}r_{\chi_j}}]+2[g_L^2(1-\lambda_1)(1+\lambda_2)-g_R^2(1+\lambda_1)(1-\lambda_2)](G_L^2-G_R^2)\sqrt{\lambda(r_{\chi_i},r_{\chi_j})}\cos\theta\}. \quad (14)$$

Fig.3. Directions of impulses and spins $\ell^-\ell^+$-pair.

As follows from this expression, during annihilation the lepton and antilepton should have opposite helicities ($\lambda_1=-\lambda_2=\pm1$). If the lepton is polarized to the left ($\lambda_1=-1$; ℓ_L^-), then the antilepton must have a right-handed helicity ($\lambda_2=+1$; ℓ_R^+) and vice versa, in the annihilation of an right-polarized lepton ($\lambda_1=+1$; ℓ_R^-), the antilepton must have a left-handed helicity ($\lambda_2=-1$; ℓ_L^+) (see Fig. 3, where the momenta and spin vectors of the lepton-antilepton pair are shown).

This is due to the preservation of the full moment in the transition $\ell^-+\ell^+\to Z$. Indeed, let us consider this transition in the center-of-mass system of a lepton-antilepton pair. In this system, the momenta of the lepton and antilepton are equal in magnitude, but opposite in direction. In fig. 3a), the helicity of the lepton is equal -1, and the helicity of the antilepton is $+1$. Thus, the projection of the total angular momentum of the lepton-antilepton pair onto the direction of the lepton momentum -1. The spin of the Z-boson is equal to 1, which means that the total moment is conserved in the transition $\ell^-+\ell^+\to Z$.

Based on the differential effective cross section (14), we determine the longitudinal spin asymmetry due to the polarization of the lepton (antilepton):

$$A_1(\theta)=\frac{1}{\lambda_1}\frac{d\sigma(\lambda_1,0)/d\Omega-d\sigma(-\lambda_1,0)/d\Omega}{d\sigma(\lambda_1,0)/d\Omega+d\sigma(-\lambda_1,0)/d\Omega}, \quad (15)$$

$$A_2(\theta)=\frac{1}{\lambda_2}\frac{d\sigma(0,\lambda_2)/d\Omega-d\sigma(0,-\lambda_2)/d\Omega}{d\sigma(0,\lambda_2)/d\Omega+d\sigma(0,-\lambda_2)/d\Omega}, \quad (16)$$

where $\frac{d\sigma(\lambda_1,0)}{d\Omega}\left(\frac{d\sigma(0,\lambda_2)}{d\Omega}\right)$ – the differential cross section of process (1) in the annihilation of a longitudinally polarized lepton and an unpolarized antilepton (an unpolarized lepton and a longitudinally polarized antilepton)

Taking into account (14) in (15) and (16). We have

$$A_2(\theta)=-A_1(\theta)=\{(g_L^2-g_R^2)[(G_L^2+G_R^2)[(1+r_{\chi_i}-r_{\chi_j})(1-r_{\chi_i}+r_{\chi_j})+\lambda(r_{\chi_i},r_{\chi_j})\cos^2\theta]+$$
$$+8G_LG_R\sqrt{r_{\chi_i}r_{\chi_j}}]+2(g_L^2+g_R^2)(G_L^2-G_R^2)\sqrt{\lambda(r_{\chi_i},r_{\chi_j})}\cos\theta\}\times$$
$$\times\{(g_L^2+g_R^2)[(G_L^2+G_R^2)[(1+r_{\chi_i}-r_{\chi_j})(1-r_{\chi_i}+r_{\chi_j})+\lambda(r_{\chi_i},r_{\chi_j})\cos^2\theta]+$$
$$+8G_LG_R\sqrt{r_{\chi_i}r_{\chi_j}}]+2(g_L^2-g_R^2)(G_L^2-G_R^2)\sqrt{\lambda(r_{\chi_i},r_{\chi_j})}\cos\theta\}^{-1}. \quad (17)$$

Hence it follows that the longitudinal spin asymmetry $A_2(\theta)$ arising in the process of annihilation of polarized antileptons with unpolarized leptons is equal in magnitude and opposite in sign to the longitudinal spin asymmetry $A_1(\theta)$ arising in the interaction of longitudinally polarized leptons with unpolarized antileptons.

The differential cross section for the reaction $\ell^-+\ell^+\to Z^*\to\tilde{\chi}_i^-+\tilde{\chi}_j^+$ in the case of unpolarized particles has the form

$$\frac{d\sigma_0(\theta)}{d\Omega}=\frac{\alpha_{\text{QED}}^2\cdot s}{32[(s-M_Z^2)^2+\Gamma_Z^2M_Z^2]}\frac{\sqrt{\lambda(r_{\chi_i},r_{\chi_j})}}{x_W^2(1-x_W)^2}\times$$
$$\times\{(g_L^2+g_R^2)[(G_L^2+G_R^2)[(1+r_{\chi_i}-r_{\chi_j})(1-r_{\chi_i}+r_{\chi_j})+\lambda(r_{\chi_i},r_{\chi_j})\cos^2\theta]+$$
$$+8G_LG_R\sqrt{r_{\chi_i}r_{\chi_j}}]+2(g_L^2+g_R^2)(G_L^2-G_R^2)\sqrt{\lambda(r_{\chi_i},r_{\chi_j})}\cos\theta\}. \quad (18)$$

Differential cross section (18) of the process under consideration does not have symmetry upon replacement $\theta\to\pi-\theta$. Consequently, the angular distribution of the charginos is asymmetric. Expression for the angular asymmetry of the forward-backward chargino obtained on the basis of (18) according to the definition

$$A_{FB}(\theta)=\frac{d\sigma_0(\theta)/d(\cos\theta)-d\sigma_0(\pi-\theta)/d(\cos\theta)}{d\sigma_0(\theta)/d(\cos\theta)+d\sigma_0(\pi-\theta)/d(\cos\theta)}, \tag{19}$$

has the following

$$A_{FB}(\theta)=\frac{g_L^2-g_R^2}{g_L^2+g_R^2}\frac{2(G_L^2-G_R^2)\sqrt{\lambda(r_{\chi_i},r_{\chi_j})}\cos\theta}{(G_L^2+G_R^2)[(1+r_{\chi_i}-r_{\chi_j})(1-r_{\chi_i}+r_{\chi_j})+\lambda(r_{\chi_i},r_{\chi_j})\cos^2\theta]+8G_LG_R\sqrt{r_{\chi_i}r_{\chi_j}}} \tag{20}$$

The measurement of the longitudinal spin asymmetries $A_1(\theta)$, $A_2(\theta)$ and the angular asymmetry forward-backward $A_{FB}(\theta)$ in the experiment allows, in principle, to obtain information about the constants of the interaction of the chargino with the vector Z-boson G_L and G_R.

Expressions for the integral characteristics of the process (1) can also be obtained from (14) and (18). For this purpose, we define as follows the total cross section for the production of a pair of charginos:

$$\sigma(\lambda_1,\lambda_2)=2\pi\int_0^\pi\frac{d\sigma(\lambda_1,\lambda_2)}{d(\cos\theta)}d(\cos\theta)=$$

$$=\frac{\pi\alpha_{\text{QED}}^2\cdot s}{8[(s-M_Z^2)^2+\Gamma_Z^2M_Z^2]}\frac{\sqrt{\lambda(r_{\chi_i},r_{\chi_j})}}{x_W^2(1-x_W)^2}[g_L^2(1-\lambda_1)(1+\lambda_2)+g_R^2(1+\lambda_1)(1-\lambda_2)]\times$$

$$\times\left\{(G_L^2+G_R^2)\left[(1+r_{\chi_i}-r_{\chi_j})(1-r_{\chi_i}+r_{\chi_j})+\frac{1}{3}\lambda(r_{\chi_i},r_{\chi_j})\right]+8G_LG_R\sqrt{r_{\chi_i}r_{\chi_j}}\right\}, \tag{21}$$

and cross-sections of the birth of chargino $\tilde{\chi}_i^-$ in the front (F) and back (B) hemispheres:

$$\sigma_F=2\pi\int_0^1\frac{d\sigma}{dx}dx,\qquad \sigma_B=2\pi\int_{-1}^0\frac{d\sigma}{dx}dx. \tag{22}$$

From the formula for the effective cross section (21) for the integral longitudinal spin asymmetry, we obtain:

$$A_2=-A_1=\frac{g_L^2-g_R^2}{g_L^2+g_R^2}. \tag{23}$$

This asymmetry is only a function of the Weinberg parameter x_W and at $x_W=0.2315$ $A_2=14.7\%$.

For the integral asymmetry forward-backward, the expression is:

$$A_{FB}=\frac{\sigma_F-\sigma_B}{\sigma_F+\sigma_B}=$$

$$=\frac{g_L^2-g_R^2}{g_L^2+g_R^2}\frac{(G_L^2-G_R^2)\sqrt{\lambda(r_{\chi_i},r_{\chi_j})}}{(G_L^2+G_R^2)\left[(1+r_{\chi_i}-r_{\chi_j})(1-r_{\chi_i}+r_{\chi_j})+\frac{1}{3}\lambda(r_{\chi_i},r_{\chi_j})\right]+8G_LG_R\sqrt{r_{\chi_i}r_{\chi_j}}}. \tag{24}$$

Let's assess the above asymmetries in the processes $e^-e^+\to\tilde{\chi}_1^-+\tilde{\chi}_1^+$, $e^-e^+\to\tilde{\chi}_2^-+\tilde{\chi}_2^+$, $e^-e^+\to\tilde{\chi}_1^-+\tilde{\chi}_2^+$ and $e^-e^+\to\tilde{\chi}_2^-+\tilde{\chi}_1^+$ at the value of the parameter $tg\beta=1$. In this case, the matrices V_{ij} and U_{ij} are defined as [10]

$$V_{ij}=\frac{1}{\sqrt{2}}\begin{pmatrix}1 & 1\\ 1 & -1\end{pmatrix},\quad U_{ij}=\frac{1}{\sqrt{2}}\begin{pmatrix}1 & 1\\ -1 & 1\end{pmatrix}. \tag{25}$$

Using the elements of these matrices for the left and right constants of the interaction of the chargino with the Z-boson, we obtain the expressions:

1) in process

$e^-e^+\to\tilde{\chi}_1^-+\tilde{\chi}_1^+$ $G_L=G_R=\frac{1}{\cos\theta_W}\left[x_W-\frac{1}{4}\right]$;

2) in process

$e^-e^+\to\tilde{\chi}_2^-+\tilde{\chi}_2^+$ $G_L=G_R=\frac{1}{\cos\theta_W}\left[x_W-\frac{1}{4}\right]$;

3) in process

$e^-e^+\to\tilde{\chi}_1^-+\tilde{\chi}_2^+$ $G_L=-G_R=-\frac{3}{4\cos\theta_W}$;

4) in process e

$e^-e^+\to\tilde{\chi}_2^-+\tilde{\chi}_1^+$ $G_L=-G_R=-\frac{1}{4\cos\theta_W}$.

As can be seen, in all four processes $G_L^2=G_R^2$, because of this condition, the asymmetry $A_{FB}(\theta)$ and integral angular asymmetry (24) become zero. As for the longitudinal spin asymmetries $A_2(\theta)$, $A_1(\theta)$, and also the integral spin asymmetries A_2 and A_1, they are the same in all processes and depend only on the Weinberg parameter x_W:

$$A_2(\theta) = -A_1(\theta) = A_2 = -A_1 \frac{\frac{1}{4} - x_W}{\frac{1}{4} - x_W + 2x_W^2}.$$

As noted above, for the Weinberg parameter $x_W = 0.2315$, these asymmetries are $\pm 14.7\%$.

4. CASE OF TRANSVERSE POLARIZATION OF BEAMS

It is known that electrons and positrons moving in storage rings acquire predominantly transverse polarization due to synchrotron radiation. In the case when the initial particles are transversely polarized, the differential cross section of process (1) has the form:

$$\frac{d\sigma(\eta_1, \eta_2)}{d\Omega} = \frac{d\sigma_0(\theta)}{d\Omega}[1 + \eta_1\eta_2 A_\perp(\theta, \varphi)], \quad (26)$$

where $\frac{d\sigma_0(\theta)}{d\Omega}$ – the differential cross section of process (1) in the case of unpolarized particles (formula (18)), $A_\perp(\theta, \varphi)$ – the transverse spin asymmetry due to the transverse polarizations of the lepton and antilepton (the angle between the vectors $\vec{\eta}_1$ and $\vec{\eta}_2$ is taken $\phi = \pi$):

$$A_\perp(\theta, \varphi) = -g_L g_R (G_L^2 + G_R^2)\lambda(r_{\chi_i}, r_{\chi_j}) \sin^2\theta \cos 2\varphi \times$$
$$\times \{(g_L^2 + g_R^2)[(G_L^2 + G_R^2)[(1 + r_{\chi_i} - r_{\chi_j})(1 - r_{\chi_i} + r_{\chi_j}) + \lambda(r_{\chi_i}, r_{\chi_j})\cos^2\theta] + 8G_L G_R \sqrt{r_{\chi_i} r_{\chi_j}}] +$$
$$+ 2(g_L^2 - g_R^2)(G_L^2 - G_R^2)\sqrt{\lambda(r_{\chi_i}, r_{\chi_j})}\cos\theta\}^{-1}. \quad (27)$$

This asymmetry is maximum at the azimuthal angle of departure of the chargino $\varphi = 0$ and π.

In fig. 4 shows the angular dependence of the transverse spin asymmetry $A_\perp(\theta)$ in the reactions $e^- + e^+ \to \tilde{\chi}_1^- + \tilde{\chi}_1^+$ (curve 1), $e^- + e^+ \to \tilde{\chi}_2^- + \tilde{\chi}_2^+$ (curve 2), $e^- + e^+ \to \tilde{\chi}_1^- + \tilde{\chi}_2^+$ (or $e^- + e^+ \to \tilde{\chi}_2^- + \tilde{\chi}_1^+$) (curve 3) at $\sqrt{s} = 500$ GeV and parameter values of $M_2 = 150$ GeV, $\mu = 200$ GeV, $x_W = 0.2315$, $M_W = 80.385$ GeV.

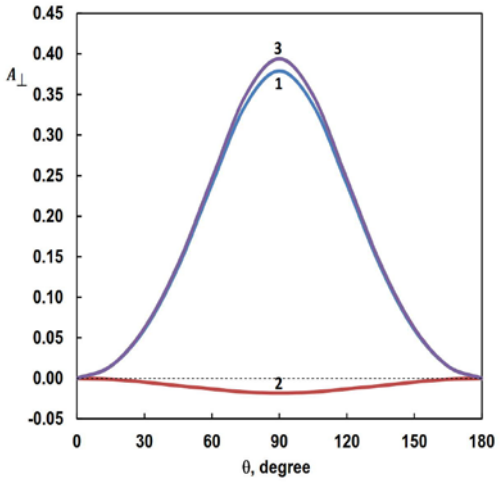

Fig. 4. Transverse spin asymmetry $A_\perp(\theta)$ as a function of angle θ.

As can be seen from the figure, in the processes $e^- + e^+ \to \tilde{\chi}_1^- + \tilde{\chi}_1^+$, $e^- + e^+ \to \tilde{\chi}_1^- + \tilde{\chi}_2^+$ (or $e^- + e^+ \to \tilde{\chi}_2^- + \tilde{\chi}_1^+$) the transverse spin asymmetry is positive and with an increase in the angle θ it reaches a maximum at $\theta = 90°$, and with a further increase in the angle, this asymmetry decreases and approaches zero at the end of the angular spectrum.

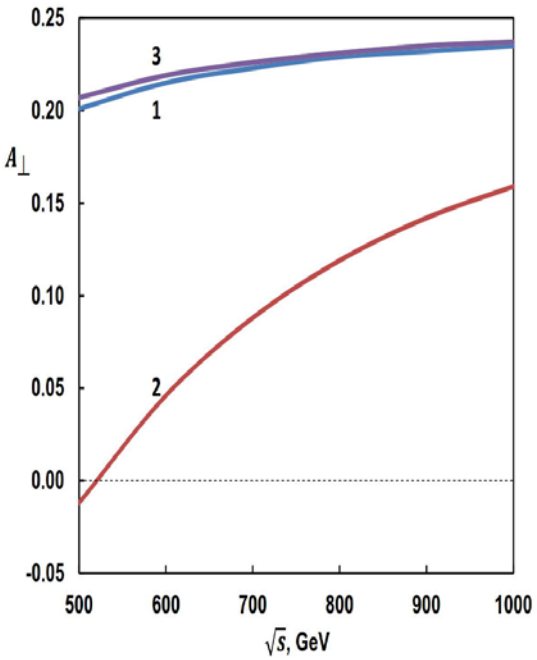

Fig. 5. Energy dependence of transverse spin asymmetry $\sqrt{s}$.

As for the transverse spin asymmetry $A_\perp(\theta)$ in the reaction $e^- + e^+ \to \tilde{\chi}_2^- + \tilde{\chi}_2^+$, we note that it is negative and at an angle of $\theta = 90°$ reaches a minimum (at this point, the asymmetry $A_\perp(\theta) = -1.8\%$).

We also present an expression for the transverse spin asymmetry $A_\perp(\sqrt{s}, \varphi)$ integrated over the polar angle θ of the chargino emission:

$$A_{\perp}(\sqrt{s},\varphi) = -\frac{2}{3} g_L g_R (G_L^2 + G_R^2)\lambda(r_{\chi_i}, r_{\chi_j})\cos 2\varphi \times$$

$$\times \left\{ (g_L^2 + g_R^2)[(G_L^2 + G_R^2)\left[(1 + r_{\chi_i} - r_{\chi_j})(1 - r_{\chi_i} + r_{\chi_j}) + \frac{1}{3}\lambda(r_{\chi_i}, r_{\chi_j}) \right] + 8 G_L G_R \sqrt{r_{\chi_i} r_{\chi_j}} \right\}^{-1}. \quad (28)$$

In fig. 5 shows the energy dependence of the transverse spin asymmetry $A_{\perp}(\sqrt{s})$ integrated over the polar angle θ in the reactions $e^- + e^+ \to \tilde{\chi}_1^- + \tilde{\chi}_1^+$ (curve 1), $e^- + e^+ \to \tilde{\chi}_2^- + \tilde{\chi}_2^+$ (curve 2) and $e^- + e^+ \to \tilde{\chi}_1^- + \tilde{\chi}_2^+$ (or $e^- + e^+ \to \tilde{\chi}_2^- + \tilde{\chi}_1^+$) (curve 3) at the same values of the parameters as in Figure 3. In all processes, the transverse spin asymmetry is positive and with increasing energy of colliding electron-positron beams, the asymmetry is increasing.

5. DEGREES OF LONGITUDINAL AND TRANSVERSE POLARIZATION OF CHARGINO

So far, we have been interested in the polarization states of the lepton and antilepton. We have determined the longitudinal and transverse spin asymmetries caused by the polarizations of the lepton and antilepton. Note that the study of the degrees of longitudinal and transverse polarizations of the charginos is also of certain interest. They can provide valuable information about the constants of interaction of a chargino with a gauge Z-boson G_L and G_R. In this regard, we turn to the study of the polarization characteristics of the chargino.

Let us consider the differential cross section of process (1) taking into account the longitudinal polarization of the chargino:

$$\frac{d\sigma(h)}{d\Omega} = \frac{1}{2}\frac{d\sigma_0}{d\Omega}[1 + hP_{\parallel}(\theta)]. \quad (29)$$

Here, $\frac{d\sigma_0}{d\Omega}$ – the differential effective cross section for reaction (1) in the case of unpolarized particles, a $P_{\parallel}(\theta)$ – the degree of longitudinal polarization of the chargino $\tilde{\chi}_i^-$:

$$P_{\parallel}(\theta) = \{(g_L^2 + g_R^2)(G_L^2 - G_R^2)\sqrt{\lambda(r_{\chi_i}, r_{\chi_j})}[1 - r_{\chi_i} + r_{\chi_j} + (1 + r_{\chi_i} - r_{\chi_j})\cos^2\theta] -$$
$$- 2(g_L^2 - g_R^2)[(G_L^2 + G_R^2)(1 - r_{\chi_i} - r_{\chi_j}) + 4 G_L G_R \sqrt{r_{\chi_i} r_{\chi_j}}]\} \times$$
$$\times \{(g_L^2 + g_R^2)[(G_L^2 + G_R^2)[(1 + r_{\chi_i} - r_{\chi_j})(1 - r_{\chi_i} + r_{\chi_j}) + \lambda(r_{\chi_i}, r_{\chi_j})\cos^2\theta] + 8 G_L G_R \sqrt{r_{\chi_i} r_{\chi_j}}] +$$
$$+ 2(g_L^2 - g_R^2)(G_L^2 - G_R^2)\sqrt{\lambda(r_{\chi_i}, r_{\chi_j})}\cos\theta\}^{-1}. \quad (30)$$

If the chargino is transversely polarized in the plane of production, then the differential cross section of process (1) takes the form (the lepton is longitudinally polarized):

$$\frac{d\sigma(\lambda_1, \eta)}{d\Omega} = \frac{1}{2}\frac{d\sigma(\lambda_1)}{d\Omega}[1 + \eta P_{\perp|}(\theta, \sqrt{s})], \quad (31)$$

Where $\frac{d\sigma(\lambda_1)}{d\Omega}$ – the differential effective cross section for reaction (1) upon annihilation of a longitudinally polarized lepton and an unpolarized antilepton:

$$\frac{d\sigma(\lambda_1)}{d\Omega} = \frac{\alpha_{\text{QED}}^2 \cdot s}{32[(s - M_Z^2)^2 + \Gamma_Z^2 M_Z^2]} \frac{\sqrt{\lambda(r_{\chi_i}, r_{\chi_j})}}{x_W^2 (1 - x_W)^2} \times$$
$$\times \{[g_L^2(1 - \lambda_1) + g_R^2(1 + \lambda_1)][(G_L^2 + G_R^2)[(1 + r_{\chi_i} - r_{\chi_j})(1 - r_{\chi_i} + r_{\chi_j}) + \lambda(r_{\chi_i}, r_{\chi_j})\cos^2\theta] +$$
$$+ 8 G_L G_R \sqrt{r_{\chi_i} r_{\chi_j}}] + 2[g_L^2(1 - \lambda_1) - g_R^2(1 + \lambda_1)](G_L^2 - G_R^2)\sqrt{\lambda(r_{\chi_i}, r_{\chi_j})}\cos\theta\}, \quad (32)$$

η – the transverse component of the spin vector of the chargino, and $P_{\perp}(\theta, \sqrt{s})$ – the degree of transverse polarization of the chargino, determined by the expression:

$$P_{\perp}(\theta, \sqrt{s}) = \sqrt{\lambda(r_{\chi_i}, r_{\chi_j})}\sin 2\theta\{[g_L^2(1 - \lambda_1) + g_R^2(1 + \lambda_1)](G_L^2 - G_R^2)\sqrt{r_{\chi_i}} +$$
$$+ [g_L^2(1 - \lambda_1) - g_R^2(1 + \lambda_1)][-(G_L^2 + G_R^2)\sqrt{r_{\chi_i}} + 8 G_L G_R \sqrt{r_{\chi_j}}]\} \cdot \{[g_L^2(1 - \lambda_1) + g_R^2(1 + \lambda_1)] \times$$
$$\times [(G_L^2 + G_R^2)[(1 + r_{\chi_i} - r_{\chi_j})(1 - r_{\chi_i} + r_{\chi_j}) + \lambda(r_{\chi_i}, r_{\chi_j})\cos^2\theta] + 8 G_L G_R \sqrt{r_{\chi_i} r_{\chi_j}}] +$$

$$+2[g_L^2(1-\lambda_1)-g_R^2(1+\lambda_1)](G_L^2-G_R^2)\sqrt{\lambda(r_{\chi_i}, r_{\chi_j})}\cos\theta\}^{-1}. \qquad (33)$$

In fig. 6 illustrates the angular dependence of the degree of longitudinal polarization of the chargino in the processes $e^-+e^+\to\tilde{\chi}_1^-+\tilde{\chi}_1^+$ (curve 1), $e^-+e^+\to\tilde{\chi}_2^-+\tilde{\chi}_2^+$ (curve 2) and $e^-+e^+\to\tilde{\chi}_1^-+\tilde{\chi}_2^+$ (or $e^-+e^+\to\tilde{\chi}_2^-+\tilde{\chi}_1^+$) (curve 3). It is seen that in all processes the degree of longitudinal polarization of the chargino is negative, with an increase in the emission angle θ it slowly decreases, reaches a minimum at an angle of $\theta=90°$, and a further increase in the angle leads to an increase in the degree of longitudinal polarization of the chargino.

The angular dependence of the degree of transverse polarization $P_\perp(\theta,\sqrt{s})$ of the chargino in the reaction $e^-+e^+\to\tilde{\chi}_1^-+\tilde{\chi}_1^+$ is shown in fig. 7 for the helicity of the lepton $\lambda_1=1$ (curve 1), $\lambda_1=-1$ (curve 2) and for an unpolarized electron (curve 3). It follows from the figure that in the interaction of a left (right) polarized electron with an unpolarized positron, the degree of transverse polarization of the chargino in the reaction $e^-+e^+\to\tilde{\chi}_1^-+\tilde{\chi}_1^+$ first increases (decreases) and reaches a maximum (minimum) at 60°, and then decreases (increases) becomes zero, and changes sign repeats numerical values with opposite sign. In the annihilation of an unpolarized electron-positron pair, the degree of transverse polarization of the chargino is only a few percent (at $\theta=45°$ $P_\perp=4.8\%$).

The total cross section for reaction (1), obtained by integrating over the angles θ and φ, has the form:

$$\sigma_0(\lambda_1)=\frac{\alpha_{\text{КЭД}}^2\cdot s}{8[(s-M_Z^2)^2+\Gamma_Z^2M_Z^2]}\frac{\sqrt{\lambda(r_{\chi_i}, r_{\chi_j})}}{x_W^2(1-x_W)^2}[g_L^2(1-\lambda_1)+g_R^2(1+\lambda_1)]\times$$
$$\times\left\{(G_L^2+G_R^2)^2\left[(1+r_{\chi_i}-r_{\chi_j})(1-r_{\chi_i}+r_{\chi_j})+\frac{1}{3}\lambda(r_{\chi_i}, r_{\chi_j})\right]+8G_LG_R\sqrt{r_{\chi_i}r_{\chi_j}}\right\}. \qquad (34)$$

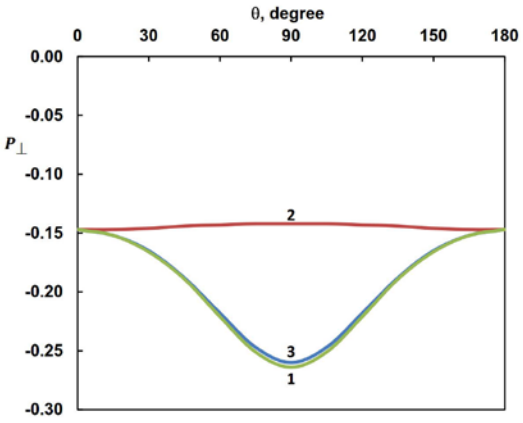

Fig.6. Angular dependence of the degree of longitudinal polarization of the chargino in the processes $e^-e^+\to\tilde{\chi}_1^-\tilde{\chi}_1^+$ (curve 1), $e^-e^+\to\tilde{\chi}_2^-\tilde{\chi}_2^+$ (curve 2) and $e^-e^+\to\tilde{\chi}_1^-\tilde{\chi}_2^+$ (or $e^-e^+\to\tilde{\chi}_2^-\tilde{\chi}_1^+$) (curve 3).

In fig. 8 illustrates the energy dependence of the cross section in the reaction $e^-+e^+\to\tilde{\chi}_1^-+\tilde{\chi}_2^+$ in three cases: a) when the electron is right-handed ($\lambda_1=1$, $e_R^-+e^+\to\tilde{\chi}_1^-+\tilde{\chi}_2^+$); b) when the electron has left helicity ($\lambda_1=-1$, $e_L^-+e^+\to\tilde{\chi}_1^-+\tilde{\chi}_2^+$); c) when particles are unpolarized ($e^-+e^+\to\tilde{\chi}_1^-+\tilde{\chi}_2^+$).

As can be seen from the figure, there is the following relationship between these sections:

$$\sigma_1(e_R^-e^+\to\tilde{\chi}_1^-\tilde{\chi}_2^+)<\sigma_3(e^-e^+\to\tilde{\chi}_1^-\tilde{\chi}_2^+)<\sigma_2(e_L^-e^+\to\tilde{\chi}_1^-\tilde{\chi}_2^+)$$

This is due to the fact that the left-hand coupling constant of the electron with the Z-boson g_L^2 is numerically ahead of the right-hand coupling constant g_R^2 ($g_L^2>g_R^2$).

The study of the contribution of s-channel diagrams with the exchange of Higgs bosons H, h and A, as well as the t-channel diagram with exchange of sneutrino $\tilde{\nu}_{eL}$, was outlined in another work.

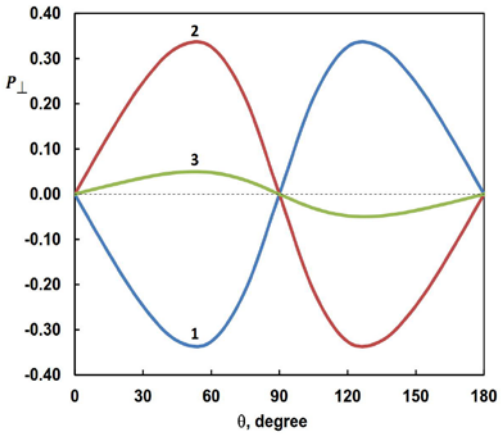

Fig. 7. Angular dependence of the degree of transverse polarization of the chargino in the process $e^-e^+\to\tilde{\chi}_1^-\tilde{\chi}_1^+$: $\lambda_1=1$ (curve 1), $\lambda_1=-1$ (curve 2) and for an unpolarized electron (curve 3).

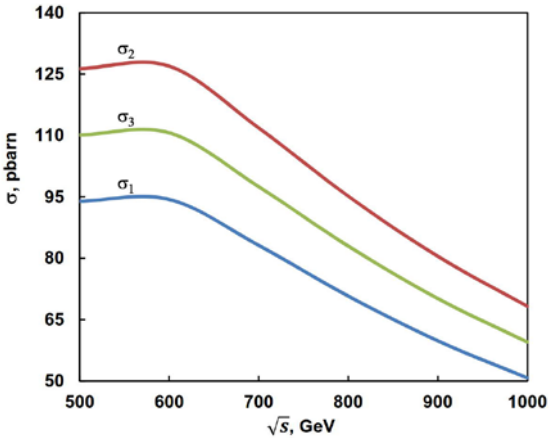

Fig. 8. The energy dependence of the cross section of the reaction $e^-e^+ \to \tilde{\chi}_1^-\tilde{\chi}_2^+$ in the cases $\lambda_1 = 1$ (curve 1), $\lambda_1 = -1$ (curve 2) and when unpolarized electron (curve 3).

CONCLUSION

We have discussed the annihilation process of an arbitrarily polarized lepton-antilepton pair (e^-e^+ - or $\mu^-\mu^+$-pair) into a chargino pair $\ell^- + \ell^+ \to \tilde{\chi}_i^- + \tilde{\chi}_j^+$. The diagram with the exchange of a neutral Z-boson is studied in detail in the case of a longitudinally and transversely polarized lepton-antilepton pair. The longitudinal and transverse spin asymmetries caused by the polarizations of the lepton-antilepton pair, the forward-backward angular asymmetry A_{FB}, as well as the degrees of the longitudinal and transverse polarization of the chargino are determined. The angular and energy dependences of these characteristics, as well as the total cross section of the reaction under consideration, are studied in detail. Research results are illustrated with graphs.

APPENDIX

Here we give the expressions for the squared amplitudes $\left|M^{(\gamma)}\right|^2$, $\left|M^{(Z)}\right|^2$ and $(M^{+(\gamma)}M^{(Z)} + M^{+(Z)}M^{(\gamma)})$:

$$\left|M^{(\gamma)}\right|^2 = \frac{8(4\pi\alpha_{\text{QED}})^2}{s^2} \times$$
$$\times\{(k_1\cdot p_1)(k_2\cdot p_2)+(k_1\cdot p_2)(k_2\cdot p_1)-m_e^2[(k_1\cdot s_1)(k_2\cdot s_2)+(k_1\cdot s_2)(k_2\cdot s_1)]-$$
$$-(s_1\cdot s_2)[(k_1\cdot p_1)(k_2\cdot p_2)+(k_1\cdot p_2)(k_2\cdot p_1)-(p_1\cdot p_2)[(k_1\cdot s_1)(k_2\cdot s_2)+(k_1\cdot s_2)(k_2\cdot s_1)-$$
$$-(k_1\cdot k_2)(s_1\cdot s_2)]+(p_1\cdot s_2)[(k_1\cdot s_1)(p_2\cdot k_2)+(k_2\cdot s_1)(k_1\cdot p_2)-(k_1\cdot k_2)(p_2\cdot s_1)]+$$
$$+(p_2\cdot s_1)[(k_1\cdot p_1)(k_2\cdot s_2)+(k_2\cdot p_1)(k_1\cdot s_2)]+m_{\chi_i}m_{\chi_j}[(p_1\cdot p_2)-m_e^2(s_1\cdot s_2)]\};$$

$$\left|M^{(Z)}\right|^2 = \left(\frac{\pi\alpha_{\text{QED}}}{x_W(1-x_W)}\right)^2 \frac{8}{(s-M_Z^2)^2+\Gamma_Z^2M_Z^2}\times$$
$$\times\{[(g^L_{\chi_i^-\chi_j^-Z})^2+(g^R_{\chi_i^-\chi_j^-Z})^2][(g_L^2+g_R^2)[(k_1\cdot p_1)(k_2\cdot p_2)+(k_1\cdot p_2)(k_2\cdot p_1)-m_e^2[(k_1\cdot s_1)(k_2\cdot s_2)+$$
$$+(k_1\cdot s_2)(k_2\cdot s_1)]]+(g_L^2-g_R^2)m_e[(k_1\cdot p_1)(k_2\cdot s_2)+(k_2\cdot p_1)(k_1\cdot s_2)-(k_1\cdot p_2)(k_2\cdot s_1)-$$
$$-(p_1,k_2)(k_1\cdot s_1)]+2g_Lg_R[-(s_1\cdot s_2)[(k_1\cdot p_1)(k_2\cdot p_2)+(k_1\cdot p_2)(k_2\cdot p_1)]-$$
$$-(p_1\cdot p_2)[(k_1\cdot s_1)(k_2\cdot s_2)+(k_1\cdot s_2)(k_2\cdot s_1)-(p_1\cdot p_2)(k_1\cdot k_2)]+(p_1\cdot s_2)[(k_1\cdot s_1)(k_2\cdot p_2)+$$
$$+(k_2\cdot s_1)(k_1\cdot p_2)-(k_1\cdot k_2)(p_1\cdot s_2)]+(p_2\cdot s_1)[(k_1\cdot p_1)(k_2\cdot s_2)+(k_1\cdot s_2)(k_2\cdot p_1)]]]+$$
$$+[(g^L_{\chi_i^-\chi_j^-Z})^2-(g^R_{\chi_i^-\chi_j^-Z})^2][(g_L^2+g_R^2)m_e[(p_1\cdot k_2)(k_1\cdot s_2)-(p_1\cdot k_1)(k_2\cdot s_2)+(k_1\cdot s_1)(k_2\cdot p_2)-$$
$$-(k_1\cdot p_2)(k_2\cdot s_1)]+(g_L^2-g_R^2)[(k_1\cdot p_2)(k_2\cdot p_1)-(k_1\cdot p_1)(k_2\cdot p_2)+m_e^2[(k_1\cdot s_1)(k_2\cdot s_2)-$$
$$-(k_1\cdot s_2)(k_2\cdot s_1)]]+g_Rg_Lm_e[(k_2\cdot p_2)(k_1\cdot s_2)-(k_1\cdot p_2)(k_2\cdot s_2)+(k_1\cdot p_1)(k_2\cdot s_1)-(k_2\cdot p_1)(k_1\cdot s_1)]]]+$$
$$+2g^L_{\chi_i^-\chi_j^-Z}g^R_{\chi_i^-\chi_j^-Z}m_{\chi_i}m_{\chi_j}[(g_L^2+g_R^2)[(p_1\cdot p_2)-m_e^2(s_1\cdot s_2)]+(g_L^2-g_R^2)m_e[(p_1\cdot s_2)-(p_2\cdot s_1)]]\};$$

$$M^{+(\gamma)}M^{(Z)}+M^{+(Z)}M^{(\gamma)} = \left(\frac{4\pi\alpha_{\text{QED}}}{x_W(1-x_W)}\right)^2 \frac{2(s-M_Z^2)}{s[(s-M_Z^2)^2+\Gamma_Z^2M_Z^2]}\times$$
$$\times\{(g^L_{\chi_i^-\chi_j^+Z}+g^R_{\chi_i^-\chi_j^+Z})[(g_L+g_R)[(p_1\cdot k_1)(p_2\cdot k_2)+(p_1\cdot k_2)(p_2\cdot k_1)-m_e^2[(k_1\cdot s_1)(k_2\cdot s_2)+$$

$$+(k_1\cdot s_2)(k_2\cdot s_1)]-(s_1\cdot s_2)[(k_1\cdot p_1)(k_2\cdot p_2)+(k_1\cdot p_2)(k_2\cdot p_1)]-(p_1\cdot p_2)[(k_1\cdot s_1)(k_2\cdot p_2)+$$
$$+(k_1\cdot s_2)(k_2\cdot s_1)-(k_1\cdot k_2)(s_1\cdot s_2)]+(p_1\cdot s_2)[(k_1\cdot s_1)(k_2\cdot p_2)+(k_2\cdot s_1)(k_1\cdot p_2)-(k_1\cdot k_2)(p_2\cdot s_1)]+$$
$$+(p_2\cdot s_1)[(k_1\cdot s_2)(k_2\cdot p_1)+(k_2\cdot s_2)(k_1\cdot p_1)]]+(g_L-g_R)m_e[(k_1\cdot s_2)(k_2\cdot p_1)+(k_1\cdot p_1)(k_2\cdot s_1)-$$
$$-(k_1\cdot p_2)(k_2\cdot s_1)-(k_2\cdot p_2)(k_1\cdot s_1)+m_{\chi_i}m_{\chi_j}[(p_1\cdot s_2)-(p_2\cdot s_1)]]]+(g^L_{\chi_i^-\chi_j^+Z}-g^R_{\chi_i^-\chi_j^-Z})m_e[(g_L+g_R)\times$$

$$\times[(k_1\cdot p_1)(k_2\cdot s_2)-(k_2\cdot p_1)(k_1\cdot s_2)+(k_1\cdot p_2)(k_2\cdot s_2)-(k_2\cdot p_2)(k_1\cdot s_1)+(k_1\cdot p_2)(k_2\cdot s_2)-$$
$$-(k_2\cdot p_2)(k_1\cdot s_2)+(k_1\cdot p_1)(k_2\cdot s_1)-(k_2\cdot p_1)(k_1\cdot s_1)]-(g_L-g_R)[(k_1\cdot p_1)(k_2\cdot p_2)-$$
$$-(k_1\cdot p_2)(k_2\cdot p_1)-m_e^2[(k_1\cdot s_1)(k_2\cdot s_2)-(k_1\cdot s_2)(k_2\cdot s_1)]]]\}.$$

---

[1] ATLAS Collaboration. Observation of a new particle in the search for the Standard Model Higgs boson with the ATLAS detector of the LHC. Phys. Letters, 2012, B 716, p. 1-29.

[2] CMS Collaboration. Observation of a new boson at mass of 125 GeV with the CMS experiment at the LHC. Phys. Letters, 2012, B 716, p. 30-60.

[3] *V.A. Rubakov*. On Large Hadron Colliders discovery of a new particle with Higgs Boson properties. UFN, 2012, V.182, No 10, p.1017-1025 (in Russian).

[4] *A.V. Lanev*. CMS Collaboration results: Higgs boson and search for new physics. UFN, 2014, V. 184, No 9, p. 996-1004 (In Russian).

[5] *D.I. Kazakov*. The Higgs boson is found: what is next? UFN, 2014, V. 184, No 9, p. 1004-1017 (In Russian).

[6] *P.W. Higgs.* Broken Symmetries and the Masses of gauge Bosons. Phys. Rev. Letters, 1964, V.13, No 16, p. 508.

[7] *F. Englert, R. Brou*t. Broken Symmetry and the mass of gauge vector Mesons Phys. Rev. Letters, 1964, V.13, No 9, p.321.

[8] *A. Djouadi*. The Anatomy of Electro-Weak Symmetry Breaking. Tome II: The Higgs boson in the Minimal Supersymmetric Standard Model. arXiv: hep-ph/0503172v2, 2003; DOI: 10.1016/j.physrep.2007.10.004.

[9] *M. Spira*. QCD effects in Higgs Physics. arXiv: hep-ph / 9705337v2, 1997.

[10] *J.F. Gunion, H.E.Haber*. Higgs bosons in Supersymmetric Phys. Rev. 2003. V. D 67. P. 0750.19.

[11] *H.E. Haber, G. Kane.* The search for supersymmetry: Probing physics beyond the Standard Model // Phys. Rep., 1985, V. C117. No 2-4, P. 75-263.

[12] *E.Sh. Omarova, V. Guseynov.* Gaugino pair production at LHC / Materials of the IX Republican scientific conference "Actual problems of physics", Baku, 2016, P. 21-24.

[13] *E.Ch. Christova, N.P. Nedelcheva.* Neutralino production in polarized e^-e^+-collisions. Preprint, Dubna, 1988, E2-88-607, 14p.

[14] *S.M. Bilenky, N.P. Nedelcheva.* Possible test for supersymmetry in e^-e^+-collisions with polarized beams. Preprint, Dubna, 1986, E2-88-494, 10p.

[15] *S.M. Bilenky, E.Ch. Christova, N.P. Nedelcheva.* Possible test for Majorana nature of heavy neutral fermions produced in polarized e^-e^+-collisions. Preprint, Dubna, 1986, E2-86-353, 15p.

[16] *A. Djouadi, J. Kalinowski, P. Ohmann, P.M. Zerwas.* Heavy SUSY Higgs bosons at e^-e^+ linear colliders. Z. Phys., 1997, V. C74, P. 93-111.

[17] *P. Cheapetta, J. Soffer, P. Taxil, F.M. Renard, P. Sorba.* Supersymmetry and polarization in e^-e^+-collisions (I) Nucl. Phys. 1984, V. B259, p. 365-396.

[18] *E.Ch. Christova, N.P. Nedelcheva.* On the ligh test supersymmetric particle in polarized e^-e^+-collisions. Preprint, Dubna, 1987, E2-87-836, 8p.

Received:19.10.2020

ON THE EXACT SOLUTION OF THE CONFINED POSITION-DEPENDENT MASS HARMONIC OSCILLATOR MODEL UNDER THE KINETIC ENERGY OPERATOR COMPATIBLE WITH GALILEAN INVARIANCE

E.I. JAFAROV and A.M. MAMMADOVA
Institute of Physics, Azerbaijan National Academy of Sciences
Javid av. 131, AZ1143, Baku, Azerbaijan
E-mail: ejafarov@physics.science.az

We propose exactly-solvable model of the confined harmonic oscillator in the framework of the effective mass formalism varying with position. Analytical expression of the position-dependent effective mass is chosen by such a way that it provides confinement effect for the via the infinitely high borders at value of position $x = \pm a$. Wave functions of the stationary states of the oscillator model under study have been obtained by solving exactly corresponding Schrödinger equation, which free Hamiltonian is compatible with Galilean invariance. Analytical expression of the wave function is described by the Gegenbauer polynomials, whereas obtained energy spectrum is discrete, but non-equidistant. It is shown that both energy spectrum and wave function completely recover known expressions of the so-called Hermite oscillator equidistant energy spectrum and wave function of the stationary states under the limit $a \to \infty$.

Keywords: Position-dependent effective mass, quantum harmonic oscillator, Gegenbauer polynomials, non-equidistant energy spectrum.
PACS: 03.65.-w, 02.30.Hq, 03.65.Ge

1. INTRODUCTION

Quantum harmonic oscillator is one of the most attractive problems of the theoretical physics and pure mathematics [1,2]. Its attractiveness for theoretical physics is existence of the exact solutions in terms of the wave functions and energy spectrum of the quantum system under consideration in the framework of the various initial bounded conditions. Attractiveness of same quantum systems for pure mathematics is related with analytical expression of the wave functions, which are expressed through certain orthogonal polynomials of the Askey scheme. One needs to note that different orthogonal polynomials appear in the analytical expressions of the wave functions as a result of the initial conditions imposed to the quantum oscillator model. These initial conditions can be related with specific non-relativistic or relativistic behaviour of the oscillator model, but also the finite or infinite nature of the position that determines how the wave function is going to be bounded.

Non-relativistic quantum harmonic oscillator model with the wave functions bounded at infinity is well known [3]. Its energy spectrum is discrete and equidistant. Analytical expression of the wave function of this oscillator model with effective mass m_0 and angular frequency ω_0 is obtained through exact solution of the corresponding Schrödinger equation in terms of the Hermite polynomials. It is easy to observe that the wave function expressed via Hermite polynomials vanishs at $\pm\infty$. However, there is no any unique approach for the definition of the harmonic oscillator model with the wave function vanishing at finite region. One of the approaches is to look for approximate solutions of the Schrödinger equation describing non-relativistic quantum harmonic oscillator with the wave function bounded at finite region. Some examples of such approximate solutions having wide range applications from astrophysics to the nanotechnologies already exist [4-10]. Another approach, leading to exact solutions of similar oscillator model confined within the finite region is related with the replacement of the constant effective mass with the position-dependent effective mass formalism. Such a formalism was proposed within the theory explaining seminal experiment on the tunneling effect from superconductors within the free multi-particle approach with bandwidth changing with position [11]. Furthermore, the approach of the position-dependent effective mass has been successfully applied for explanation of the many experimental results and phenomena. Main goal of our paper is to develop this approach and apply it for exact solution of the non-relativistic quantum harmonic oscillator model with position-dependent effective mass with Galilean invariance.

The paper is structured as follows: Section 2 contains brief review of the well-known nonrelativistic quantum harmonic oscillator model, which wave functions of the stationary states are expressed through the Hermite polynomials. Then, we present main results devoted to the constructed model of the confined quantum harmonic oscillator possessing the position-dependent effective mass with Galilean invariance in Section 3. Final section is devoted to discussion of the obtained results. This section also includes basic limit relations between the model under construction and the so-called Hermite oscillator model.

2. NON-RELATIVISTIC HARMONIC OSCILLATOR IN TERMS OF THE HERMITE POLYNOMIALS

In this section, we are going to present general information about the problem of the non-relativistic quantum harmonic oscillator and its exact solution in

131, H.Javid ave, AZ-1143, Baku
ANAS, Institute of Physics
E-mail: jophphysics@gmail.com

terms of the wave functions of the stationary states and discrete energy spectrum. The information being provided in this section is well known and can be easily found in most of the textbooks devoted to quantum mechanics and its basic principles. However, we think that the information provided below can be useful for reader easily to understand the problem under consideration and its correct limits to the known harmonic oscillator results. First of all, one can start from the correct definition of the Schrödinger equation that in the position representation has the following form:

$$\left[\frac{\hat{P}_x^2}{2m}+V(x)\right]\psi(x)=E\psi(x). \quad (2.1)$$

Then, introducing exact expression of the quantum harmonic oscillator potential as

$$V(x)=\frac{m_0{\omega_0}^2x^2}{2}, \quad (2.2)$$

we can solve eq.(2.1) exactly assuming that eigenfunctions $\psi(x)$ of it vanish at infinity. Here m and ω_0 are position-independent mass and angular frequency of the non-relativistic quantum harmonic oscillator. We are going to perform all computation within the canonical approach to the quantum mechnics. Therefore, one-dimensional momentum operator is defined as below:

$$\hat{p}_x=-i\hbar\frac{d}{dx}. \quad (2.3)$$

Sustitution of both eqs.(2.2)&(2.3) at eq.(2.1) leads to the following second order differential equation:

$$\frac{d^2\psi}{dx^2}+\frac{2m_0}{\hbar^2}\left(E-\frac{m_0{\omega_0}^2x^2}{2}\right)\psi=0. \quad (2.4)$$

Its exact solution in terms of the eigenvalues and eigenfunctions is well known. Energy spectrum E being as eigenvalue of eq.(2.4) is discrete and equidistant as follows:

$$E\equiv E_n=\hbar\omega_0\left(n+\frac{1}{2}\right), n=0,1,\cdots. \quad (2.5)$$

Wave functions of the stationary states being as eigenfunctions eq.(2.4) have the following analytical expression:

$$\psi_n(x)=\frac{1}{\sqrt{2^n n!}}\left(\frac{m\omega_0}{\pi\hbar}\right)^{\frac{1}{4}}e^{-\frac{m\omega_0x^2}{2\hbar}}H_n\left(\sqrt{\frac{m\omega_0}{\hbar}}x\right). \quad (2.6)$$

Here, $H_n(x)$ are the Hermite polinomials. They are defined in terms of ${}_2F_0$ confluent hypergeometric functions [12]:

$$H_n(x)=(2x)^n\ {}_2F_0\left(\begin{matrix}-\frac{n}{2}, & -\frac{(n-1)}{2}\\ - & \end{matrix};\ \frac{1}{x^2}\right).$$

Wave functions (2.6) are ortonormalized in the whole real position range $(-\infty,+\infty)$:

$$\int_{-\infty}^{\infty}\psi_m^*(x)\psi_n(x)dx=\delta_{mn}.$$

This relation has been obtained via the following known orthogonality relation of Hermite polinomials $H_n(x)$:

$$\frac{1}{\sqrt{\pi}}\int_{-\infty}^{\infty}e^{x^2}H_m(x)H_n(x)dx=2^n n!\,\delta_{mn}.$$

3. EXACT SOLUTION OF THE CONFINED POSITION-DEPENDENT MASS HARMONIC OSCILLATOR MODEL IN TERMS OF THE GEGENBAUER POLYNOMIALS

This section deals with exact solution of the quantum harmonic oscillator problem confined in the finite region, which effective mass behaves itself as varying with position and being compatible with Galilean invariance. Beauty of such alternative method for description of the effective mass formalism within the non-relativistic quantum problem is the certain position dependency function that can also generate confinement effect as a hidden property of the model under consideration.

One of the approaches taking into account the mass varying with position in the kinetic energy operator is the approach that allows to introduce the following analytical expression of the kinetic energy operator compatible with Galilean invariance [13]:

$$\widehat{H}_0^{GI}=-\frac{\hbar^2}{6}\left[\frac{1}{M(x)}\frac{d^2}{dx^2}+\frac{d}{dx}\frac{1}{M(x)}\frac{d}{dx}+\frac{d^2}{dx^2}\frac{1}{M(x)}\right]. \quad (3.1)$$

Here, $M(x)$ is the effective mass varying with position. If one introduces confined harmonic oscillator potential as

$$V(x)=\begin{cases}\frac{M(x)\omega^2x^2}{2}, & |x|<a,\\ \infty, & |x|\geq a.\end{cases} \quad (3.2)$$

then, the Hamiltonian describing the quantum harmonic oscillator problem confined in the finite region will have the following expression:

$$\widehat{H}^{GI}=-\frac{\hbar^2}{6}\left[\frac{1}{M(x)}\frac{d^2}{dx^2}+\frac{d}{dx}\frac{1}{M(x)}\frac{d}{dx}+\frac{d^2}{dx^2}\frac{1}{M(x)}\right]+\frac{M(x){\omega_0}^2x^2}{2}. \quad (3.3)$$

Performing easy computations one observes that (3.3) can be simplified as follows:

$$\widehat{H}^{GI}=-\frac{\hbar^2}{2M}\left[\frac{d^2}{dx^2}-\frac{M'}{M}\frac{d}{dx}-\frac{1}{3}\frac{M''}{M}+\frac{2}{3}\left(\frac{M'}{M}\right)^2\right]+\frac{M(x){\omega_0}^2x^2}{2}. \quad (3.4)$$

Position-dependent effective mass $M\equiv M(x)$ is only the function that is still indefinite in eq.(3.4). It can be defined within the following conditions:

- position-dependent effective mass $M(x)$ equals to constant mass m_0 at origin of position $x=0$ and also recovers it under the limit $a\to\infty$;
- confinement effect at values of position $x=\pm a$ is achieved via the definition of the position-dependent effective mass $M(x)$;
- stationary Schrödinqer equation for the Hamiltonian $\widehat{H}^{GI}$ (3.4) becomes exactly solvable and analytical solutions correctly recover Hermite oscillator solutions (2.5) & (2.6) under the limit $a\to\infty$.

We define position-dependent effective mass $M(x)$ satisfying the listed above conditions via the following analytical expression:

$$M \equiv M(x) = \frac{a^2 m_0}{a^2 - x^2}. \quad (3.5)$$

Checking listed above conditions for the position-dependent effective mass $M(x)$ (3.5), one observes that it equals to constant mass m_0 under condition $M(0) = m_0$ and also recovers constant mass m_0 under the following limit relation:

$$\lim_{a\to\infty} \frac{a^2 m_0}{a^2 - x^2} = m_0. \quad (3.6)$$

Aslo, one observes that potential (3.2) with position-dependent effective mass $M(x)$ (3.5) satisfies the following boundary conditions:

$$V(-a) = V(a) = \infty.$$

The final condition that one needs to check is exact solubility of the following Schrödinger equation with the Hamiltonian (3.4):

$$\widehat{H}^{GI}\psi^{GI} = E^{GI}\psi^{GI}. \quad (3.7)$$

By substitution of (3.4)&(3.5) at (3.7) and performing easy mathematical computations, one can write down the Schrödinger equation as follows:

$$\frac{d^2\psi^{GI}}{dx^2} - \frac{2x}{a^2 - x^2}\frac{d\psi^{GI}}{dx} + \frac{\left(\frac{2m_0 a^2 E^{GI}}{\hbar^2} - \frac{2}{3}\right)(a^2 - x^2) - \frac{{m_0}^2{\omega_0}^2 a^4}{\hbar^2}x^2}{(a^2 - x^2)^2}\psi^{GI} = 0. \quad (3.8)$$

Now, one introduces new dimensionless variable $\xi = x/a$, which allows to rewrite eq.(3.8) in more compact form

$$\psi'' + \frac{\tilde{\tau}}{\sigma}\psi' + \frac{\tilde{\sigma}}{\sigma^2}\psi = 0. \quad (3.9)$$

Here, $\psi \equiv \psi^{GI}$, $\tilde{\tau}$ is a polynomial of at most first degree, but σ and $\tilde{\sigma}$ are polynomials of at most second degree having the following mathematical expression:

$$\tilde{\tau} = -2\xi,\ \sigma = 1 - \xi^2,\ \tilde{\sigma} = \left(c_0 - \frac{2}{3}\right) - \left(c_2 - \frac{2}{3}\right)\xi^2,$$
$$c_0 = \frac{2m_0 a^2 E^{GI}}{\hbar^2},\ c_2 = c_0 + \frac{{m_0}^2{\omega_0}^2 a^4}{\hbar^2}.$$

Eq.(3.9) is exactly soluble second order differential equation of the hypergeometric type. There are various methods for its exact solution. One of such methods, which can be applied here is Nikiforov-Uvarov method for solution of the second order differential equations [14].

We assume that the wave function of the Schrödinger equation (3.9) has the following form:

$$\psi = \varphi(\xi)y(\xi), \quad (3.10)$$

where, $\varphi(\xi)$ is defined as

$$\varphi(\xi) = e^{\int\frac{\pi(\xi)}{\sigma(\xi)}d\xi}, \quad (3.11)$$

with $\pi(\xi)$ being at most a polynomial of first order. Also, by performing simple computations, one can show that

$$\psi' = \varphi y' + \frac{\pi}{\sigma}\varphi y,$$
$$\psi'' = \varphi y'' + \frac{2\pi}{\sigma}\varphi y' + \frac{\pi'\sigma - \pi\sigma + \pi^2}{\sigma^2}\varphi y.$$

Their substitution at eq.(3.9) leads to the following equation for $y(\xi)$:

$$y'' + \frac{2\pi + \tilde{\tau}}{\sigma}y' + \frac{\tilde{\sigma} + \pi^2 + \pi(\tilde{\tau} - \sigma') + \pi'\sigma}{\sigma^2}y = 0. \quad (3.12)$$

One can easily check that $\tilde{\tau} - \sigma' = 0$. Then, by introducing

$$\bar{\tau} = 2\pi + \tilde{\tau}$$

and

$$\bar{\sigma} = \tilde{\sigma} + \pi^2 + \pi'\sigma,$$

eq.(3.12) can be written in more compact form as follows:

$$y'' + \frac{\bar{\tau}}{\sigma}y' + \frac{\bar{\sigma}}{\sigma^2}y = 0. \quad (3.13)$$

Next, taking into account that $\bar{\sigma}$ is also a polynomial of at most second order, one can assume that $\bar{\sigma} = \lambda\sigma$. Then, we can rewrite (3.13) in the following more compact form:

$$y'' + \frac{\bar{\tau}}{\sigma}y' + \frac{\lambda}{\sigma}y = 0. \quad (3.14)$$

At same time, one observes that

$$\pi = \varepsilon\sqrt{\mu\sigma - \tilde{\sigma}} = \varepsilon\sqrt{\left(\mu + \frac{2}{3} - c_0\right) - \left(\mu + \frac{2}{3} - c_2\right)\tilde{\sigma}},$$

where, $\mu = \lambda - \pi'$ and $\varepsilon = \pm 1$. Now, taking into account that π should be a polynomial at most of first degree, one observes that this condition is true if $\mu + \frac{2}{3} = c_0$ or $\mu + \frac{2}{3} = c_2$. Then, it means that we have four different solutions for π in terms of (ε, μ) pairs: $\left(+1, c_0 - \frac{2}{3}\right)$, $\left(+1, c_2 - \frac{2}{3}\right)$, $\left(-1, c_0 - \frac{2}{3}\right)$ and $\left(-1, c_2 - \frac{2}{3}\right)$. By computing exact expression of $\varphi(\xi)$, one can find that only at the value $\left(+1, c_0 - \frac{2}{3}\right)$, the wave function vanishs at $\xi = \pm 1$ $(x = \pm a)$. Then, one easily obtains that

$$\pi(\xi) = -\frac{m_0\omega_0 a^2}{\hbar}\xi,$$
$$\lambda = \frac{2m_0 a^2 E^{GI}}{\hbar^2} - \frac{m_0\omega_0 a^2}{\hbar} - \frac{2}{3},$$
$$\varphi(\xi) = (1 - \xi^2)^{\frac{m_0\omega_0 a^2}{2\hbar}}.$$

Taking into account that λ is known, then eq.(3.14) can be solved exactly through its comparison with the following second order differential equation for the Gegenbauer polynomials $C_n^{\bar{\lambda}}(x)$:

$$(1 - x^2)\bar{y}'' - \left(2\bar{\lambda} + 1\right)x\bar{y} + n\left(n + 2\bar{\lambda}\right)\bar{y} = 0, \quad (3.15)$$
$$\bar{y} = C_n^{\bar{\lambda}}(x).$$

From this comparison one obtains that energy spectrum E_n^{GI} is non-equidistant and has the following expression:

$$E_n^{GI} = \hbar\omega_0\left(n + \frac{1}{2}\right) + \frac{\hbar^2}{2m_0 a^2}n(n+1) + \frac{\hbar^2}{3m_0 a^2}. \quad (3.16)$$

The wave functions of the stationary states ψ^{GI} expressed through the Gegenbauer polynomials by the following manner:

$$\tilde{\psi}^{GI}(x) = c_n^{GI}\left(1 - \frac{x^2}{a^2}\right)^{\frac{m_0\omega_0 a^2}{2\hbar}} C_n^{\left(\frac{m_0\omega_0 a^2}{\hbar} + \frac{1}{2}\right)}\left(\frac{x}{a}\right). \quad (3.17)$$

Here, Gegenbauer polynomials $C_n^{(\bar{\lambda})}(x)$ are defined in terms of the ${}_2F_1$ hypergeometric functions as follows [12]:

$$C_n^{(\bar{\lambda})}(x) = \frac{(2\bar{\lambda})_n}{n!} \; {}_2F_1\left(\begin{matrix}-n, n+2\bar{\lambda} \\ \bar{\lambda}+\frac{1}{2}\end{matrix};\ \frac{1-x}{2}\right), \bar{\lambda} \neq 0.$$

$\tilde{\psi}^{GI}$ is orthonormalized and differs from ψ^{GI} due to multiplied normalization factor c_n^{GI}, which is obtained from the following orthogonality relation for the Gegenbauer polynomials:

$$\int_{-1}^{1}(1-x^2)^{\bar{\lambda}-\frac{1}{2}} C_m^{(\bar{\lambda})}(x) C_n^{(\bar{\lambda})}(x)dx = \frac{\pi\Gamma(n+2\bar{\lambda})2^{1-2\bar{\lambda}}}{\{\Gamma(\bar{\lambda})\}^2(n+\bar{\lambda})n!}\delta_{mn}.$$

Its exact expression is the following:

$$c_n^{GI} = 2^{\frac{m_0\omega_0 a^2}{\hbar}}\Gamma\left(\frac{m_0\omega_0 a^2}{\hbar}+\frac{1}{2}\right)\sqrt{\frac{\left(n+\frac{m_0\omega_0 a^2}{\hbar}+\frac{1}{2}\right)n!}{\pi a\Gamma\left(n+\frac{2m_0\omega_0 a^2}{\hbar}+1\right)}}.$$

Taking into account that exact expressions of the energy spectrum and wave functions of the stationary states are found by solving the Schrödinger equation (3.7), this statement partly proves the final condition that introduced position-dependent effective mass $M(x)$ (3.5) needed to satisfy. We are going to discuss different properties and possible limit relations of these exact expressions within next Section.

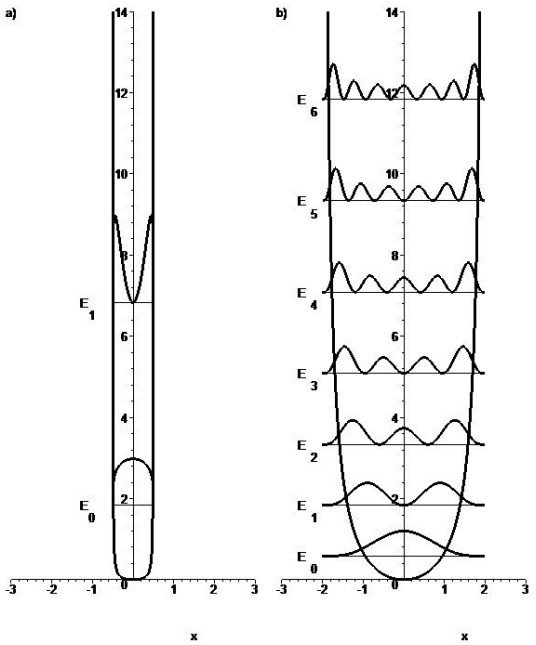

Fig. 1. Confined quantum harmonic oscillator potential (3.3) and behaviour of the corresponding non-equidistant energy levels (3.16) and probability densities $\left|\tilde{\psi}^{GI}(x)\right|^2$ of the ground and a) **1** excited state for value of the confinement parameter $\boldsymbol{a = 0.5}$; b) **6** excited state for value of the confinement parameter $\boldsymbol{a = 2}$ ($\boldsymbol{m_0 = \omega_0 = \hbar = 1}$).

4. DISCUSSION AND CONCLUSIONS

Taking into account that our main goal aiming to solve exactly the confined quantum harmonic oscillator model with position-dependent effective mass and kinetic energy operator compatible with Galilean invariance and show that obtained exact solutions under certain limit recover well-known Hermite oscillator model is achieved partially, namely, exact solution in terms of the wave functions of the stationary states and discrete energy spectrum are obtained, now one needs to explore further the possible limit from vanishing at finite region to infinite one. Confinement parameter a in fact restricts our oscillator model within the deep potential well with a width that equals to $2a$. Then, possible limit that one needs to apply here to expression of the discrete non-equidistant energy spectrum (3.16) and wave functions in terms of the Gegenbauer poynomials (3.17) is $a \to \infty$.

In Fig.1, we depicted both confined harmonic oscillator potential (3.2) with energy spectrum (3.16) and probability densities $\left|\tilde{\psi}^{GI}(x)\right|^2$ computed from the wave functions (3.17) and corresponding to energy spectrum (3.16). Two different values of the confinement parameter a is considered as an example - $a = 0.5; 2.0$. One observes from these two pictures that confinement parameter close to zero drastically changes the behaviour of the model under consideration from the quantum harmonic oscillator to infinite quantum well. Then of course, the question arises on mathematical base of such a behaviour.

Mathematical base of the correct recover of the known Hermite oscillator model is based on the following asymptotics and limit relations:

$$\Gamma(z) \underset{z\to\infty}{\cong} \sqrt{\frac{2\pi}{z}}e^{z\ln z - z},$$

$$\Gamma(\alpha+1/2) \underset{\alpha\to\infty}{\cong} \sqrt{2\pi}e^{\alpha\ln\alpha-\alpha}, \alpha = \frac{m_0\omega_0 a^2}{\hbar},$$

$$\lim_{a\to\infty}\Gamma(n+2\alpha+1) \cong 2^n\sqrt{4\pi\alpha}e^{(2\alpha+n)\ln\alpha-2\alpha+2\alpha\ln 2},$$

$$\lim_{\alpha\to\infty}\alpha^{\frac{n}{2}}c_n^{GI} = \tilde{c}_0\sqrt{\frac{n!}{2^n}}, \quad \tilde{c}_0 = \left(\frac{m_0\omega_0}{\pi\hbar}\right)^{1/4}.$$

$$\lim_{a\to\infty}\left(1-\frac{x^2}{a^2}\right)^{\frac{1}{2}\sqrt{\alpha^2+1}} = e^{-\frac{m_0\omega_0 x^2}{2\hbar}}.$$

By applying these relations, one can easily to show the correctness of the following limit relation:

$$\lim_{a\to\infty}\psi_n^{GI}(x) = \psi_n(x).$$

This limit relation completes the proof of the correctness of the final condition for the position-dependent effective mass $M(x)$.

We do not discuss more details of the model that is presented in this paper, but at conclusions it is necessary to highlight an importance of such models due to recent development mothods, allowing to fabricate infinite quantum well structures with shapes different than traditional square-like behaviours.

ACKNOWLEDGEMENTS

E.I. Jafarov kindly acknowledges that this work was supported by the Scientific Fund of State Oil Company of Azerbaijan Republic 2019-2020 **Grant Nr 13LR-AMEA** and the Science Development Foundation under the President of the Republic of Azerbaijan – **Grant Nr EIF-KETPL-2-2015-1(25)-56/01/1**.

[1] *M. Moshinsky and Y.F. Smirnov*. The harmonic oscillator in modern physics (New York: Harwood Academic, 1996).
[2] *S.C. Bloch.* Introduction to classical and quantum harmonic oscillators (Wiley, New-York, 1997).
[3] *L.D. Landau and E.M. Lifshitz*. Quantum mechanics (Non-relativistic Theory) (Oxford: Pergamon, 1991).
[4] *F.C. Auluck*. 1941 Proc. Indian Nat. Sci. Acad. 7 133-140.
[5] *S. Chandrasekhar*. 1943 Astrophys. J. 97 263-273.
[6] *F.C. Auluck and D.S. Kothari*. 1945 Math. Proc. Camb. Phil. Soc. 41 175-179.
[7] *A. Consortini and B.R. Frieden*. 1976. Nuovo Cim. B 35 153-164.
[8] *F.C. Rotbart*. 1978 J. Phys. A: Math. Gen. 11 2363-2368.
[9] *A.H. MacDonald and P. Středa*. 1984. Phys. Rev. B 29 1616-1619.
[10] *M. Grinberg et al.* 1994. Phys. Rev. B 50 6504-6507.
[11] *W.A. Harrison*. 1961 *Phys. Rev*. 123 85-89.
[12] *R. Koekoek, P.A. Lesky and R.F. Swarttouw*. Hypergeometric orthogonal polynomials and their q-analogues (Springer Verslag, Berlin, 2010).
[13] *J.R.F. Lima et al*. 2012 *J. Math. Phys*. 53 072101
[14] *A.F. Nikiforov and V.B. Uvarov*. Special Functions of Mathematical Physics (Birkhäuser, Basel, 1988).

Received: 19.10.2020

POLARIZATION PROPERTIES OF γ-QUANTA IN $H \Rightarrow f + \bar{f} + \gamma$ DECAYİNG

F.A. SADDİGH
Scientific advisor at Idrak Technology Transfer
mirfarhad.saddigh@idrak.az

We have analyzed the Higgs-boson decaying process of $H \Rightarrow f + \bar{f} + \gamma$ based on the Feynman diagram. While considering the helicity of fermion-antifermion and the linear (circular) polarization , the cross-section of the $H \Rightarrow f + \bar{f} + \gamma$ in the framework of the standard model (SM) has been calculated. The linear or the circular polarization of the $\gamma -$ quanta has been evaluated and the dependency of the fermion-antifermion pair over the x i.e. the invariant mass and the exiting θ angle has been investigated.

The value for the linear and circular polarization of the γ-quanta during the $H \Rightarrow \tau^- + \tau^+ + \gamma$ has been shown.

Keywords: Higgs Boson, Standard Model, γ-quanta polarization, Scattering matrix, Electroweak interaction, tau leptons.
PACS: 13.88.+e ,

1. INTRODUCTION

Based on $SU_c(3)\times SU_l(2)\times U_y(1)$ symmetry, the standard model (SM) predicts and describe all the phenomena of strong, weak and electromagnetic forces.

The main part of this model is the spontaneous symmetry breaking via higgs mechanism. In this process, the non-zero scalar field is being introduced. Because of interaction with this field and based on the computations of quantum electrodynamics, the higgs particles are being created. Thanks to ATLAS and CMS collaboration the higgs boson was finally discovered in 2012(see reference [5-7]).

Higgs boson is an unstable particle and will be decayed through different channels [2,8-10].

In Large Hadron Collider (LHC), it is through the following channels $H \Rightarrow \gamma + \bar{\gamma}$ two photon decaying, 2 electron-positron pair and 2 muon-antimuon channels. The mentioned channels are as follow $H \Rightarrow e^- + e^+ + e^- + e^+$, $H \Rightarrow e^- + e^+ + \mu^- + \mu^+$, $H \Rightarrow \mu^- + \mu^+ + \mu^- + \mu^+$.

These decaying are being shown as follow:

$$H \Rightarrow zz^* \Rightarrow 4l$$

Here, z is the real and $z^*$the virtual boson while l signifies one of the $e^{\pm}$ or $\mu^{\pm}$.

In ATLAS and CMS the decaying of $H \Rightarrow WW^* \Rightarrow l_v l_v$ is also being discovered where the W is the real and W^* is virtual boson while υ is the electron neutrino (or even muon neutrino).

Higs boson in most cases is being decayed into $H \Rightarrow b + \bar{b}$ where the $b\bar{b}$ pair is one of the most observed phenomena in proton-proton and proton-anti proton collision. This state occurs even at the absence of Higgs boson. Because of this selecting information regarding higgs boson is very difficult. So, as a result of processes like this, during the collision of proton-proton, the higgs boson are produced with the W boson at the same time and the w boson is decayed to υ_e pair. Here e is either $e^{\pm}$ or $\mu^{\pm} H \Rightarrow b + \bar{b}$, $Z \Rightarrow 2e$ or $Z \Rightarrow 2\upsilon$ decayings are also a result of $p + p \Rightarrow z + H$. Unfortunately in LHC selection of these reactions from the background has not been possible.

One of the main channels for the decaying of higgs boson are the following channels of $H \Rightarrow \gamma + e, H \Rightarrow \gamma + Z$. Besides these channels, it creates the radiative reactions of higgs boson of $H \Rightarrow f + \bar{f} + \gamma$ that are very interesting. Here $f\bar{f}$ signifies fermion-antifermion pairs [11-15].

In this work, the cross section for the process is carried out and the distribution over the angles and energies has being researched and the assymetry for longitudinal and transverse polarization problems has been investigated. The features of Gamma quantas though has been ignored. For now, the main goals for the current work is to study the cross section of the decay, while considering the linear and circular polarization of $H \Rightarrow \tau^- + \tau^+ + \gamma$ while obtaining numerical results.

2. THE AMPLİTUDE OF $H \Rightarrow f\bar{f}\gamma$ DECAYİNG

The radiative higgs boson decay $H \Rightarrow f + \bar{f} + \gamma$ takes place through the feynman diagrams depicted in fig.1. Based on these diagrams the higgs boson is first decayed to fermion-antifermion and then emits γ-quanta.

The amplitude for this procss is given by:

$$M_{i\to f} = iA_0 Q_f \left[\bar{u}_f(p_1,\lambda_1) R \vartheta_f(p_2,\lambda_2)\right] \qquad (2)$$

Where

$$A_0 = -\frac{2\pi\alpha_{KED} m_f}{M_w \sin\theta_w} \qquad (3)$$

$$R = \hat{e}^* \frac{\widehat{p_1}+\hat{k}+m_f}{(p_1+k)^2-m^2 f} - \frac{\widehat{p_2}+\hat{k}+m_f}{(p_2+k)^2-m^2 f}\ \hat{e}^* \qquad (4)$$

Here θ_w is the weinberg angle , M_w stands for the mass of the boson, $P, P_1, P_2 and\ K$ are the 4-momentum of higgs boson,fermion-antifermion and γ-quanta. $\lambda_1 and \lambda_2$ shpw the chirality of fermion-antifermion and e^* is the four-vector for the polarization of γ-quanta.

131, H.Javid ave, AZ-1143, Baku
ANAS, Institute of Physics
E-mail: jophphysics@gmail.com

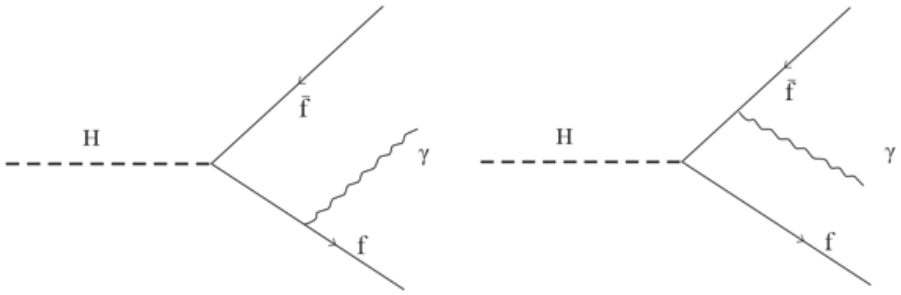

Fig.1.

Using Dirac equation,

$$\bar{u}_f(p_1,\lambda_1)\left(\widehat{p_1}-m_f\right)=0,\quad \left(\widehat{p_2}+m_f\right)\vartheta_f(p_2,\lambda_2)=0 \qquad (5)$$

We will get the following for the R:

$$\hat{R}=\frac{2(e^*,p_1)+\hat{e}^*\hat{k}}{2(p_1\cdot k)}-\frac{2(e^*,p_2)+\hat{e}^*\hat{k}}{2(p_2\cdot k)} \qquad (6)$$

The amplitude of the relation (2) in the system of equation $(\overrightarrow{p_1}+\overrightarrow{p_2}=0,\vec{p}=\vec{k})$ will give the relation as follow:

$$\left|M_{i\to f}\right|^2=\frac{A_0^2}{2}\left(\frac{1}{(p_1\cdot k)}+\frac{1}{(p_2\cdot k)}\right)^2\{(1+\lambda_1\lambda_2)[M_H^2(ep_1)(ep_1{}^*)+(p_1\cdot k)(p_2\cdot k)]-$$
$$i(\lambda_1+\lambda_2)[(ep_1)(p_1p_2ke^*)_\varepsilon-(e^*\cdot p_1)(p_1p_2ke)_\varepsilon+(k\cdot p_2)(p_1ke^+e)_\varepsilon]\} \qquad (7)$$

where the $(abcd)_\varepsilon$ is being considered.

The cross section for the decaying of higgs-boson is proportional to the square of $\left|M_{i\to f}\right|(i.e.\left|M_{i\to f}\right|^2)$.

$$d\Gamma\left(H\Rightarrow f\bar{f}\gamma\right)=\frac{1}{2E_H}\left|M_{i\to f}\right|^2 d\Phi \qquad (8)$$

where the $d\phi$ is the invariant volume of the phases.

$$d\Phi=(2\pi)^4\frac{d\overrightarrow{p_1}}{(2\pi)^3\cdot 2E_1}\cdot\frac{d\overrightarrow{p_2}}{(2\pi)^3\cdot 2E_2}\cdot\frac{d\vec{k}}{(2\pi)^3\cdot 2E_\gamma}\ \delta(p-p_1-p_2-k) \qquad (9)$$

The heavier the mass of the fermion, the stronger the interaction of the fermion-antifermion pair will be causing the constant of interaction to be larger. we get from here that the higgs boson mass equal to $M_H=125Gev$ will decay to $\tau\tau^+$, $c\bar{c}$ and $b\bar{b}$ fermion pairs. Because of the low value for its mass the followig decaying channels of $H\Rightarrow e^-+e^++\gamma$, $H\Rightarrow\mu^-+\mu^++\gamma$, $H\Rightarrow u+\bar{u}+\gamma$, $H\Rightarrow d+\bar{d}+\gamma$ and $H\Rightarrow s+\bar{s}+\gamma$ are not possible.

The $H\Rightarrow\tau^-+\tau^++\gamma$ radiation decaying is also very attractive meaning $\tau^-\Rightarrow\pi^-+\upsilon_\tau$, $\tau^-\Rightarrow K^-+\upsilon_\tau$, $\tau^-\Rightarrow\rho^-+\upsilon_\tau$ decaying channels allow us to measure the polarization. Additionally during $H\Rightarrow\tau^-+\tau^++\gamma$, the γ-quanta can obtain the linear or circular polarization and its measurement will make possible to investigate some feature of the higgs boson. The squared fraction for radiative reactions $H\Rightarrow q^-+q^++\gamma$, $H\Rightarrow c+\bar{c}+\gamma$ and $H\Rightarrow b+\bar{b}+\gamma$ are $(\frac{m_\tau}{M_H})^2=0.0002\ll 1$ and $(\frac{m_b}{M_H})^2=0.0015\ll 1$. Because of this, in the cross section calculation, we can ignore the related $\varepsilon\frac{m_f^2}{M_H^2}$.

3. THE LİNEAR POLARİZATİON OF γ - QUANTA

At the center of the fermion-antifermion pairs, the angle θ is the polar angle and φ the azimuthal angle. At the center of the fermion-antifermion pair, the cross section of $H\Rightarrow f+\bar{f}+\gamma$ for the linearly polarized γ quanta is given by:

$$\frac{d\Gamma(\vec{e})}{dx\,d\Omega}=\frac{A_0^2\,M_H\vartheta}{2^{12}\pi^4(1-x)}\cdot\frac{N_C(1+\lambda_1\lambda_2)}{(1-\vartheta^2\cos^2\theta)^2}\ [4x\vartheta^2(\vec{e}\vec{n})^2+(1-x)^2(1-\vartheta^2\cos^2\theta)] \qquad (10)$$

Here $d\Omega=d(\cos\theta)d\varphi$ is the angle of the emission for the fermion f and the x is the invariant mass for the fermion-anti fermions in M_H^2 units.

$$x=\frac{s}{M_H^2}=\frac{(p_1+p_2)^2}{M_H^2}$$

Where $v = \sqrt{1 - 4m_f^2/s}$ is the velocity of fermion and the N_c is the constant of quark (lepton) pair production$N_c = 3(1)$.

From the equation (10) for the cross section of the decay we get that the helicity for fermion-anti fermion must be equal (λ1= λ2=±1). So fermion-anti fermion will either have right polarization fr,fr or left polarization fl,fl. This is the result of conservation of energy in $H \Rightarrow f + \bar{f}$ decaying.

The cross section for the γ-quanta decaying along x ($\vec{e} = \overrightarrow{e_x}$) and y (($\vec{e} = \overrightarrow{e_y}$)) is given by the relation (11) and (12).

$$\frac{d\Gamma(\overrightarrow{e_x})}{dx\, d\Omega} = \frac{A_0^2\, M_H \vartheta}{2^{10}\pi^4(1-x)} \cdot \frac{N_C}{(1-\vartheta^2\cos^2\theta)^2} \left[4x\vartheta^2 \sin^2\theta\cos^2\varphi + (1-x)^2(1-\vartheta^2\cos^2\theta)\right] \quad (11)$$

$$\frac{d\Gamma(\overrightarrow{e_y})}{dx\, d\Omega} = \frac{A_0^2\, M_H \vartheta}{2^{10}\pi^4(1-x)} \cdot \frac{N_C}{1-\vartheta^2\cos^2\theta} \left[4x\vartheta^2 \sin^2\theta\sin^2\varphi + (1-x)^2(1-\vartheta^2\cos^2\theta)\right] \quad (12)$$

According to equation 13(mentioned below) we are now going to evaluate the order(magnitude) of linear polarization for the γ-quanta.

$$P_\gamma(\vec{e}) = \frac{d\Gamma(\overrightarrow{e_x})/dx\, d\Omega - d\Gamma(\overrightarrow{e_y})/dx\, d\Omega}{d\Gamma(\overrightarrow{e_x})/dx\, d\Omega + d\Gamma(\overrightarrow{e_y})/dx\, d\Omega} = \frac{2x\vartheta^2\sin^2\theta\cos 2\varphi}{2x\vartheta^2\sin^2\theta + (1-x)^2(1-\vartheta^2\cos^2\theta)} \quad (13)$$

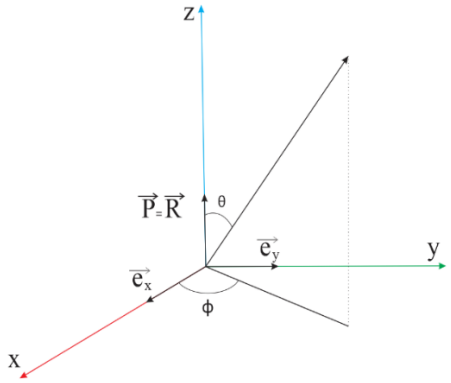

Fig .2. The Polarization of fermion-antifermion pair for polar θ-angle and φ-azimuthal angle.

The maximum value for linear polarization for the γ quanta appears to be at azimuthal angle of φ=0.in figure 3 the linear polarization is being depicted for the γ-quanta at the θ=90 and mH=125 Gev and m_τ=1.778 Gev over the x variable for the $H \Rightarrow \tau^- + \tau^+ + \gamma$ decaying. It is seen from the diagram that as x increases the linear polarization of the γ-quanta will increase monotonically and at the end of the spectrum at x=1 obtains its highest value of p(γ=100%). At the maximum value of invariant mass(x=1) the photon will have the lowest possible energy.

Correspondingly, the higgs bosons during $H \Rightarrow f + \bar{f} + \gamma$ decaying will give rise to the light photons of linear polarization.

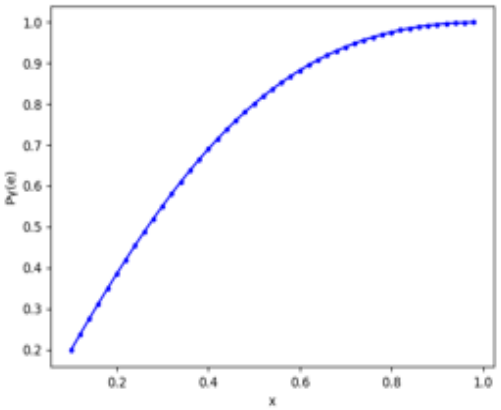

Fig.3. The x-dependency of magnitude of linear polarization of γ-quanta at θ=90º.

By summation for the polarization of γ-quanta in eq-10:

$$\sum_e (\vec{en})^2 = (\overrightarrow{e_x}\vec{n})^2 + (\overrightarrow{e_y}\vec{n})^2 = sin^2\theta(cos^2\varphi + sin^2\varphi) = sin^2\theta$$

We will get the following cross section for $H \Rightarrow f + \bar{f} + \gamma$:

$$\frac{d\Gamma}{dx\, d(\cos\theta)} = \frac{A_0^2 M_H N_C \vartheta}{128\,\pi^3} \cdot \frac{1+x^2}{(1-x)(1-\vartheta^2\cos^2\theta)} \quad (14)$$

Fig 4 shows the width of $H \Rightarrow \tau^- + \tau^+ + \gamma$ decaying for$M_H = 125Gev$, $M_w = 80.385\,Gev$, $sin^2\theta_w = 0.2315$ for differnet invariant mass of $x = 0.2; x = 0.5; x = 0.8$; over the emittied θ angle.

As θ increases the width of the decaying $H \Rightarrow \tau^- + \tau^+ + \gamma$ increase and at $\theta = 90$ obtains its maximumvalue. The further increse of θ will decrease the width. The further increase of θ will decrease the width. The increase in fermion-antifermion invariant mass (by decreasing the width of γ-quanta) will increase the width of the decaying.

By integrating the relation 14 for the decay over emitting angle we will obtain the relation of tau-lepton decaying over the invariant mass:

$$\frac{d\Gamma}{dx} = \frac{A_0^2 M_H}{128\,\pi^3} \cdot \frac{1+x^2}{(1-x)} \cdot \ln\frac{1+\vartheta}{1-\vartheta} \qquad (15)$$

Figure 5 depicts the width of decaying of $H \Rightarrow \tau^- + \tau^+ + \gamma$ over the invariant mass. According to the diagram, increasing the energy obtained from fermion-antifermion pair will result in the increase of the width of $d\Gamma(H \Rightarrow \tau^- + \tau^+ + \gamma)/dx$.

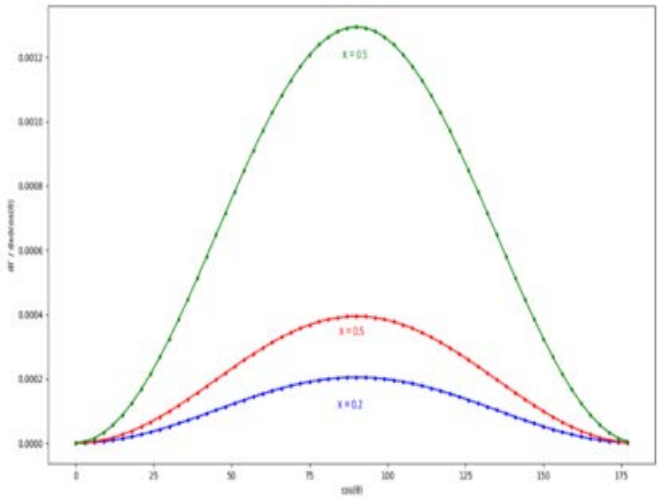

Fig.4 . The $H \Rightarrow \tau^- + \tau^+ + \gamma$ decaying for different x over emitting angle.

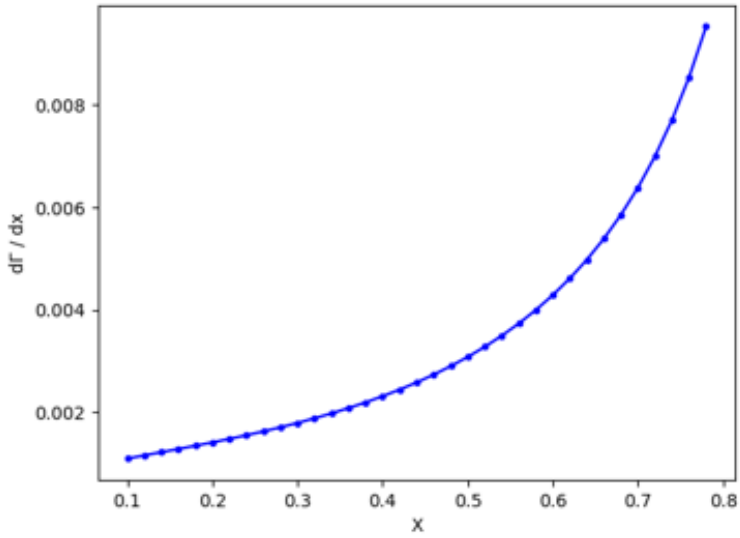

Fig. 5. Width of the $H \Rightarrow \tau^- + \tau^+ + \gamma$ decaying and its dependency over the invariant mass x.

4. CİRCULAR POLARİZATİON OF γ-QUANTA

Let's observe the polarization of γ-quanta from fermion-antifermion during $H \Rightarrow f + \bar{f} + \gamma$ decaying. The circular polarization vectors for the γ-quanta are:

$$\vec{e} = \frac{1}{\sqrt{2}}\left(\vec{\beta} + i\, s_\gamma\, [\vec{n}_0\vec{\beta}]\right),\ \vec{e}^{\,*} = \frac{1}{\sqrt{2}}\left(\vec{\beta} i\, s_\gamma\, [\vec{n}_0\vec{\beta}]\right) \qquad (16)$$

Here, $\vec{n}_0$ and $\vec{\beta}$ quantities,respectively, stand for the orientation of unit vectors of themomentum vector and prependicular to them. The $s_\gamma = \pm 1$ though characteriz the right and left polarization of the γ-quanta.
The $\vec{e}$ and $\vec{e}^{\,*}$ polarization vectors have the following properties:

$$(\vec{e}\vec{e}^{\,*}) = 1, [\vec{e}\vec{e}^{\,*}] = -i\, s_\gamma \vec{n}_0, [\vec{e}\vec{n}_0] = i\, s_\gamma \vec{e}, [\vec{n}_0\vec{e}^{\,*}] = i\, s_\gamma \vec{e}^{\,*}$$

The width of the decaying $H \Rightarrow f + \bar{f} + \gamma$, while considering the circular polarization of γ-quanta is being given by:

$$\frac{d\Gamma(\lambda_1;S_\gamma)}{dxd(\cos\theta)} = \frac{A_0^2 M_H \vartheta}{2^{10}\pi^3(1-x)} \cdot \frac{N_C}{(1-\vartheta^2\cos^2\theta)^2} \cdot \{(1+\lambda_1\lambda_2)(1+x^2)(1-\vartheta^2\cos^2\theta) + S_\gamma(\lambda_1+\lambda_2)(1-x)[2x\vartheta^2\sin^2\theta + (1-x)(1-\vartheta^2\cos^2\theta)]\} \quad (17)$$

the order of the circular polarization of γ-quanta is obtained using eq.18:

$$P_\gamma(S_\gamma) = \frac{\frac{d\Gamma(\lambda_1;S_\gamma=1)}{dxd(\cos\theta)} - \frac{d\Gamma(\lambda_1;S_\gamma=-1)}{dxd(\cos\theta)}}{\frac{d\Gamma(\lambda_1;S_\gamma=1)}{dxd(\cos\theta)} + \frac{d\Gamma(\lambda_1;S_\gamma=-1)}{dxd(\cos\theta)}} = \lambda_1 \cdot \frac{(1-x)[2x\vartheta^2\sin^2\theta + (1-x)(1-\vartheta^2\cos^2\theta)]}{(1+x^2)(1-\vartheta^2\cos^2\theta)} \quad (18)$$

Figure 6 depicts the order of circular polarization for γ-quanta at $\lambda_1 = -1$ for the $H \Rightarrow \tau^- + \tau^+ + \gamma$over the θ angle.

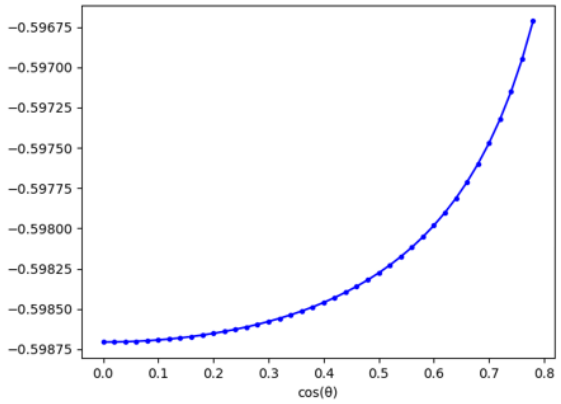

Fig. 6. $P_\gamma(S_\gamma)$ dependency over cos θ.

As it is seen the order of circular polarization for γ-quanta is negative and it can be said that it is independent of the θ angle. The energy obtained from fermion-antifermion pair cause the order of circular polarization to get reduced.

By integrating the equation 17 over the θ angle the spectrum of fermion-antifermion pair will get us the following relation:

$$\frac{d\Gamma(\lambda_1;S_\gamma)}{dx} = \frac{A_0^2 M_H \vartheta}{2^9\pi^3}\frac{N_C}{1-x}\{(1+x^2)L + S_\gamma\lambda_1(1-x)[-2x+(1+x\vartheta^2 L)]\} \quad (19)$$

where $L = \frac{1}{v} ln \frac{1+v}{1-v}$.

We can calculate the order of circular polarization of γ-quanta by the following relation:

$$P_\gamma(S_\gamma) = \frac{d\Gamma(\lambda_1;S_\gamma=1)/dx - d\Gamma(\lambda_1;S_\gamma=-1)}{d\Gamma(\lambda_1;S_\gamma=1)/dx + d\Gamma(\lambda_1;S_\gamma=-1)} \quad (20)$$

Using relation 19:

$$P_\gamma(S_\gamma) = \lambda_1 \cdot \frac{(1-x)[-2x+(1+x\vartheta^2 L)]}{(1+x^2)L} \quad (21)$$

Fig-7 draws the order of circular polarization of γ-quanta for the $H \Rightarrow \tau^- + \tau^+ + \gamma$ at $\lambda_1 = -1$ for τ-lepton pair over the invariant mass x. As it is seen the order of circular polarization for γ-quanta is negative and its magnitude decrease as the x-invariant mass increase.

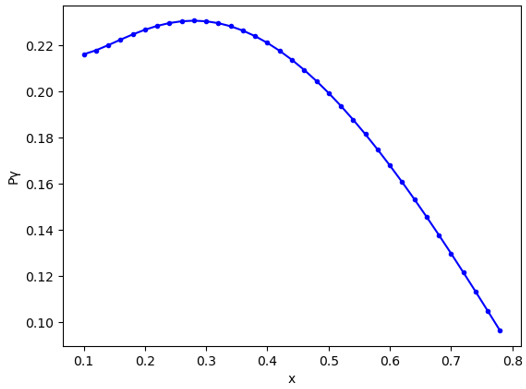

Fig. 7. The Circular Polarization for $H \Rightarrow \tau^- + \tau^+ + \gamma$ of the γ-quanta.

RESULT

We have analyzed the Higgs boson decaying by the γ-radiation from fermion-antifermion pair. Considering the helicity of fermion-antifermion pair and linear(circular) polarization, the cross section for $H \Rightarrow f + \bar{f} + \gamma$ in the framework of standard model has been calculated. The order of linear and circular polarization is being calculated and its dependency on the invariant mass od fermion-antifermion x and the angle of output θ is being carried out. The value of order of linear and circular polarization for γ-quanta in $H \Rightarrow \tau^- + \tau^+ + \gamma$ is being shown.

I would like to express my gratitude and appreciation to prof.S.Q.Abdullayev for his valuable advice on the main problem and discussion and evaluation of the final results.

[1] *S.Q. Abdullayev.* Fundamental qarşılıqlı təsirlərin ümumi xassələri. Bakı, "Zəka print", 2018, 332s.
[2] *A. Djonadi.* The anatom of ElectroWeak Symmetry Breaking. Tome I. The Higgs Boson in the Standard Model. arXiv: hep-ph/05037v2, 2005.
[3] ATLAS Collaboration. Observation of a new particle in the search for the Standart Model Higgs

boson at the ATLAS detector at the LHC. II Phys. Lett., 2012, V. B716, p. 1-29.

[4] CMS Collaboration. Observation of a new boson at mass of 125 GeV with the CMS experiment at the LHC. II Phys. Lett., 2012, V. B716, p. 30-61.

[5] *V.A. Rubakov*. On Large Hadron Collider's discovery of a new particle with Higgs boson properties. II UFN, 2012, V. 182, N.10, p. 1017-1025 (in Russian).

[6] *A.V. Lanyov*. CMS Collaboration results: Higgs boson and search for new physics II. UFN. 2014, V. 184, N. 9, p. 996-1004 (in Russian).

[7] *D.I. Kazakov*. The Higss boson is found: what is next? II UFN, 2014, V. 184, N. 9, p. 1004-1016 (in Russian).

[8] *S.K. Abdullayev, M.Sh. Gojayev, F.A. Sadding*. Decay channels of Standard Higgs boson II Moscow University Physics Bulletin, 2017, V. 72, N.4, p. 329-339

[9] *S.K. Abdullayev, M.Sh. Gojayev, F.A.Sadding*. Higgs boson decay channels: $H \Rightarrow \gamma\gamma$, $H \Rightarrow \gamma Z$, $H \Rightarrow gg$. AJP: Fizika, 2015, V. XX1, N.2, p. 17

[10] *S.Q. Abdullayev, F.A. Saddigh.* Higgs bosonun çevrilmə kanalları. II Bakı Universitetinin xəbərləri, Fizika-Riyaziyyat elmləri seriyası, 2014, N.1, 9.142-151.

[11] *A. Abbasabadi, D. Browser-Chao, D.A. Dicus, W.W. Repko*. Radiative Higgs boson decays $H \Rightarrow f\bar{f}\gamma$, II Phys. Rev., 1997, V. D55, p.5647

[12] *Y. Sun, Chang H.-R., Gao D.-N*. Higgs Decays to $\gamma l^+ l^-$ in the standard model. arXiv: 1303. 2230 v2 $[hep-ph]$, 2013.

[13] *R. Akbar, I. Ahmed, M.J.Aslam.* Lepton polarization asymmetries of $H \Rightarrow \gamma\tau^+\tau^-$ decay in the Standard Model. II Prog. Theor. Exp. Phys., 2014, 093BO3

[14] *A. Abbasabadi, W.W. Repko*. Higgs boson decay to $\mu\bar{\mu}\gamma$ II Phys. Rev., 2000, V. D62, 054025

[15] *A.Yu. Korchin, V.A. Kovalchuk.* Polarization effects in the Higgs boson decay to γZ and test of CP and CPT symmetries. arXiv: 1303. 0365V9 $[hep-ph]$, 2013.

Received: 23.10.2020

THE SCATTERING OF CURRENT CARRIERS ON LONG-WAVE ACOUSTIC PHONONS IN $In_{1-x}Ga_xSb$ (x=0.3÷0.7) AT LOW TEMPERATURES

S.Z. DAMIROVA

Institute of Physics ANAS, AZ-1143, H.Javid ave., 131, Baku, Azerbaijan

The investigations of thermopower(α) and total thermal conduction(χ_{tot}) in solid solutions $In_{1-x}Ga_xSb$(x=0.30÷0.70) in temperature interval5÷300 K, are carried out. K $\alpha(T)$ and $\chi_{t_ot}(T)$ pass through maximum in interval~20÷25 and ~30÷40 K. $\chi_{tot}(T)$ maximum is explained by Callaway theory and α(T) maxima are connected with hole scattering on long-wave acoustic phonons. It is established that the shift of maxima $\alpha(T)$ and $\chi_{tot}(T)$ and also the dependence of phonon thermopower α_{ph} on T in $\alpha_{ph}\sim T^{-3.4}$ form are in accordance with Herring theory.

Keywords: thermopower, thermal conduction, scattering, effective mass, relaxation time.
PACS: 64.75.Nx;72.20.Pa

INTRODUCTION

Last time the investigations of semiconductor physical properties having the small width of forbidden band, small effective mass and big carrier mobility are intensively carried out. The one of such semiconductors is $A^{III}B^{V}$ – $A^{III}B^{V}$ solid solution. One can form high-sensitive thermogenerators on their base. The investigation of kinetic properties of $A^{III}B^{V}$–$A^{III}B^{V}$ solid solutions is of the big interest. $A^{III}B^{V}$–$A^{III}B^{V}$ solid solutions are obtained on the base of binary compounds $A^{III}B^{V}$и $A^{III}B^{V}$. The additional thermopower which appears because of charge carriers on long-wave acoustic phonons (phonon drag) is often observed at investigation of thermopower in $A^{III}B^{V}$and $A^{III}B^{V}$ compounds. The realization of new effect takes place at approximation of electron wave numbers to phonons that is satisfied as $\kappa \approx q$ (κ and q are wave numbers of electrons and phonons correspondingly) or electron wave length are equal to phono wavelength which are observed at low temperatures. $A^{III}B^{V}$ and $A^{III}B^{V}$ samples have *p*-type conduction. That's why solid solutions also have p-type conduction. For analysis of obtained results it is necessary to emphasize the hole (χ_h) and phonon (χ_{ph}) thermal conduction components such as $\chi_{ph} = \chi_{tot} L\sigma T$ where L is Lorentz number (L=2.44 ·10^{-8} Vt·Om/K) and σ is electric conduction. At low temperatures χ_{ph} is small enough, i.e. in this region T thermal conduction is totally supplied by phonons, then $\chi_{ph} \approx \chi_{tot}$. In samples with temperature decrease both the thermal conduction χ_{ph} and phonon thermopower α_{ph} increasing take place. Such observation takes place when the increasing limit χ_{ph} forms the sample boundary limiting the free phonon length l_{ph}.

The phonon drag is observed at low temperatures in $A^{III}B^{V}$ and $A^{III}B^{V}$ compounds [1]. One can expect that given effect also takes place in these solid solutions. The coefficients of thermopower and thermal conduction in $In_{1-x}Ga_xSb$ (x=0.30÷0.70) in temperature interval 5÷300K (fig. 1 and 2) are investigated for this purpose. As it is seen from fig.1 and 2, $\alpha(T)$ in~20÷25K interval and $\chi_{t_ot}(T)$ in ~30÷40K interval pass maximum. Such observation takes place when the increase limit χ_{ph} forms the sample boundary limiting the free phonon length l_{ph}. As it is known, in crystal thermal conduction takes place whole phonon spectrum for which the effective mean free path $\bar{l}_{ph}$ is less than phonons have taking part in drag process as $\bar{l}_{ph} \ll l_{ph}$ then $\alpha_{ph}(T)$ maximum in comparison with $\chi_{ph}(T)$ maximum should be shifted to the side of low temperatures. As the maximum position depends directly on investigated sample size, for experimental question solution it is necessary to carry out χ_{ph} and α_{ph} measurements on the one and the same sample. The given question is discussed for different materials in several works [1-5]. In these woks it is revealed that $\chi_{ph}(T)$ and α_{ph}(T) maxima coincide at low temperature shift. As phonon thermopower is observed in *p*-InSb and *p*-GaSb [4] samples then it is expected that this effect can be also observed in $In_{1-x}Ga_xSb$ solid solutions which are obtained on their base. Here one moment presents interest by the fact that hole concentration and hole effective mass strongly differ from crystal *p*-InSb *and* *p*-GaSb. These distinctions should lead to the maximum shift in $\alpha(T)$ and $\chi_{ph}(T)$ in $In_{1-x}Ga_xSb$ in comparison with *p*-InSb and *p*-GaSb. From this point of view it is necessary to investigate $\alpha(T)$ and $\chi_{ph}(T)$ temperature dependences on composition dependence in $In_{1-x}Ga_xSb$ at low temperatures.

From above mentioned it is followed that the given work is dedicated to investigation of $\chi_{ph}(T)$ and $\alpha(T)$ in $In_{1-x}Ga_xSb$ (x=0.3÷0.70) at low temperatures.

EXPERIMENT TECHNIQUE

The measurement of coefficients of thermopower and thermal conduction are carried out in the crystal taken for measurement of kinetic coefficients in region 5÷300 K [6]. The temperature measurements in interval 5÷40 K are carried out by resistance carbon thermometer. The solid solution InSb-GaSb is obtained by the method zone leveling at different velocities [7]. The temperature dependences α and χ_{ph} for four samples of $In_{1-x}Ga_xSb$ are shown in Fig.1,2.

131, H.Javid ave, AZ-1143, Baku
ANAS, Institute of Physics
E-mail: jophphysics@gmail.com

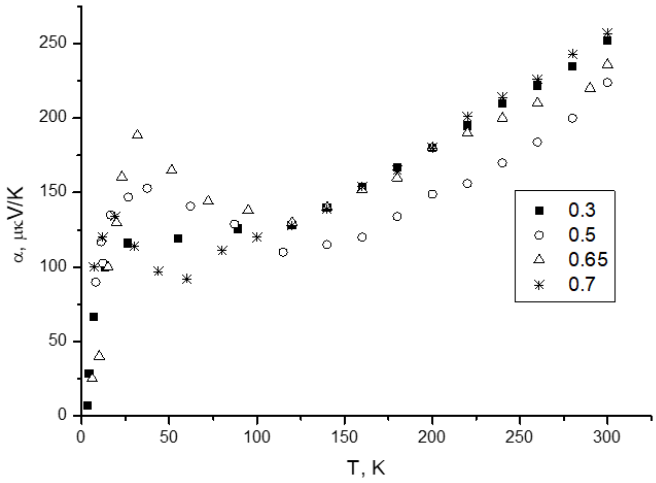

Fig.1. Temperature dependence of thermopower in $In_{1-x}Ga_xSb$ (x=0,3÷07) , where:
■- x=0.3; 0-(x=0.5); Δ- (x=0.65); ∗ – (x=0.7)

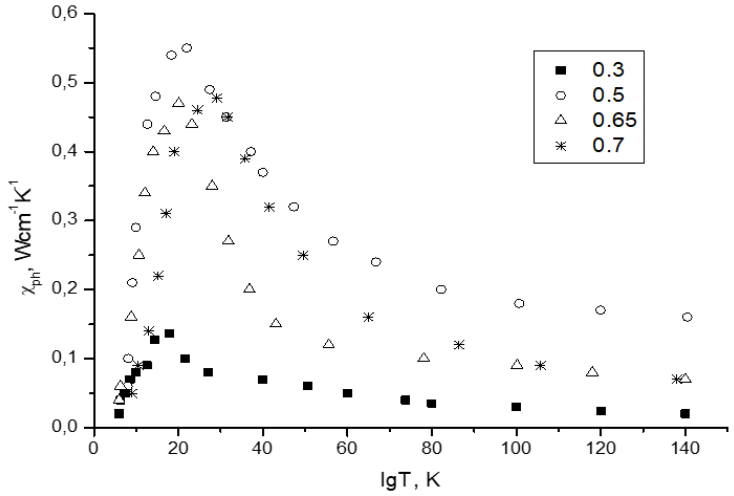

Fig.2. Temperature dependence of thermal conduction in $In_{1-x}Ga_xSb$ (x=0.3÷0.7)
■- x=0.3; 0-(x=0.5) ; Δ- (x=0.65); ∗ – (x=0.7)

As it is seen, in $In_{1-x}Ga_xSb$ thermopower increases going through maximum at T~20÷25 K beginning from 100K with temperature decrease. The thermal conductivity coefficient values χ_{ph} is significantly lower than in $A^{III}B^{V}$ crystals, the temperature motion χ_{ph} in region 90-300K isn't strong, maximum is situated in temperature interval T~30÷40K .

RESULT'S ANALYSIS

From fig.1 it is seen that $\alpha(T)$ goes through maximum in $In_{1-x}Ga_xSb$ solid solutions at temperature T~20÷25 K. $\alpha(T)$ increase at T<100 K can be accepted as phonon drag effect $\alpha_{ph}(T)$. α_{ph} exceeds diffusion component α_d beginning from T≈100 K. The hole part of thermal conductivity in $In_{1-x}Ga_xSb$ is small one, then curve $\chi_{tot}(T)$ also can be accepted as phonon part $\chi_{ph}(T)$ at T <100K because of electric conduction σ(Fig.3).

This shows that in $In_{1-x}Ga_xSb$ α_{ph} maxima to the side of low T than χ_{ph}(~45K) maxima, i.e. the theory prediction realizes. The analysis in limits of Kalavey theory [8] which allows all possible scattering mechanisms takes place by $\chi_{ph}(T)$ data. One can suppose that maximum $\chi_{ph}(T)$ at T~40-50K is caused by scattering of phonons on boundaries, point defects and phonons (umklapp and normal processes). The qualitative correlation allows us to conclude that in $In_{1-x}Ga_xSb$ there are enough quantity of eigen defects leading to intensive phonon scattering. χ_{ph} decrease in T~100-300 K interval takes place because of the influence of normal processes on χ_{ph} value. From $\chi_{ph}(T)$ curves, it is seen that increases on $\chi_{ph} \infty T^{2.2}$ law up to $\chi_{ph}(T)$ maximum. From general theory of thermal conduction, it follows that $\chi_{ph} \infty T^3$ condition satisfies. Besides, such distinction is connected with the fact that at low temperatures the phonons scatter on big effective mass of charge carrier especially on samples with p-type conduction. This type of scattering is especially intensive at low temperatures - 9-11].

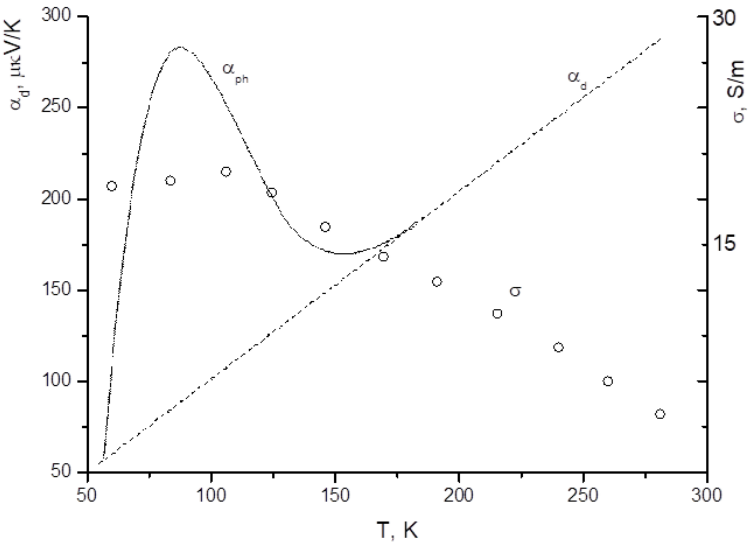

Fig.3. Calculation values $\alpha_{ph}(T)$, $\alpha_d(T)$ and experimental value σ(T) in $In_{1-x}Ga_xSb$

For theoretical analysis of $\alpha_{ph}(T)$ one should use Herring theory according to which α_{ph} value is defined by formula [12]:

$$\alpha_{ph} = \frac{k_0}{e}\frac{m^* V_0^2 <\tau_{ph}>}{3k_0 T \tau_e} - \qquad (1)$$

where κ_0 is Boltzmann constant, m^* is effective mass of charge carrier, V_0 is group velocity of long-wave phonons interacting with charge carriers (velocity of sound), τ_e is relaxation time of charge carrier is caused only by this process of interaction, $<\tau_{ph}>$ is averaged relaxation time of long-wave phonons defined by their interaction with whole crystal phonon spectrum, with defects of charge carriers and crystal boundaries. From formula [1] it is seen that of $<\tau_{ph}>$ big value, i.e. high thermal conductivity is formed for drag effect appearance at not small effective mass of charge carriers. In this case α_{ph} temperature motion is defined by τ_{ph}/т temperature motion. $<\tau_{ph}(\text{т})>$ dependence by Herring is caused by crystal symmetry [12].

For $\alpha_{ph}(T)$ calculation in approximation of relaxation time in the dependence on scattering on long-wave acoustic phonons is defined by following way. The averaged relaxation time of long-wave phonons is expressed by formula [13,14].

$$<\tau_{ph}(\text{т})> = \frac{1}{4\text{к}^4}\int_0^{2\text{к}} \tau_{ph} q^3 dq \quad , \qquad (2)$$

where

$$\tau_{ph}^{-1} = \frac{\hbar q}{\rho_0}\left(\frac{k_0 T}{\hbar V_0}\right)^4 V_0 \quad , \qquad (3)$$

here ρ_0 is crystal density. Substituting the (3) expression in formula (2) for the definition of averaged relaxation time of long-wave phonon we obtain:

$$<\tau_{ph}> = \frac{2\rho_0}{3\sqrt{2m^* k_0 T}}\left(\frac{\hbar V_0}{k_0 T}\right)^4, \qquad (4)$$

Taking under consideration formula (4) for averaged absorption mean free path of long-wave phonons we obtain the following expression

$$l = \frac{2\rho_0}{3\sqrt{2m^* k_0 T}}\left(\frac{\hbar V_0}{k_0 T}\right)^4 V_0 \quad , \qquad (5)$$

For τ_e definition including in formula (4) and for charge scattering the carriers on acoustic phonons at standard band has the form [15]:

$$\tau_{ac}(T) = \frac{9\pi}{2}\frac{\rho V_0^2 \hbar^4}{C^2 (2m^* k_0 T)^{3/2}} \qquad (6)$$

C is constant where it connects with deformation of E_d lattice deformation potential by following way $E_d = \frac{2}{3}C$ [15]. Substituting ρ, V_0, C, m^* values in formula (5), we define $\tau_e(T)$. Taking under consideration $<\tau_{ph}>$ and τ_e in formula (1) we define $\alpha_{ph}(T)$. The general thermopower is equal to sum of partial phonon and diffusion thermopower (α_d) as

$$\alpha = \alpha_{ph} + \alpha_d$$

where $\alpha_d = -\frac{\kappa_0}{e}\left[r + 2 + \ln\frac{2(3\pi m^* k_0 T)^{3/2}}{\hbar^3 n}\right]$. Here r is scattering mechanism parameter, n is charge carrier concentration.

The calculative data of $\alpha_{ph}(T)$ and $\alpha_d(T)$ for sample $In_{0.5}Ga_{0.5}Sb$ (where V_0= $5.2\cdot10^5$ cm/c, ρ_0=5.66 gr/cm^3, m^*=0.340m$_0$, E_d=45 eV) are presented in Fig.3.

As it is seen from fig.3 the theoretical calculation of maximum value $\alpha_{ph}(T)$ in comparison with experimental one is in two times bigger.

This can be connected with two reasons:

1) the shifted scattering (acoustic ions) takes place in this temperature region,
2) the hole gas is strongly degenerated. For confirmation of second preposition the chemical

potentials at $T \leq 20$ K are defined by formula [15]:

$$\alpha = -\frac{k_0}{e}\left[\frac{F_{r+2}}{F_{r+1}} - \mu^*\right] \quad , \qquad (6)$$

μ^* is given chemical potential, $F(\mu^*)$ is one-parameter Fermi integral. The obtained data are given in the table.

Table

The band parameters in $In_{1-x}Ga_xSb$

x	P, cm^{-3} 10^{16}	$\eta^*(T=15\ K)$	m^*	E_g, eV (T=0 K)	μ, $cm^2/V{\cdot}s$ T=15 K	E_d, eV
0.20	4,5	14	0.363 [13]	0.285[13]	2800	42
0.50	5.0	16	0.340 [16]	0.370[16]	2764	45
0.65	6.30	19	0.376[13]	0.368 [13]	2500	47
0.7	6.80	21	0.389[13]	0.775[13]	1782	50

P is hole concentration, m^* is effective mass of holes, E_g is forbidden band width, μ is hole mobility, E_d is deformation potential.

The comparison of experimental and calculative data of $\alpha_{ph}(T)$ and table data show that this effect is strongly emphasized at removal of hole gas degeneration, i.e. the hole drag on long-wave acoustic phonons more intensively changes in the dependence on crystal symmetry [12]. For general dependence α_{ph} (T) hasn't universal form in the region of its increase up to maximum.

The theoretical calculation shows that we should take charge carrier scattering on lattice acoustic oscillations for $\alpha_{ph}(T)$ definition.

From theory, it is followed that significantly bigger effective mass of charge carriers, absence of electron gas degeneration and big value of $<\tau_{ph}>$ long-wave phonons in $In_{1-x}Ga_xSb$ cause the strong effect of hole increasing by phonons. The rest values of formula (1) weakly depends on temperature.

The analysis of other crystals shows that the given drag effect shows that α_{ph} should depend on T as $\alpha_{ph} \infty T^{-3,5}$ for cubic crystals and depend on as $\alpha_{ph} \infty T^{-3}$. Inn temperature interval the charge carries scatter on ions, drag effects weakens and it influences on $\alpha_{ph}(T)$ dependence. If the phonon free path length achieves the sample minimum sizes ($\tau_{ph} = const$), temperature motion of $\alpha_{ph}(T)$ is defined by $1/T\ \tau_e$ value change on temperature at $\tau_e \infty T^{-3/2}$, $\alpha_{ph} \infty T^{-0.5}$.

$In_{1-x}Ga_xSb$ solid solutions are related to the number of diamond-like structure [17]. According to this the calculation shows that α_{ph} dependence on T has the form $\alpha_{ph} \sim T^{-3.4}$. In experiment this fact is designated as $\alpha_{ph} \sim T^{-3}$. Probably these distinctions in this temperature region are connected with the fact that there is additional scattering mechanism.

Thus, the going through $\alpha_{ph}(T)$ maximum at $\alpha_{ph}(T)$ temperature interval in $In_{1-x}Ga_xSb$ solid solutions totally agrees by Herring theory as charge carrier drag by phonons caused by unique scattering mechanism of long-wave phonons.

[1] *I.I. Timchenko,S.S.Shalit.* PhSS, 1962, 4.

[2] *S.A. Aliyev , A.I. Nashelski, S.S. Shalit.* 1965, 7(5), 1590.

[3] *S.A.Aliyev*. PhTS 7(1) , 168, 1973.

[4] *S.A. Aliyev.* Some questions of experimental and theoretical physics, Baku, Elm, 1977.

[5] *S.A. Aliyev, F.F. Aliyev, Z.S. Gasanov, S.M.Abdullayev, R.I. Selim-zade*. PhTS, 44 (6), 764(240).

[6] *S.A. Aliyev, V.G. Arasli, Z.F. Agayev, Z.I. Zulfugarov, Sh.S. Ismayilov.* News of AzSSR Academy of Sciences, series of phys-tech. and math. Sciences, 6.67, 1982.

[7] *V.I. Ivanov-Omski, B.T. Kolomnez.* PhTS, 1.6,913, 1959, (T.1, B.6, C913).

[8] *Y. Gallaway*. Phys.Rev. 1959, 113 (4), 1046.

[9] *I.A. Smirnov, V.I. Tamarchenko.* Electron conduction in metals and semiconductors, "Science", L, 1977, p.151.

[10] *S.A. Aliyev, F.F. Aliyev, S.G. Abdinova, Z.S. Gasanov, D.M. Ragimova.* Izv.Vuz, Physics, № 6, 41, 1990.

[11] *L.S. Parfenyeva, I.A. Smirnov, A.V. Fokin, H.* Misporek, Y. Mukha, A. Yejovski, 2003, PhST, 45, 2, 359.

[12] *C. Herring.* Phys. Rev. 1954, 95, 954.

[13] *A.I. Anselm*. Introduction into semiconductor theory, M. Science, 1978.

[14] *B.A.Askerov.* Transition electron phenomena in semiconductors, M. Science, 1985.

[15] *B.A.Askerov,* Kinetic effects in semiconductors L., Science, 1970.

[16] *F.F. Aliev, S.Z. Damirova, S.A. Zeynalova, M.M. Zarbaliyev.* The actual problems of Solid State Physics, Theses of VIII International Conference (Minsk, September, 24-28, 2018), vol.2, pp. 41-42.

Received: 14.10.2020

PERFORMANCE OF NEW MAPD PHOTODIODES

N.V. SADIGOVA[1], F.I. AHMADOV[1,2], A.Z. SADIGOV[1,2], A.H. MAMMADLI[1], A.H. GERAYEVA[1], N.N. HEYDAROV[1]

[1]Institute of Radiation Problems of ANAS, Baku, Azerbaijan

[2]National Nuclear Research Center, Baku, Azerbaijan

e-mail: saazik@yandex.ru

The article presents the results of the study of optical characteristics and the calculation of the internal gain of a new micropixel avalanche photodiode (MAPD). The calculation procedure is described, the experimental setup of the performed studies, and the results of the study of parameters at low light fluxes, up to single photons, are also presented. It was revealed that avalanche photodiodes with a micropixel structure can be silicon analogs of widely used vacuum photomultiplier tubes.

Keywords: Photodiode; MAPD; APD; photodetector.
PACS: 85.30.−z; 85.60.Dw

INTRODUCTION

Modern photomultiplier tubes (PMTs) have a high gain (10^6-10^7). This allows them to be used without an additional signal amplifier. Also, the photomultiplier tube can be used as a low intensity light detector. The advent of avalanche photodiodes with negative bias voltage, which quenches the avalanche process, made it possible to create an avalanche photodiode (APDg) operating in the "Geiger" mode. This APDg has a high gain (10^5-10). However, in this case, the dead time of the device becomes large (on the order of microseconds).

In order to solve the problem of recording the intensity light flux in recent years, a new type of photodetector has been developed - a silicon micropixel avalanche photodiode (MAPD), which is a photodetector based on an ordered set (matrix) of pixels (approximately 10^3 mm^{-2}) made on a common substrate. Each pixel is an APD photodiode operating in the Geiger mode with a multiplication factor of about 10^6, but the entire MAPD is an analog detector, since the MAPD output signal is the sum of signals from all pixels triggered when they absorb the photons [1].

Note that when the intensity of the incident light flux is high, i.e., the probability of the production of several photoelectrons in one pixel is significant, or all cells are triggered, the output signal from the MAPD becomes saturated. Thus, there is an upper limit on spectrometric recording of light intensity.

EXPERIMENTAL SAMPLE

MAPD is a device of a new type for detecting light flashes of low intensity (at the level of single photons) and duration of the order of units - hundreds of nanoseconds [1, 2]. Similar to vacuum PMTs, MAPD can become a device of wide application due to the following qualities:

• High internal gain of about 10^6, which significantly reduces the requirements for electronics;

• Small spread in the gain (about 10%) and, as a result, low noise factor;

• The efficiency of registration of visible light at the level of vacuum photomultipliers;

• The ability to register nanosecond light flashes without distorting the shape of the detected signal;

• The ability to work both in the pulse counting mode and in the spectrometric mode;

• Good temporal resolution (tens of picoseconds);

• Low supply voltage (50-90 V, depend on design);

• Insensitivity to the magnetic field; compactness (crystal dimensions of the order of ~3 x 3 x 0.3 mm^3).

In fig. 1 schematically shows the principle of a MAPD device, which consists of independent pixels with dimensions of the order of 30x30 μm. By means of aluminum buses, all pixels are combined, and the same bias voltage (U_{bias}) is applied to them, exceeding the breakdown voltage ($U_{breakdown}$) by 10-15% [3], which ensures operation in "Geiger" mode. When a quantum of light enters the active region of the pixel, a self-extinguishing "Geiger" discharge develops in it. Quenching, i.e. termination of the discharge, occurs due to a voltage drop at the p-n-junction below the breakdown due to the presence of a current-limiting resistor in each pixel (R_{lim} = 400 kΩ). The current signals from the triggered pixels are added to the total load. The amplification of each pixel is about 10^6, so the detector can be operated on a cable without pre-amplification.

Since all MAPD pixels are independent microcounters, and the signal from each pixel is determined by the charge accumulated at each pixel, the MAPD gain (M) is determined only by the charge (Q_{pixel}) of the pixel capacitance C_{pixel} [3]:

$$M = Q_{pixel}/e \qquad (1)$$

where, $Q_{pixel} = C_{pixel} \cdot \Delta U = C_{pixel} \cdot (U_{bias} - U_{breakdown})$, and e=1.6*10^{-19} C – electron charge.

131, H.Javid ave, AZ-1143, Baku
ANAS, Institute of Physics
E-mail: jophphysics@gmail.com

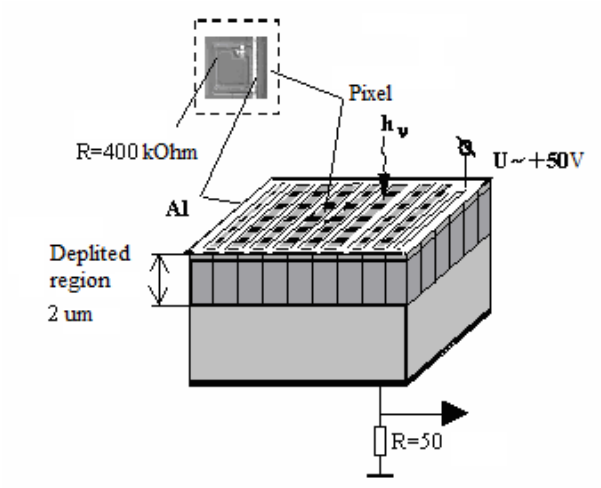

Fig. 1. Schematic view of MAPD photodiode.

The spread in the gain is determined by the technological spread in the elementary capacitance and the pixel breakdown voltage and is less than 10%. Since all pixels are the same, the detector's response to weak light flashes is proportional to their intensity [4].

EXPERIMENTAL SETUP

Figure 2 shows a diagram of the elements and blocks that make up the experimental setup, with which measurements were made.

A blue LED NSPB310A was used as a light source. The LED is powered from a waiting pulse generator (Led supply) with a frequency of 1000 Hz and duration of 15 ns. The amplitude of the pulses is adjustable in the range of 0-7 V, which allows changing the intensity of the light emitted by the LED. The waiting pulse generator is started by the trigger pulse generator (Tektronix AFG3100).

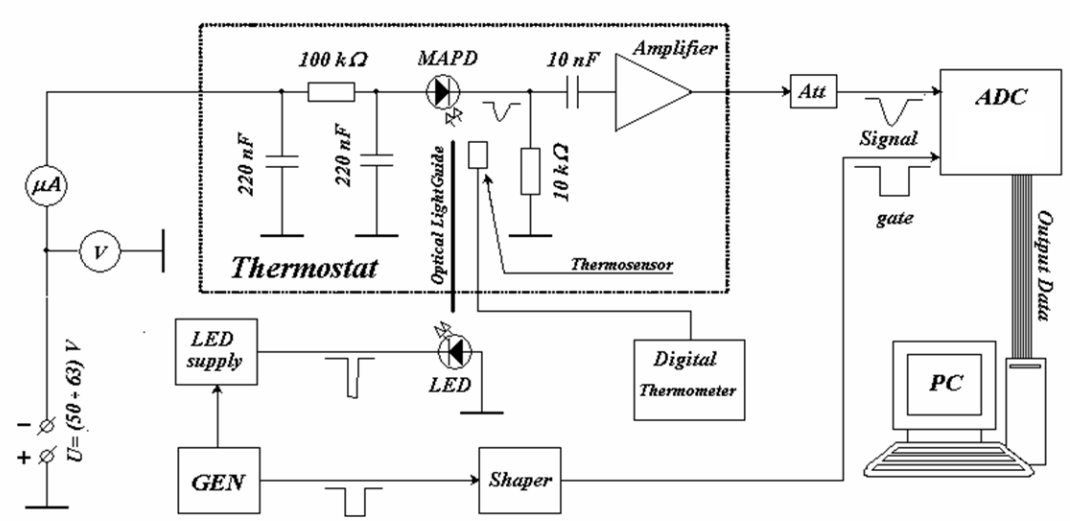

Fig. 2. Experimental setup.

The LED is located outside the Thermostat. This is necessary in order to exclude possible fluctuations of its characteristics from temperature. The light emitted from the LED is transported to the thermostat by an optical light guide to the photodiode (MAPD). The photodiode is powered by an external regulated voltage source (U = 50-63 V). To suppress ripple from the power source, as well as external high-frequency interference (which can occur in the electrical circuit through external electromagnetic radiation), C-R-C is included in the power supply circuit of the photodiode. (U-shaped) filter (here capacitance C=220nF, resistance R=100kΩ). A voltmeter measures the voltage applied to the MAPD, which is calculated:

$$U_{bias} = U - I * R, \quad (2)$$

where I is avalanche current, R is quenching resistor. As a result of the light pulse hitting the surface of the photodiode, a current pulse arises, which is amplified by a low-noise hybrid high-speed linear amplifier. The capacitance (10 nF), included at the amplifier input, to break the galvanic connection between the MAPD

load (R = 10 kΩ) and the amplifier input is designed to prevent disruption of the DC input stage of the amplifier.

The installation uses a high-speed analog-to-digital converter (ADC) CAEN. The output signal from the amplifier is fed to the ADC, which digitizes the signal area (charge) in the presence of a gate pulse. The attenuator (Att) is designed to increase the dynamic range of the measured signals with MAPD. The strobe pulse is created by the trigger generator and has a duration of 60 ns, which is set by the shaper. The synchronization of the strobe pulse and the signal makes it possible to register the pulse arising from the photodiode under the action of the initiating light against the background of dark (noise) pulses. However, noise signals are recorded during the duration of the strobe pulse. The number of recorded noise pulses is determined by the formula:

$$N_c = N_n \nu \tau, \quad (3)$$

where N_c is the counting rate of random coincidences, N_n is the counting rate of noise pulses, respectively, □ is the trigger pulse repetition rate, τ is the strobe pulse duration.

The data (output data) from the ADC is read by a computer (PC) by means of a controller; a computer.

METHODOLOGY

The measurement technique is based on the use of low-intensity light flashes. The incident photon flux onto the photodetector produces photoelectrons through the photoelectric effect. Under real conditions, the number of photons hitting the photodetector is not constant, but obeys the Poisson distribution. Photo conversion is a binary process. Convolution of a Poisson process with a binary process gives again the Poisson distribution. Therefore, the formation of photoelectrons also obeys the Poisson distribution:

$$P(n;\mu) = \frac{\mu^n * e^{-\mu}}{n!} \quad (4)$$

where, μ −is the average number of photoelectrons resulting from photo effect, $P(n;\mu)$ − the probability that n photoelectrons will be observed at the output of the photodetector, with their average equal to μ.

Data from ADC are analyzed by a personal computer and presented in the form of a histogram channel number (charge) - the number of events that hit the channel (Fig. 3). The ADC channel unit is 0.25 pC. In what follows, all values (if not specified) are indicated in channel units.

To determine the average number of photoelectrons, we use the fact that at small they are distributed according to the Poisson distribution. The probability that we will not register any photoelectrons is equal to:

$$P(0;\mu) = \frac{\mu^0 * e^{-\mu}}{0!} = e^{-\mu} \quad (5)$$

hence the average number of photoelectrons hitting the photo detector:

$$\mu = -lnP(0;\mu) \quad (6)$$

The signal corresponding to the fact that no photoelectron was formed on the photo detector enters the ADC pedestal (Fig. 3). Thus, the probability of the absence of a photoelectron is:

$$P(0;\mu) = N_{ped}/N \quad (7)$$

where N_{ped} is the number of events in the pedestal, N is the total number of events.

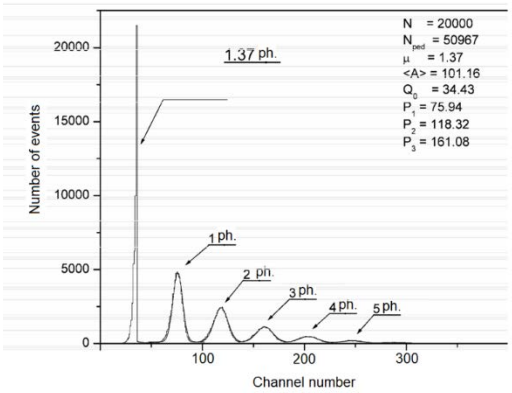

Fig. 3. MAPD spectrum (at fixed T and U_{bias}). Designations: N, N_{ped} - respectively the total number of events and the number of events in the pedestal; μ is the average number of photoelectrons; <A> - average value of the histogram; Q_0 is the position of the pedestal, P1, P2, P3 are the positions of the peaks of the 1st, 2nd and 3rd photoelectrons, respectively.

The average signal S is defined as the average of the histogram <A> minus the position of the pedestal Q_0:

$$S = < A > - Q_0 \quad (8)$$

The uncertainty that occurs when determining the signal is associated with a statistical uncertainty in determining the position of the pedestal and a statistical uncertainty in determining the average amplitude of the histogram and does not exceed 1%.

The gain fluctuates around the statistical mean and is determined by the probability distribution with the mean M [13]. The response of a photodetector (output charge) to a single photoelectron is the gain and can be described by a Gaussian distribution (similar PMT):

$$M(x) = \frac{1}{\sigma_1 \sqrt{2\pi}} \exp\left(-\frac{(x-Q_1)^2}{2\sigma_1^2}\right) \quad (9)$$

where x is a variable (charge),Q_1=M_e(e=1.6*10^{-19}C) - average charge on the output of the photodetector, when one photoelectron was generated as a result of photoconversion, σ_1 - respectively, the standard

deviation of the charge distribution [5]. Thus, the position of the peak of the Gaussian distribution (Q_1) determines the gain of the photodetector and is calculated as:

$$Q_1 = P_1 - Q_0 \quad (10)$$

from where:

$$M = \frac{Q_1}{e} \quad (11)$$

It should be noted that in our case the output signal from the photodetector passes through the amplifier-attenuator system amplifying the signal by a factor of K (in our case, K = 36) times, therefore, the gain of the photodetector is:

$$M = \frac{Q_1}{K*e} \quad (12)$$

From the data shown in Fig. 3 MAPD gain in absolute units, based on the position of the peak (P_1) of one photoelectron (channel unit $0.25*10^{-12}$C):

$$M = \frac{41.51*0.25*10^{-12}C}{36*1.602*10^{-19}\,C} = 1.80 * 10^6 \quad (13)$$

The gain can be determined using the peak position of N photoelectrons (P_N) as:

$$M = \frac{(P_N - Q_0)}{N*K*e} - \frac{Q_N}{K*e} \quad (14)$$

The dispersion of N-electron Gaussian distributions is associated with the inhomogeneity of the photosensitivity of the photodetector surface, the technological spread and fluctuations in the number of electrons in the avalanche, as well as the noise of MAPD and recording electronics.

At low light intensities (Fig. 4, a, b), when the registration inefficiency (the relative number of events in the pedestal) is large enough, which makes it possible to determine the average number of photoelectrons (relative light intensity) with good accuracy.

If the intensity of the light flash is increased (Fig. 4,c), the registration inefficiency decreases exponentially, which worsens the ability to measure μ. At high light intensities, the registration efficiency is high, which corresponds to the absence of events in the pedestal (Fig. 4, d). It can be seen from the spectrum in Fig. 11, d that the formation of single photoelectrons is strongly suppressed. For example, the probability of the formation of first photoelectron is $P(1,16.5)=1.1*10^{-6}$, and second is $P(2,16.5)=1.0*10^{-5}$.

When registering high light intensities, the average number of photoelectrons is determined as:

$$\mu = \frac{S}{M} \quad (15)$$

where S is the average signal amplitude, M is the gain of the photodetector, which can be determined at low light intensities using the above technique, as was done to determine the light intensity in the spectrum shown in Fig. 4, d.

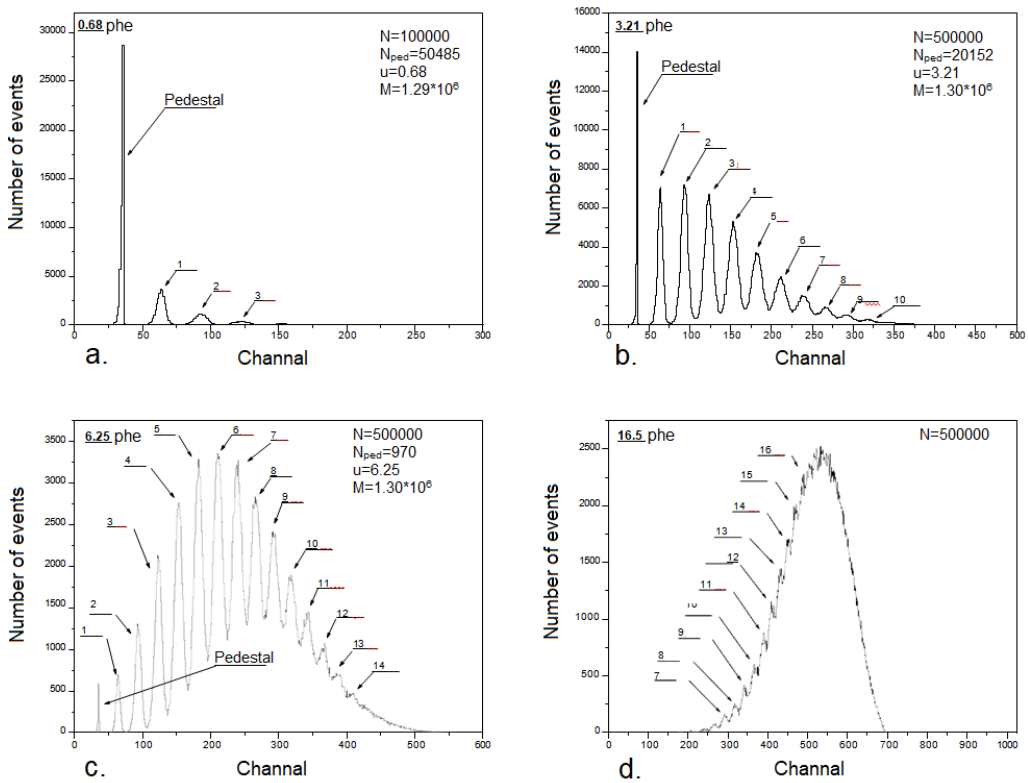

Fig. 4. Spectra obtained with MAPD (T = 220C, U_{bias} = 60V). Designations: N - total number of events, bold and underlined numbers, μ - average number of photoelectrons, M - gain determined from the peak of the first photoelectron.

RESULTS

The results of optical studies of a silicon-based micro pixel avalanche photodiode are obtained. The research method and calculations are shown, as well as the preparation of the experimental stand.

It was revealed that the photodiode of the MAPD type is a successful device for counting single photons, as well as for spectrometric measurements.

ACKNOWLEDGMENT

This work was supported by the Science Development Foundation under the President of the Republic of Azerbaijan, Grant №. EİF—BGM-5-AZTURK-1/2018-2/01/1-M-01

[1] *P. Buzhan* at al. 7th International Conference on Advanced Technology and Particle Physics. Como, Italy, 2001. The advanced study of silicon photomultiplier.

[2] *P. Buzhan* at al.: 3rd International Conference on New Developments in Photodetection. Beaune, France, 2002. Silicon Photomultiplier and its possible applications.

[3] *B. Dolgoshein.* Silicon photomultipliers in particle physics: possibilities and limitations. MIPhI, Moskow

[4] *Z. Sadygov* et al. On the prospects of using a new silicon avalanche photodetectors with local negative coupling JINR, LHEP, 2000, (Russian).

[5] *Chirikov-Zorin* et al. Absolute calibration and monitoring of a spectrometric channel using a photomultiplier. Preprint of JINR, Dubna, 1993; Nuclear Instrument & Methods A339(1994)468.

Received: 28.10.2020

ISSN 1028-8546

2020, Vol. XXVI, № 3
Section: En

CONTENTS